DECORATION OF GRAPHENE SHEETS BY METAL OXIDE PARTICLE: SYNTHESIS, CHARACTERIZATION, AND APPLICATION IN HYDROGEN STORAGE

by
ZAHRA GOHARI BAJESTANI

Submitted to the Graduate School of Engineering and Natural Sciences
in partial fulfillment of
the requirements for the degree of
Doctor of Philosophy

Sabanci University
August 2017

Decoration of graphene sheets by metal oxide particles: synthesis, characterization, and application in hydrogen storage

APPROVED BY:

Prof. Dr. Yuda Yürüm.....
(Thesis Supervisor)

Prof. Dr. Nilgun Yavuz.....

Prof. Dr. Serhat Yesilyurt.....

Assoc. Prof. Dr. Selmiye Alkan Gürsel.....

Assoc. Prof. Dr. Adem Tekin.....

DATE OF APPROVAL: 01.08.2017

ABSTRACT

DECORATION OF GRAPHENE SHEETS BY METAL OXIDE PARTICLE: SYNTHESIS, CHARACTERIZATION, AND APPLICATION IN HYDROGEN STORAGE

Zahra Gohari Bajestani

PhD Dissertation, August 2017

Supervisor: Prof. Yuda Yürüm

Keywords: Hydrogen storage, Graphene, Adsorption, Nanocomposite.

This is the thesis for a doctorate of Sabanci University and relates to the synthesis of graphene based nanocomposites as media to store hydrogen gas. The aim of this work is to develop such materials with improved hydrogen storage capacity at ambient temperature and pressures that can also provide the adaptability to onboard systems and public safety.

In the first part of this work, graphene sheets were decorated by 2.8 wt% transition metal oxide (TiO_2, NiO, Fe_3O_4, CuO) for hydrogen uptake. Among these nanocomposites, sample decorated with Fe_3O_4 showed the maximum hydrogen uptake of 0.4 wt% at room temperature while TiO_2 showed the highest improvement in the isosteric heat of adsorption (12kJ/mol at a surface coverage of 50%) when normalized by maximum uptake at 298k due to the strong interaction between hydrogen molecules and substrate. Moreover, a series of graphene-based nanocomposites with different TiO_2 contents (10, 12 and 15 wt%) have been prepared via a facile chemical method. The highest hydrogen uptake of 0.39 wt% was obtained for the sample with 12 wt% TiO_2 nanoparticle that is 125% higher than the

hydrogen adsorption of the parent graphene material. In the next part of this work, homogeneously distributed TiO_2 nanoparticles with (001) reactive facets were grown over nitrogen-doped reduced graphene oxide sheets by a solvothermal method. Hydrogen storage capacity of the system was significantly improved to 0.91 wt% that is the highest hydrogen storage ever reported for graphene-based nanocomposites at room temperature and low pressures. Importantly, this nanocomposite exhibits ~91% capacity retention through 5 cycles with more than 88% release of the stored hydrogen at ambient conditions. In the last part of the thesis, we reported the development of a heterogeneous catalyst consisting of Al_2O_3 nanoparticle and low amounts of Pd that markedly enhances the hydrogen uptake of RGO. It was shown that incorporation of 1 wt% heterogeneous catalyst (<0.3 wt% Pd) significantly increased the hydrogen storage capacity of RGO from 0.17 wt% to 0.31 wt%. This indicated a rise of hydrogen uptake by a factor of 1.8 in RGO nanocomposite.

OZET

DECORATION OF GRAPHENE SHEETS BY METAL OXIDE PARTICLE: SYNTHESIS, CHARACTERIZATION, AND APPLICATION IN HYDROGEN STORAGE

Zahra Gohari Bajestani

PhD Dissertation, August 2017

Supervisor: Prof. Yuda Yürüm

Keywords: Hidrojen depolama, Grafen, Adsorpsiyon, Nanokompozit.

Bu tez, Sabancı Üniversitesi doktora tezi olup hidrojen gazı depolaması için grafen esaslı nanokompozitlerin sentezi ile ilgilidir. Bu çalışmanın amacı, ortam sıcaklığında ve basıncında hidrojen depolama kapasitesi geliştirilmiş malzemelerin, yerleşik sistemlere ve kamu güvenliğine uyum sağlayacak şekilde geliştirilmesidir.

Bu çalışmanın ilk bölümünde grafen tabakaları, hidrojen alımı için ağırlıkça %2.8 geçiş metal oksidi (TiO_2, NiO, Fe_3O_4, CuO) ile yüklenmiştir. Bu nanokompozitlerden Fe_3O_4 ile yüklenen örnek, oda sıcaklığında %0,4 ile en yüksek hidrojen alımını gösterirken, izostrerik adsorpsiyon ısısındaki en yüksek miktardaki iyileşmeyi TiO_2 (yüzeyin %50 kaplandığı durumda 12kJ/mol) göstermiştir. Bu değerler 298K'de maksimum alım için normalleştirilmiştir. Ayrıca, farklı TiO_2 içerikli (ağırlıkça %10, 12 ve 15) grafene dayalı nanokompozitler kolay bir kimyasal yöntemle hazırlanmıştır. Bu nanokompozitlerde, en yüksek hidrojen alımı ağırlıkça %0.39 olmuş ağırlıkça %12 TiO_2 nanoparçacıkları içeren

numune ile elde edilmiştir. Ulaşılan hidrojen alımı miktarı ana grafen maddesinin hidrojen adsorpsiyon miktarından %125 oranında yüksek olmuştur.

Bu çalışmanın sonraki bölümünde, (001) reaktif fasetlere sahip homojen olarak dağıtılan TiO2 nanopartikülleri azot katkılı indirgenmiş grafen oksit tabakaları üzerinde solvotermal bir yöntemle yerleştirilmiştir. Sistemin hidrojen depolama kapasitesi, oda sıcaklığında ve düşük basınçlarda grafen bazlı nanokompozitler için şimdiye kadar rapor edilen en yüksek hidrojen depolama miktarı olan ağırlıkça % 0,91'e ulaşmıştır. Önemli biçimde, bu nanokompozit ortam koşullarında depolanan hidrojenin %88'den fazla salınması ile 5 döngü boyunca ~% 91 kapasite retansiyonu sergilemektedir.

Tezin son bölümünde, Al_2O_3 nanoparçacıkları ve az miktarda Pd içeren heterojen bir katalizörün, RGO'nun hidrojen alımını önemli ölçüde arttırdığı bidirilmiştir. Ağırlıkça %1 oranında heterojen katalizör (ağırlıkça <%0.3 Pd) eklenmesinin, RGO'nun hidrojen depolama kapasitesini ağırlıkça %0,17'den %0,31'e arttırdığı gösterilmiştir. Gözlemlenen bu artışın, RGO nanokompozitinde hidrojen alımını 1,8 faktörü ile arttırdığı gösterilmiştir.

ACKNOWLEDGEMENTS

I would love to express my deepest gratitude to my advisor Professor Dr. Yuda Yürüm for his unwavering support, collegiality, and mentorship throughout my PhD. He has always supported me and has given me enthusiasm for science. I am really grateful to his supervision and owe him a greatest degree of appreciation. It was a great honor to finish this thesis under his supervision.

I am genuinely appreciative of Professor Alp Yürüm for his valuable scientific guidance and support.

Particular thanks must also be recorded to Professor Yürüm's group member, Ezgi, Mustafa, Aysu and Sahand for their academic support and friendship.

My thankfulness is also to the staff of faculty of engineering and natural sciences, FENS, for their support and kind care.

A special gratitude goes to my beloved family for their encouragement and whole hearted love.

And finally I would love to acknowledge my husband, Omid, who blessed me with a life of joy and also I wish to thank him for his love and help during my studies at Sabanci University.

TABLE OF CONTENT

List of Figures

Chapter 1 : General Introduction

1.1 Introduction

Fossil fuels are non-renewable and finite resources of energy that became too expensive and environmentally damaging. In contrast, many types of renewable energy resources-such as wind and solar energy-are constantly replenished and will never run out. Renewable energies are important because they are clean sources of energy and they have a much lower environmental impact compare to conventional energies. Recently, climate changes arising from global warming has actuated scientists in search of environmentally friendly renewable energy resource [1-3].

Hydrogen attracts a considerable attention in energy area since it holds the promise as a clean energy resource for the next-generation energy carriers in mobile and stationary power systems. In recent years, production, storage, and consumption of energy have become a serious problem that our world currently faces [4]. Although several systems have developed for hydrogen production and combustion, most of storage systems have encountered challenges. The biggest Issues related to the success of H_2-based technologies for on-board technologies rely on the safe and efficient storage of hydrogen. Recently, several methods such as high-pressure tanks, liquefied H_2 tanks, and storage in solid materials are examined to store hydrogen [5].

- **Compressed hydrogen storage technologies:** Hydrogen can be stored in different types of pressure vessels including cylinders and polymorph. Normally the pressure of hydrogen gas changes between 25 MPa (compressed natural gas) and 30 MPa (oxygen and air for breathing apparatus) but recently 35-70 MPa vessels are developed and used to store hydrogen. The most important issues that should be considered during using hydrogen gas to prevent the risk of failure by leakage in service and guaranty the performance are storage, transportation, use (emptying, handling, etc), filling steps, periodic inspection, and maintenance [5].
- **Cryogenic storage:** Liquefying hydrogen is both time consuming and energetic process since it needs to be done at a low temperature such as -235 °C. In addition, it is difficult to store liquid hydrogen over a long period because evaporation from the system is

unavoidable and more than 40% of the energy content can be lost. Hence, it is not a preferred method to store hydrogen especially for on board applications.

- **Solid state storage:** Hydrogen storage by solid compounds holds apparent advantageous compared to high-pressure tanks or liquefied hydrogen due to its safe and efficient utilization and also a gas can be stored reversibly in solid materials under pressure and temperature conditions [2]. The thermodynamic and kinetics of adsorption play an important role to determine a good storage media. The thermodynamic is defined by measuring the hydrogen pressure-composition characteristics under equilibrium conditions at a given temperature. In the case of kinetics, since adsorption of hydrogen is exothermic process therefore good management of heat transfer with the exterior is required to avoid penalizing the kinetics [5]. Finding materials for efficient hydrogen storage is one the most important components for the adoption of hydrogen in future of renewable energies [6, 7]. Several candidates such as metal–organic frameworks (MOFs), porous organic frameworks (POFs), porous carbon based materials, etc were studied during the last decades to provide safe and effective hydrogen adsorbents but none of them meets the storage targets set by the U.S. Department of Energy (DOE)(a gravimetric goal of 5.5 wt.% hydrogen storage for an on board system by 2020 and an ultimate target of 7.5 wt.%) [8-11].

Among these options proposed as hydrogen storage media, carbon nanostructures, such as fullerenes, carbon nanotubes, and graphene have attracted wide attention due to large surface area, low density, inexpensiveness, high thermal stability and exceptional mechanical properties [12]. Graphene has been cited as a promising candidate for energy conversion and storage applications because it has high theoretically surface area, large microporosity, and good chemical stability [13-16].

Recently, much work has been focused on the synthesis of single layer and few layer graphene because the availability of graphene is a key factor for its use in research and development into possible applications. There are different methods to prepare graphene that can be grouped as follow:

- Micromechanical cleavage of highly oriented pyrolytic graphite or natural graphite
- Epitaxial growth of graphene on SiC and metal (Ru, Pt)

- Thermal- or plasma-enhanced chemical vapor deposition (CVD) of graphene from the decomposition of hydrocarbons at high temperatures on metal substrates (such as Ni, Cu, Pt) or metal oxide (Al_2O_3, MgO) particles
- Chemical exfoliation of graphitic materials
- A bottom-up synthesis strategy from organic compounds
- Other methods such as electrochemical exfoliation of graphite, graphene growth from solid state carbon, direct arc discharge of graphite, reduction of ethanol by sodium metal, and the thermal splitting of SiC granules

It is worth mentioning that among mentioned methods; currently, the chemical exfoliation method is the most common route to prepare the graphene at low cost and high quality. This procedure starts with oxidation of graphite to increase the d-spacing and intercalation between graphite layers as a result of the weak interaction between the sheets. After that, it continues for reduction of graphite oxide (GO) by chemical or thermal treatment to obtain reduced graphene oxide (rGO) [17].

With reference to hydrogen adsorption of pure graphene, the range of reported hydrogen uptakes of graphene at ambient conditions is low[18]. For example, Srinivas et al.[19] and Huang et al.[8] reached hydrogen uptake of 0.1 wt. % at 10 bar and 0.067 wt. % at 57 bar, respectively. Thermodynamically, hydrogen molecules are incapable of penetrating between the graphene layers in a graphitic structure whereby H_2 adsorption generally restricts to the outermost sheets. The weak binding energy between carbon nanostructure and H_2 at ambient conditions is also another key factor that leads to low H_2 adsorption capacity of this material [14]. For moderate storage conditions, i.e. temperature of ~300 K and pressures no greater than 100 bar, carbon nanostructures are yet to be found that can reproducibly store in excess of 2 wt.% [11]. Thus, surface modifications, such as doping and functionalization have been proposed to enhance gas adsorption property of graphene based materials [14, 20].

So far many theoretical studies, generally performed using standard density-functional theory (DFT), have been devoted to functionalization of carbonous materials with appropriate species, such as transition metals, alkali metals, and alkali-earth metals as

energy storage media. For example, Lebon et al. [12] investigated the adsorption of molecular hydrogen on Ti-doped zigzag graphene nanoribbons (GNR). Hydrogen uptake of GNR decorated with Ti atoms at both sides of the nanoribbons was more than 6 wt% suggesting the potential of this system for hydrogen storage. Lu et al. [21] studied the hydrogen storage properties of Li, Ca, Sc, Ti on graphyne nanotubes and graphene monolayers. They found the hydrogen storage capacity of 4.82 wt%, 5.08 wt%, 4.88 wt%, 4.76 wt% for Li, Ca, Sc, Ti decorated graphyne nanotubes, respectively. Seenithurai et al. [22], used Al-decorated, single-walled carbon nanotube for hydrogen storage based on DFT calculations. They reported that each Al can bind four H_2 molecules without clustering and corresponding storage capacity is 6.15 wt%. Experimental studies on this kind of systems have also been carried out, although they are scarcer than theoretical studies due to the challenges that have to be overcome. For instance, Hudson et al. [23] and Zhou et al. [24] have used Fe and Ni nanoparticles on reduced graphene oxide respectively to show that graphene sheets decorated with Fe and Ni nanoclusters are potential high-capacity hydrogen-storage media. The hydrogen uptake capacity of Fe-graphene was 2.16 wt.% at 77 k and 50 bar while in the case of Ni-graphene hydrogen uptake was 0.14 wt %. at room temperature and a hydrogen pressure of 1 bar and it changed to 1.18 wt.% when hydrogen pressure increased to 60 bar.

Regarding to the preparation methods of graphene-nanoparticle composites, different techniques such as in-situ (e.g., growing the nanoparticles on the graphene surface) and ex-situ (e.g., attaching premade nanoparticles to the graphene surface) methods can be used to anchor nanoparticles to the sheets of graphene, rGO and GO to obtain graphene decorated nanoparticles [25]. GO and rGO are a promising template for anchoring nanoparticles due to the presence of oxygen containing functional groups on their surface and edges. These groups strongly influence the size, shape, and distribution of nanoparticles on the graphene [17, 25]. We briefly explained the techniques that we used in our work below.

- **Chemical impregnation method:** In general, to the in-situ growth of nanoparticles on graphene sheets, a one step method is used in which metal precursor is mixed with GO in an aqueous solution. The oxygen functional groups such as alcohols, carbonyl groups, and acids with negative charge easies the attachment of positively charged

metal ions through electrostatic interactions and the growth of particles on the surface of GO. Although, this method is cost effective and easy to perform, controlling the morphology of particles are difficult in this method [25].

- **Hydrothermal/Solvothermal method:** The hydrothermal/solvothermal method is also commonly used to synthesize inorganic nanoparticles that have a high crystallinity and narrow size distribution on graphene sheets. Generally, hydrothermal/solvothermal necessitate high pressure and long time allowing nucleation/growth of particles and reduction of GO to rGO at the same time. A major advantage of this method over other methods for the formation of graphene sheets decorated by nanoparticles is removing post annealing and calcinations [25].
- **Ex-situ method:** Graphene-nanoparticle composites can also be produced by ex-situ method. In this method, nanoparticles are synthesized separately and added to the graphene suspension. While this method needs more time and steps to complete, it has advantageous compared to in-situ methods including controlling of shape and size of the particles [25].

In all mentioned fabrication methods, keeping reduced graphene oxide from re-stacking the layers is a key factor to retain surface dependent properties of graphene sheets. Metal oxide nanoparticles attached to both side of graphene sheets act as nanobarrier to separate the adjacent graphene layers because of the synergetic effect between graphene and metal oxide [17]. Due to various advantages e.g., suppressing the restacking of graphene layers, good bonding and interfacial interactions with oxygen-containing groups on graphene sheets, fabrication of graphene/metal oxide is expected to be an effective and practical method for increasing the hydrogen storage capacity of graphene [17, 20].

1.2 Perspectives and challenges:

In the work reported herein, an attempt was made to apply graphene-nanoparticle composites as a medium for hydrogen storage. For this aim, we synthesized graphene-nanoparticle composites with different methods including in-situ such as impregnation (chapter 3 and 4), solvothermal (chapter 5) and ex-situ method (chapter 6) to investigate the hydrogen storage behavior of prepared composites. The goal was to develop a unique composite with fully dispersed transition metal oxide nanoparticles on the reduced graphene oxide exhibiting high hydrogen storage capacity.

This thesis is presented in seven chapters. Chapter 1 serves as a general introduction based on previous studies and Chapter 2 presents experimental and different characterization methods that we used in this work.

Chapter 3 (Hydrogen adsorption properties of RGO-MOx (M: Ti, Fe, Ni, and Cu) nanocomposites) discusses the hydrogen adsorption of reduced graphene oxide-metal oxide nanoparticles at a pressure of 9bar and two different temperatures of 298 and 328 k. The isosteric heat of adsorption which shows the strength of bonding between hydrogen and substrate is calculated for all samples.

In chapter 4 (Significant improvement of the hydrogen storage capacity of reduced graphene oxide/TiO_2 nanocomposite by chemical bonding of Ti–O–C), the synthesis of rGO-TiO_2 with different amount of TiO_2 nanoparticles is detailed. Hydrogen uptake of samples is measured at room temperature.

Chapter 5 (Synthesis of anatase TiO_2 with exposed (001) facets grown on N-doped reduced graphene oxide for enhanced hydrogen storage) involves the synthesis of nitrogen doped reduce graphene oxide (NrGO) and followed by decoration of NrGO with active TiO_2 nanoparticles. Hydrogen storage measurements were done at ambient conditions.

In chapter 6 (Decoration of graphene sheets with Pd/Al_2O_3 hybrid particles for hydrogen storage applications), Pd/Al_2O_3 hybrid particles are synthesized and used as a heterogeneous catalyst for enhancement of hydrogen storage capacity of rGO.

Chapter 7 presents conclusions and a general overview of study results and future prospects.

1.3 References

[1] H.G. Shiraz, O. Tavakoli, Investigation of graphene-based systems for hydrogen storage, Renewable and Sustainable Energy Reviews, 74 (2017) 104-109.
[2] K. Pareek, R. Rohan, Z. Chen, D. Zhao, H. Cheng, Ambient temperature hydrogen storage in porous materials with exposed metal sites, International Journal of Hydrogen Energy, 42 (2017) 6801-6809.
[3] A. Grzech, J. Yang, P.J. Glazer, T.J. Dingemans, F.M. Mulder, Effect of long range van der Waals interactions on hydrogen storage capacity and heat of adsorption in large pore silicas, International Journal of Hydrogen Energy, 39 (2014) 4367-4372.
[4] K. Spyrou, D. Gournis, P. Rudolf, Hydrogen Storage in Graphene-Based Materials: Efforts Towards Enhanced Hydrogen Absorption, ECS Journal of Solid State Science and Technology, 2 (2013) M3160-M3169.
[5] H. Barthelemy, M. Weber, F. Barbier, Hydrogen storage: Recent improvements and industrial perspectives, International Journal of Hydrogen Energy, 42 (2017) 7254-7262.
[6] C.-H. Chen, T.-Y. Chung, C.-C. Shen, M.-S. Yu, C.-S. Tsao, G.-N. Shi, C.-C. Huang, M.-D. Ger, W.-L. Lee, Hydrogen storage performance in palladium-doped graphene/carbon composites, International Journal of Hydrogen Energy, 38 (2013) 3681-3688.
[7] A. Ambrosi, A. Bonanni, Z. Sofer, J.S. Cross, M. Pumera, Electrochemistry at Chemically Modified Graphenes, Chemistry – A European Journal, 17 (2011) 10763-10770.
[8] C.-C. Huang, N.-W. Pu, C.-A. Wang, J.-C. Huang, Y. Sung, M.-D. Ger, Hydrogen storage in graphene decorated with Pd and Pt nano-particles using an electroless deposition technique, Separation and Purification Technology, 82 (2011) 210-215.
[9] H.-p. Zhang, X.-g. Luo, X.-y. Lin, X. Lu, Y. Leng, Density functional theory calculations of hydrogen adsorption on Ti-, Zn-, Zr-, Al-, and N-doped and intrinsic graphene sheets, International Journal of Hydrogen Energy, 38 (2013) 14269-14275.
[10] B.P. Vinayan, K. Sethupathi, S. Ramaprabhu, Facile synthesis of triangular shaped palladium nanoparticles decorated nitrogen doped graphene and their catalytic study for renewable energy applications, International Journal of Hydrogen Energy, 38 (2013) 2240-2250.
[11] D.S. Pyle, E.M. Gray, C.J. Webb, Hydrogen storage in carbon nanostructures via spillover, International Journal of Hydrogen Energy, 41 (2016) 19098-19113.
[12] A. Lebon, J. Carrete, L.J. Gallego, A. Vega, Ti-decorated zigzag graphene nanoribbons for hydrogen storage. A van der Waals-corrected density-functional study, International Journal of Hydrogen Energy, 40 (2015) 4960-4968.
[13] H.-J. Choi, S.-M. Jung, J.-M. Seo, D.W. Chang, L. Dai, J.-B. Baek, Graphene for energy conversion and storage in fuel cells and supercapacitors, Nano Energy, 1 (2012) 534-551.
[14] S. Gadipelli, Z.X. Guo, Graphene-based materials: Synthesis and gas sorption, storage and separation, Progress in Materials Science, 69 (2015) 1-60.
[15] W.G. Hong, B.H. Kim, S.M. Lee, H.Y. Yu, Y.J. Yun, Y. Jun, J.B. Lee, H.J. Kim, Agent-free synthesis of graphene oxide/transition metal oxide composites and its

application for hydrogen storage, International Journal of Hydrogen Energy, 37 (2012) 7594-7599.
[16] L. Ma, J.-M. Zhang, K.-W. Xu, Hydrogen storage on nitrogen induced defects in palladium-decorated graphene: A first-principles study, Applied Surface Science, 292 (2014) 921-927.
[17] Z.-S. Wu, G. Zhou, L.-C. Yin, W. Ren, F. Li, H.-M. Cheng, Graphene/metal oxide composite electrode materials for energy storage, Nano Energy, 1 (2012) 107-131.
[18] A.G. Klechikov, G. Mercier, P. Merino, S. Blanco, C. Merino, A.V. Talyzin, Hydrogen storage in bulk graphene-related materials, Microporous and Mesoporous Materials, 210 (2015) 46-51.
[19] G. Srinivas, Y. Zhu, R. Piner, N. Skipper, M. Ellerby, R. Ruoff, Synthesis of graphene-like nanosheets and their hydrogen adsorption capacity, Carbon, 48 (2010) 630-635.
[20] V. Tozzini, V. Pellegrini, Prospects for hydrogen storage in graphene, Physical Chemistry Chemical Physics, 15 (2013) 80-89.
[21] J. Lu, Y. Guo, Y. Zhang, Y. Tang, J. Cao, A comparative study for Hydrogen storage in metal decorated graphyne nanotubes and graphyne monolayers, Journal of Solid State Chemistry, 231 (2015) 53-57.
[22] S. Seenithurai, R.K. Pandyan, S.V. Kumar, C. Saranya, M. Mahendran, Al-decorated carbon nanotube as the molecular hydrogen storage medium, International Journal of Hydrogen Energy, 39 (2014) 11990-11998.
[23] M. Sterlin Leo Hudson, H. Raghubanshi, S. Awasthi, T. Sadhasivam, A. Bhatnager, S. Simizu, S.G. Sankar, O.N. Srivastava, Hydrogen uptake of reduced graphene oxide and graphene sheets decorated with Fe nanoclusters, International Journal of Hydrogen Energy, 39 (2014) 8311-8320.
[24] C. Zhou, J.A. Szpunar, X. Cui, Synthesis of Ni/Graphene Nanocomposite for Hydrogen Storage, ACS Applied Materials & Interfaces, 8 (2016) 15232-15241.
[25] P.T. Yin, S. Shah, M. Chhowalla, K.-B. Lee, Design, Synthesis, and Characterization of Graphene–Nanoparticle Hybrid Materials for Bioapplications, Chemical Reviews, 115 (2015) 2483-2531.

Chapter 2 : Experimental

2.1 Materials

Natural graphite flake (99%), sulfuric acid (H_2SO_4, 98%), sodium nitrate ($NaNO_3$), potassium permanganate ($KMnO_4$), hydrochloric acid (HCl, 37%), copper nitrate trihydrate ($Cu(NO_3)_2 \cdot 3H_2O$), hydrogen peroxide (H_2O_2, 30%), and N-Methyl-2-pyrrolidone (NMP, 97%), and aluminum oxide (Al_2O_3, 99.8%) with primary particle sizes of 13 nm purchased from Sigma-Aldrich. The Al_2O_3 (99.9%) nanoparticles with primary particle size of 220 nm were also purchased from Sumitomo, Jaban. Titanium chloride ($TiCl_3$), nickel chloride ($NiCl_2$), iron chloride ($FeCl_3$), ethanol (C_2H_6O), hydrofluoric acid (HF), and titanium isopropoxide ($C_{12}H_{28}O_4Ti$) were obtained from Merck. All reagents were analytical grade and used without further purification.

2.2. Synthesis of graphite oxide

Graphite flakes were first mixed with sulfuric acid (H_2SO_4) and sodium nitrate ($NaNO_3$) and then potassium permanganate ($KMnO_4$) was added slowly during 2 hours. After completion of oxidation stage, mixture was added to water, filtered, rinsed and, then re-dispersed in 5% HCl solution. Finally, mixture was washed with water till reaching neutral pH and dried at 60°C under vacuum or freeze-dried for further use.

2.3. Synthesis of nanocomposites

2.3.1 Synthesis of RGO-MO_x (M: Ti, Fe, Ni, and Cu) nanocomposites

GO was first sonicated (Vibra Cell 75041, Bioblock Scintific) in water for 2 h to obtain a homogenous dispersion of graphene oxide in aqueous medium. Different amounts of metal salts were then added to the mixture (impregnation method). After stirring for 24 h, suspensions were filtered, vacuum-dried at 60 °C and reduced at 1000 °C for 12 min under argon atmosphere.

2.3.2 Synthesis of TiO_2 with exposed (001) facets and its RGO nanocomposites

Nitrogen-doped graphene (N-rGO) was obtained by treating the as-prepared graphite oxide in a flow of ammonia gas at 1000 °C. In a typical synthesis, 100 mg of N-rGO was dispersed in 50 ml of a mixture of ethanol and NMP (25/1 vol/vol) by ultrasonication for 2

h. The required amount of titanium isopropoxide and HF was added to the solution drop-wise under mechanically stirred conditions. Solvothermal treatment was performed at 150 °C for 24h. The same solvothermal treatment was applied to GO (without ammonia treatment, TiO_2-rGO). Suspensions were filtered, washed by ethanol and vacuum-dried at 60 °C. As a reference, GO was thermally reduced at 1000 °C to attain fully exfoliated reduced graphene oxide (rGO). Preparation of TiO_2-N-rGO as well as TiO_2-rGO nanocomposite was schematically shown in Figure 2.1.

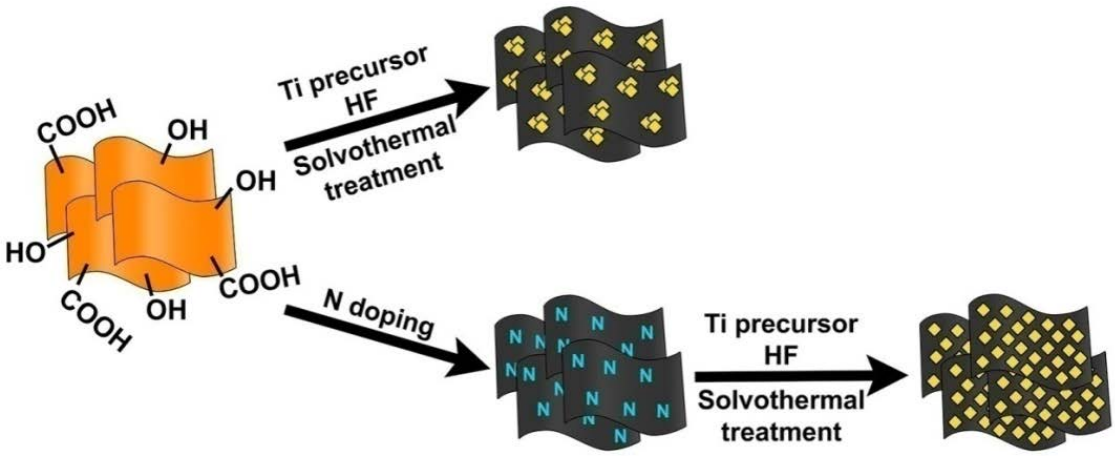

Figure 2.1 Schematic illustration for the fabrication of nanocomposites

2.3.3 Synthesis of Pd/Al_2O_3 hybrid particle and its RGO nanocomposites

The Al_2O_3 nanoparticles were first dispersed in water by ultrasonication. A certain amount of aqueous solution of palladium chloride was added dropwise to this dispersion. The mixture was sonicated for 30 minutes followed by stirring at room temperature for 24 hours. To prepare Pd/Al_2O_3-decorated graphene sheets, GO was dispersed in water for 2 h to obtain a homogenous dispersion (2.25 mg/ml) and then, Pd/Al_2O_3 particles were added to the GO dispersion to reach Al_2O_3/GO of 1/300 (wt/wt). Subsequently, the mixture was sonicated for 30 min and magnetically stirred for 24 h at room temperature. Thereafter, the product was collected by centrifuge, washed with water and vacuum-dried at 60 °C for 3 days. Thermal reduction was carried out with the products at 600 °C for 12 min under argon atmosphere to obtain Pd/Al_2O_3-graphene nanocomposites. As a reference, GO was thermally reduced at 1000 °C to attain fully exfoliated graphene oxide.

2.4 Characterization methods

2.4.1 High resolution transmission electron microscopy (HR-TEM)

HR-TEM was carried out by JEM-ARM 200CF JEOL, Japan with the accelerating voltage of 200 keV. Samples were mildly dispersed in acetone and placed on Cu grid (SPI 200 Mesh Cu, USA).

2.4.2 Scanning electron microscopy (SEM)

SEM equipped with energy dispersive spectroscopy (EDS) was performed by Leo Supra 35VP field emission scanning electron microscope with an acceleration voltage of 2–20kV.

2.4.3 X-Ray powder diffraction (XRD)

XRD were performed using Bruker AXS diffractometer fitted with a Siemens X-ray gun using 0.15406 nm Cu Kα radiation.

2.4.4 Raman spectroscopy

Raman spectroscopic analysis was recorded from samples by using Renishaw inVia reflex Raman spectrometer with a 532 nm laser beam in the range of 100-3500 cm^{-1} while samples were loaded on silica wafer and focused with a 50× objectives.

2.4.5 Specific surface area

The Brunauer-Emmett-Teller (BET) specific surface area and porosity of samples were determined by analyzing the standard nitrogen adsorption-desorption isotherm at 77 K using nova 2200e, Quantachrome instruments.

2.4.6 Hydrogen adsorption

Hydrogen storage capacity of samples was measured by using Intelligent Gravimetric Analyzer (IGA 001, Hiden Isochema). All samples were degassed at 120 °C for 12h under high vacuum (~ 10^{-7} mbar) prior to measurements and then, the hydrogen adsorption isotherm were measured at room temperature and pressures up to 10 bar.

2.4.7 X-ray photoelectron spectroscopy (XPS)

XPS analyses were conducted on a Thermo K-alpha X-ray photoelectron spectrometer with a monochromated Al Kα supported by a low energy electron/ion flood gun for charge neutralization.

2.4.8 Dynamic light scattering (DLS)

Particle size distribution and hydrodynamic radius (r_h) of hybrid particles were measured in aqueous media by Zetasizer nanoseries (Malvern Instruments, Ltd.). DLS measurements were applied to the aqueous suspensions of 0.01 wt. % nanoparticles.

2.4.9 Thermogravimetric analysis (TGA)

TGA was carried out by heating up the nanocomposites at 10 K/min from room temperature to 1300 °C under air atmosphere followed by 3 hours of soaking step at this temperature. Concentration of TiO_2 in each sample was calculated from the difference between residual mass of specimens and RGO and/or N-RGO (reference samples).

Chapter 3 : Hydrogen adsorption properties of RGO-MOx (M: Ti, Fe, Ni, and Cu) nanocomposites

In this chapter preparation and hydrogen adsorption capacity of reduced graphene oxide-metal oxide nanoparticles (RGO-MO_x M: Ti, Fe, Ni, and Cu) was reported. The hydrogen uptake was measured at 298 and 328 k and pressure up to 9 bar. This allows determination of isosteric heat of adsorption. Among nanocomposites, TiO_2-incorporated RGO shows the highest heat of adsorption due to strongly bonds between hydrogen and substrate.

3.1 Introduction

Recently, graphene a single atomic layer sheet of sp^2 bonded carbon atoms attracted many attentions for different applications due to presence unique properties such as high surface area, porous structure, good mechanical and electrical properties etc [1-4]. Various methods are suggested to prepare graphene sheets (single or few layers) in large quantities. As we explained in chapter 1, the most promising method is to use graphene oxide synthesized by the oxidation of graphite. With the reduction of graphene oxide, most of the properties of graphene are reportedly recovered [3]. In order to enhance the hydrogen uptake of graphene samples at ambient conditions, several routes such as functionalization by different species are theoretically investigated [2, 5]. Most of the theoretical works proposed hydrogen enhancement at room temperature and ambient pressures conditions. Because of weak binding of hydrogen molecules and graphene/graphite, many efforts have been devoted to increase both the binding strength and hydrogen storage capacity of graphene samples. Several simulation studies demonstrated the capacity of transition metals decorated on graphene sheets for hydrogen storage [5]. For example, Lu et al. [6] showed the chemical functionalization of graphene with different transition metals such as Sc and Ti and hydrogen uptake of 4.88 wt%, 4.76 wt% in metal decorated graphyne nanotubes, respectively. Ma et.al [4] investigated the structure and hydrogen adsorption behavior of Pd-decorated nitrogen-doped graphene using the DFT calculations. They showed double-side Pd-decorated graphene with nitrogen defects can theoretically reach a gravimetric capacity of 1.99 wt.% hydrogen. Reunchan et al. [7] studied the role of various transition metal atoms such as Sc, V, and Ti on porous graphene for molecular hydrogen adsorption

by first-principles calculations. They reported that these metals can bind to porous graphene and are able to adsorb multiple hydrogen molecules.

In this chapter, reduced graphene oxide was produced from exfoliation of natural graphite by the Hummers' method. The resultant graphene was further decorated with transition metal oxide (TiO_2, NiO, Fe_3O_4 and CuO) nanoparticles by a chemical impregnation technique for the hydrogen storage application. All hydrogen storage measurements were made at two different temperatures and pressures relevant for practical on-board storage systems. Among composites, TiO_2 demonstrated the highest heat of adsorption due to the increased interaction between hydrogen molecules and exposed sites in the nanocomposite.

3.2 Results and discussion

3.2.1 Morphological and structural study

The gas storage capacity of graphene-metal oxide nanocomposites is mainly governed by physical adsorption. This type of adsorption depends on i) distribution, size, and nature of nanoparticles and ii) accessible surface area and pore structure of graphene substrate [2, 13]. We first tracked the dispersion state of nanoparticles by energy dispersive spectroscopy (Figure 3.1). The elemental mapping analysis shows the well-defined spatial distribution of Ti (Figure 3.1i), Fe (Figure 3.1j), Ni (Figure 3.1m), and Cu (Figure 3.1n) confirming the good dispersion of nanoparticles throughout the nanocomposites.

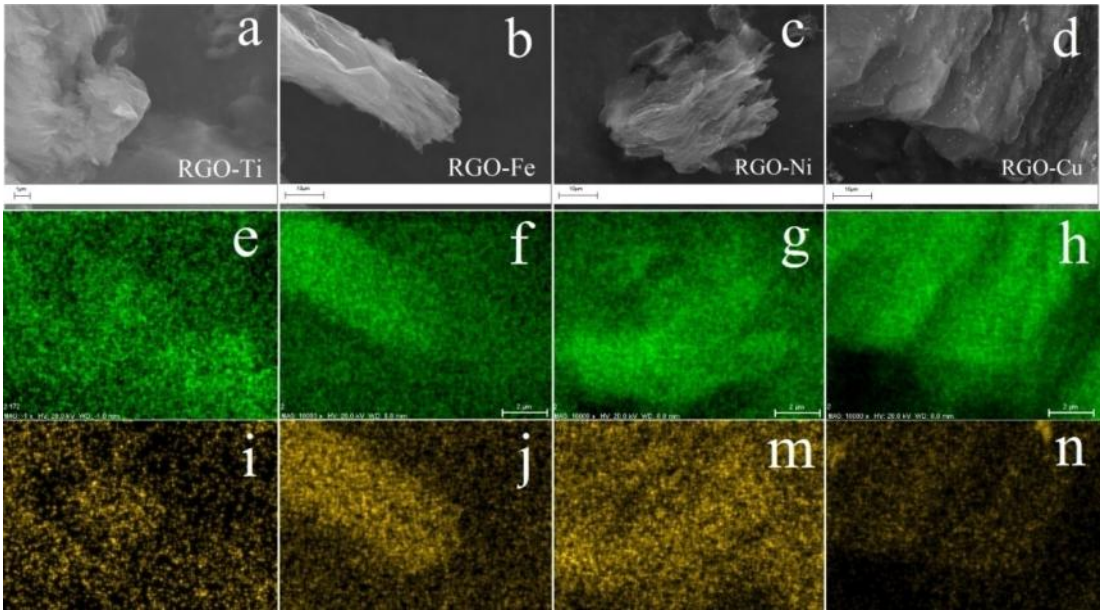

Figure 3.1 Elemental mapping of nanocomposites: selected area (a–f), C-mapping (e–h), Ti-mapping (i), Fe-mapping (j), Ni-mapping (m), and Cu-mapping (n)

Figure 3.2 shows size and distribution of nanoparticles in higher magnification. The RGO-Ti, RGO-Cu, and RGO-Fe displayed particle size of ~ 30 nm, ~ 50 nm, and 50–100 nm, respectively. On the other hand, nanoparticles with size of ~ 200 nm as well as connected networks of nanocrystals were detected in RGO-Ni (inset-top of Figure 3.2c).

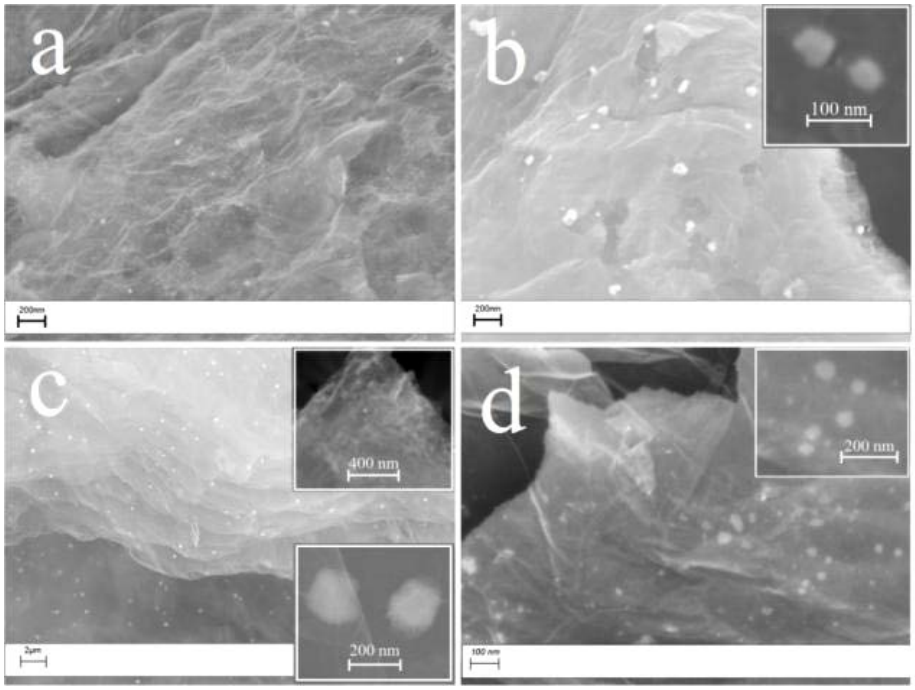

Figure 3.2 SEM images of a) RGO-Ti, b) RGO-Fe, c) RGO-Ni, and d) RGO-Cu, insets show RGO-X nanocomposites in higher magnifications, inset of Figure 2.2c-top shows connected networks of nanocrystals in RGO-Ni

In general, size of nanoparticles plays a key role in gas adsorption behavior of carbon-based nanocomposites—lower the particle size, higher the capacity of the system [14, 15]. Moreover, clustering of nanoparticles often occurs due to the strong cohesion of transition metals. Thus, in order to reduce the size and also avoid the agglomeration of nanoparticles, defects such as oxygen functional groups, structural disorders, and nitrogen doping are introduced to the substrate [11, 16-19]. These defective sites act as nucleation centers and results in formation and pinning of metal crystals onto the substrate [10, 20]. In our system, defective structures mostly comprise oxygen-containing functional groups such as C–OH, C (epoxy/alkoxy)/C=O and O=C–O (carboxylic) groups (Figure 3.3) that intercalate between graphene sheets during oxidation step of graphite flakes.

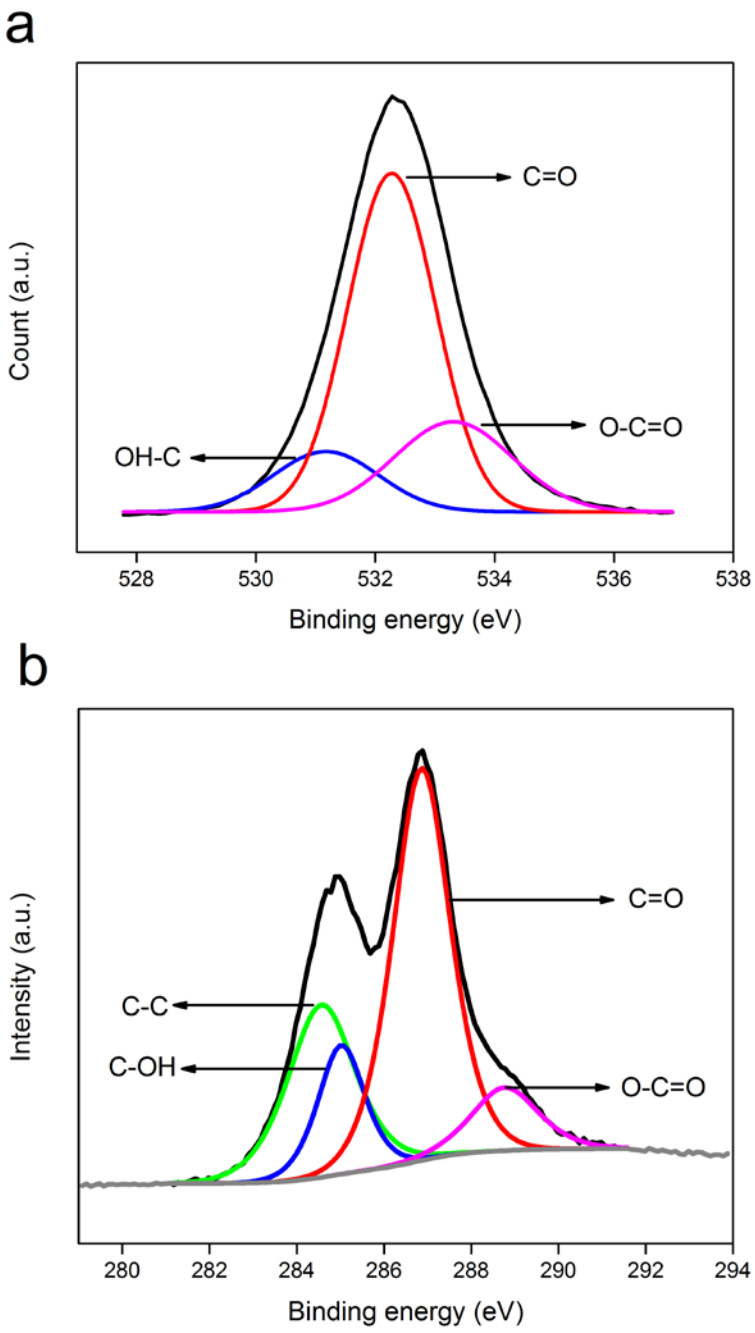

Figure 3.3 XPS spectra of GO a) O 1s scan and b) C 1s scan

Given the similar degree of oxidation in GO substrate—same GO precursor was used for preparation of GO-X nanocomposites, varying size of nanoparticles can be attributed to the difference in tendency of metals ions to interact with oxygen functional groups of the substrate. To elucidate the effect of nature of metal species on their interaction with oxygen

functional groups, the structural change of GO after addition of metal ions was monitored by XRD (Figure 3.4).

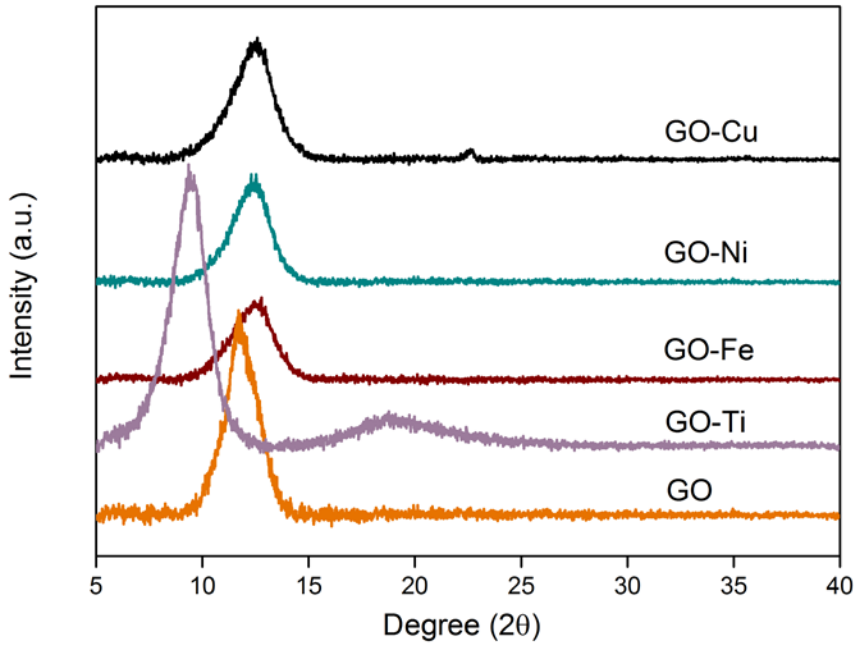

Figure 3.4 XRD patterns of GO and GO-X nanocomposites

Upon addition of Fe, Ni, and Cu, the main peak of GO ($2\theta = 11.7°$ corresponding to (001) plane) shifted to higher 2θ values and also full width at half maximum (FWHM) of the peak increased (Table 3.1) suggesting that GO was partially deoxygenated in the presence of metal ions [21, 22]. This deoxygenation was more pronounced in GO-Cu in such a way that formation of reduced graphene oxide structures was detected through observation of a low intensity peak at $2\theta \approx 23°$. On the other hand, Ti was found to strongly interact with oxygen groups of GO sheets such that a broad peak emerged at $2\theta \approx 20°$ and GO main peak shifts to $2\theta = 9.5°$ (d-spacing of 0.93 nm). While the former illustrates the formation of turbostratic graphite in the system, the latter simply reflects the expansion effect of Ti ion intercalation into GO sheets [23-25]. Therefore, the lower size of nanoparticles in RGO-Ti compared to that of RGO-Fe, Ni, and Cu is expected due to the strong interaction of Ti ions with functional groups of GO sheets.

Table 3.1 XRD parameters of GO and GO nanocomposites

Sample	Main peak (2θ°)	Interlayer spacing (Å)	Full width at half maximum (2θ°)
GO	11.7	7.54	1.66
GO-Ti	9.5	9.34	1.81
GO-Fe	12.48	7.08	2.11
GO-Ni	12.40	7.12	2.11
GO-Cu	12.51	7.06	2.21

It is worth mentioning that neither GO-X (Figure 3.4), nor RGO-X nanocomposites (Figure 3.5) showed characteristic peaks of metal-containing components in XRD patterns that is attributed to the low metal content (Figure 3.6) and small size of nanoparticles (Figure 3.2) [26].

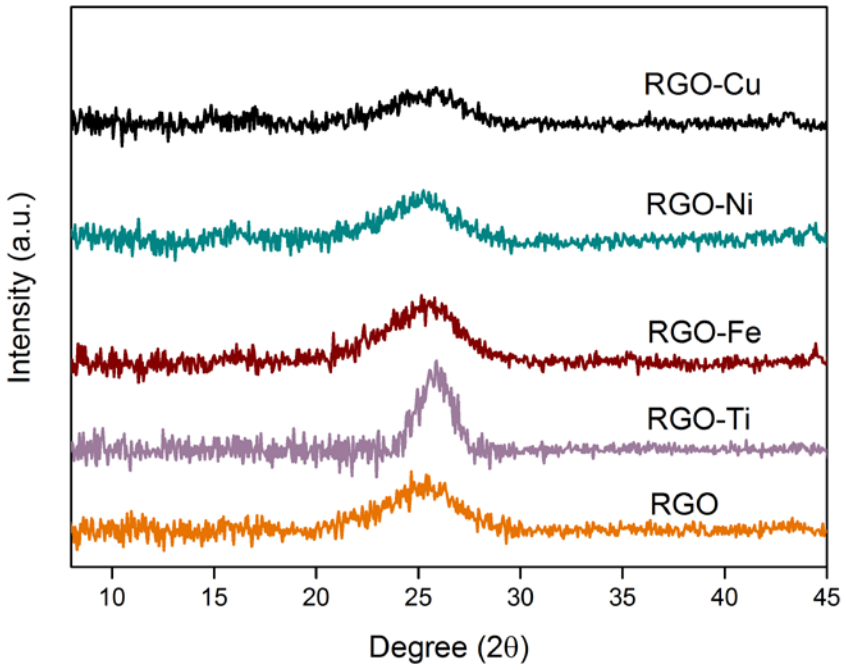

Figure 3.5 XRD patterns of RGO and RGO-X nanocomposites

The concentration of metal oxides in each sample was obtained from the difference between residual mass of RGO-X nanocomposites and RGO sample (reference sample) at the end of the thermogravimetrical analysis. TGA graph of all nanocomposites and references was shown in Figure 3.6. Results indicated the presence of 2.86±0.03 wt% nanoparticles in nanocomposites.

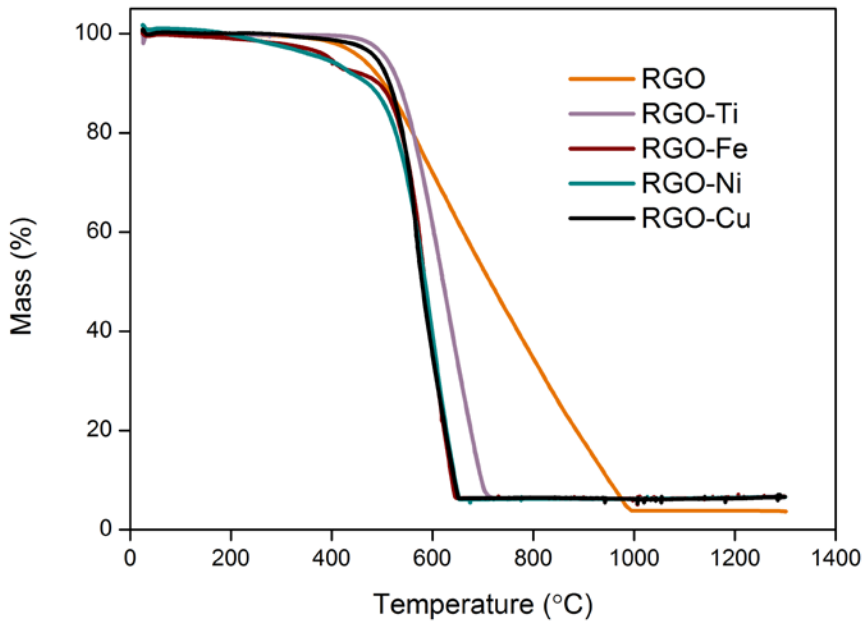

Figure 3.6 Thermogravimetric analysis of RGO and RGO-X nanocomposites

To characterize the structural properties of graphene sheets and nanoparticles, Raman spectroscopy was carried out on reduced graphene oxide samples (Figure 3.7). Raman spectra of graphene and its nanocomposites typically show two Raman shifts at ~ 1350 cm^{-1} (D-band) and ~ 1600 cm^{-1} (G-band). The intensity ratio of the D and G bands (I_D/I_G) is often used to analyze the degree of disorder in graphene layers. The D-band is related to disorder structures in the sp^2 lattice while G-band is attributed to vibration of the sp^2 lattice of 2D hexagonal structure [27, 28]. Upon addition of nanoparticles, the I_D/I_G increased from 1.03 in RGO to 1.05 and 1.06 in RGO-X nanocomposites (Figure 3.7a). This observation illustrates the presence of higher density of defects in graphene substrate possibly originating from nanoparticle–substrate interaction [29].

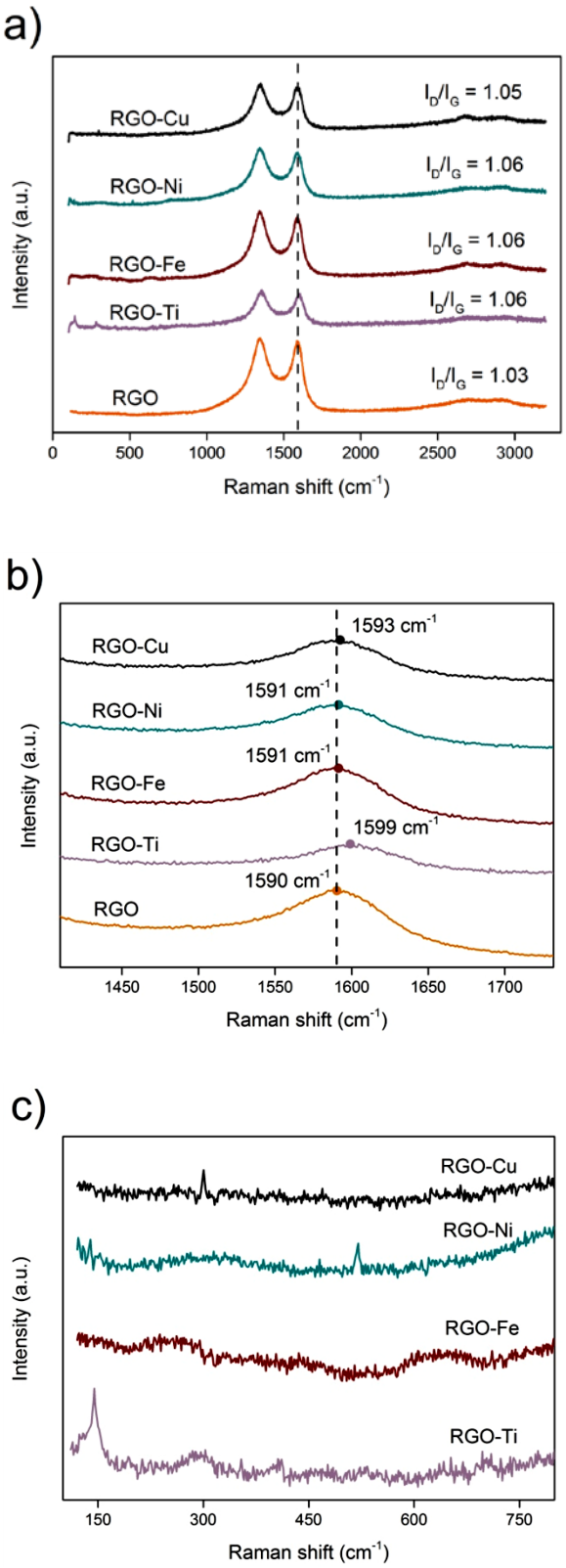

Figure 3.7 Raman spectra of RGO and RGO-X nanocomposites in the range of a) 100–3500 cm^{-1} and b) 1400–1800 cm^{-1} b) 100–800 cm^{-1}

The observed blue-shifts in G-band of RGO-X nanocomposites (Figure 3.7 b) further supports the formation of graphene–nanoparticle interactions [30] that also agrees with the XRD results of GO-X nanocomposites (Figure 3.4). In addition to D and G band, RGO-X nanocomposites display characteristic Raman peaks at 145 cm^{-1} in RGO-Ti, ~ 250 cm^{-1} and ~ 640 cm^{-1} in RGO-Fe, 520 cm^{-1} in RGO-Ni, and 300 cm^{-1} in RGO-Cu (Figure 3.7 c). These peaks are respectively assigned to E_g mode TiO_2 anatase phase [31, 32], E_g and A_{1g} modes of Fe_3O_4 [33, 34], longitudinal optical phonon mode of NiO [35], and A_g mode of CuO [36] and demonstrate the formation of crystalline metal oxide structures in RGO-X nanocomposites.

3.2.2 Gas adsorption behavior of RGO-X nanocomposites

Although incorporated by nanoparticles, hydrogen adsorption behavior of carbon-based nanocomposites is still influenced by accessible surface area and pore structure of the substrate. Porous materials with high surface area and micro-pores of 7–12 Å are desired for H_2 storage application due to high delivery efficiency and fulfilling the volumetric goals at room temperature [37-39]. To assess the specific surface area and pore characteristics of samples, nitrogen adsorption-desorption isotherms (Figure 3.8a) followed by Brunauere-Emmette-Teller (BET) and Barret–Joyner–Halenda (BJH) methods were applied to RGO and RGO-X nanocomposites.

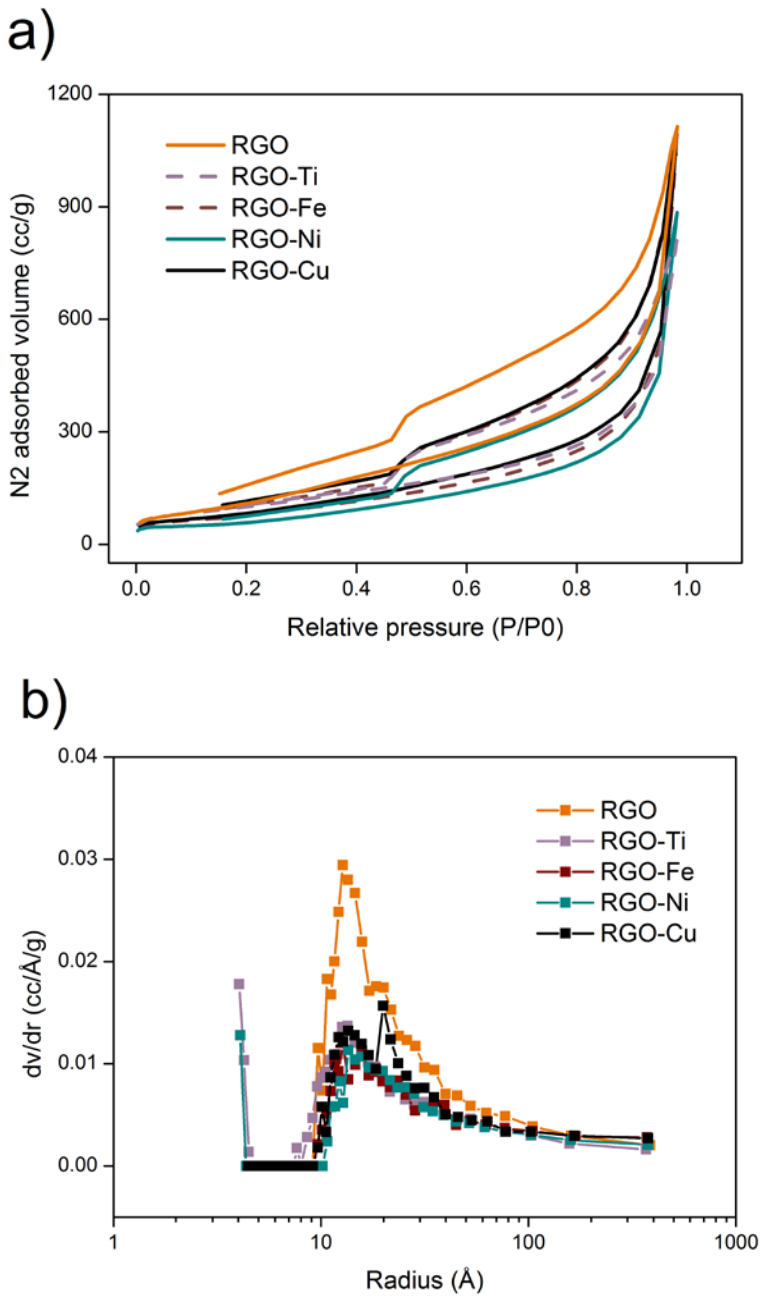

Figure 3.8 a) Nitrogen adsorption-desorption isotherm of RGO and RGO-X nanocomposites and b) pore size distribution of RGO and RGO-X nanocomposites

As seen in Table 3.2, introduction of nanoparticles to graphene sheets reduced the specific surface area and pore-size of samples. The pore-size distribution of RGO-X nanocomposites (Figure 2.8b) also displayed a depressed peak at ~ 12.7 Å compared to that of RGO while the shoulder at ~ 19 Å disappeared in RGO-Ti, Fe, and Ni (blocking effect) [9]. Furthermore, RGO-Ti and Ni showed additional peak at ~ 4 Å indicating that

utilization of Ti and Ni species favors the structural change of the substrate towards preferred pore size.

To track the effect of nanoparticles on hydrogen adsorption behavior of samples, hydrogen adsorption isotherms were carried out. The results of hydrogen adsorption obtained from gravimetric analysis in room temperature and pressures up to 9 bar are summarized in Figure 3.9. As expected, the hydrogen uptake of all samples increased by hydrogen pressure. The maximum hydrogen uptake capacities were found to be 0.4, 0.38, 0.34, 0.33, and 0.16 wt% for rGO-Fe, rGO-Cu, rGO-Ni, rGO-Ti, and rGO, respectively.

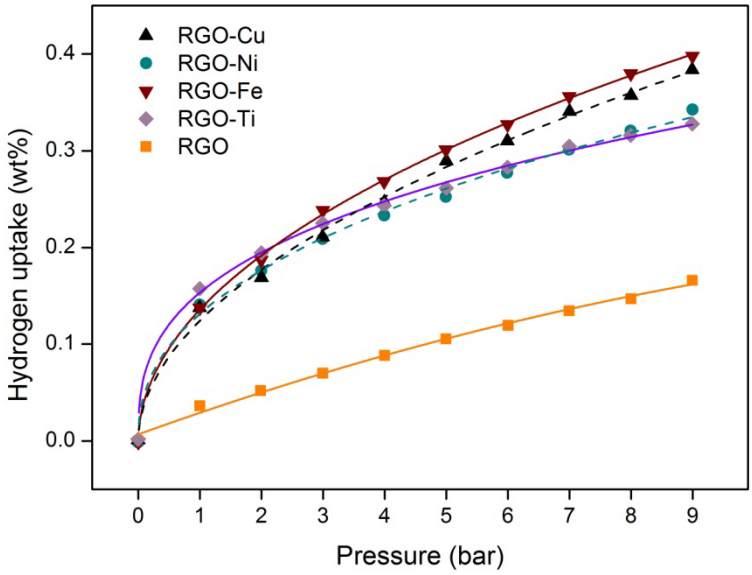

Figure 3.9 H_2 adsorption isotherms of RGO and RGO-X nanocomposites at room temperature

In order to better evaluate the effect of nanoparticles on hydrogen capacity of nanocomposites, results of hydrogen adsorption were normalized with respect to the uptake value of samples at 9 bar and 298 K (Figure 3.10). The adsorption behavior of nanocomposites was found to strongly dependent on the nature of incorporated nanoparticles; for example, the pressure to reach 50% of uptake at 9 bar changed from ~ 4 bar in RGO to ~ 1 bar in RGO-Ti.

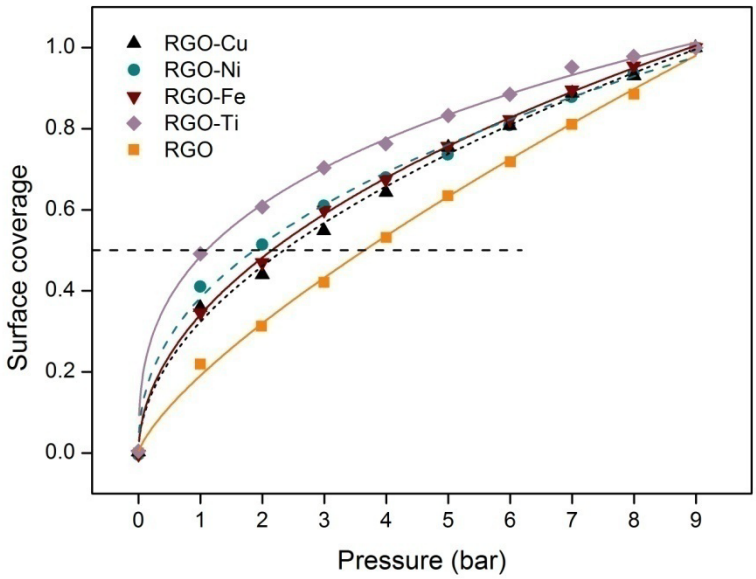

Figure 3.10 Normalized hydrogen uptake RGO and RGO-X nanocomposites at room temperature

To quantify the interaction of composite samples with hydrogen molecules, isosteric heat of adsorption (Qst) were calculated using the Clausius–Clapeyron equation (equation 1) from isotherms measured at 298 K and 328 K.

$$ln\frac{P_2}{P_1} = \frac{q}{R}\left(\frac{1}{T_1} - \frac{1}{T_2}\right) \qquad (1)$$

where q is the isosteric heat of adsorption and R is the ideal gas constant.

The isosteric heats of adsorption as a function of the surface coverage are shown in Figure 3.11a. The isosteric heat calculated for different coverages is corresponded to the strength of interaction between adsorbate and various adsorption sites in adsorbent, therefore, the increased heat of adsorption shows higher hydrogen uptake with lower temperature dependence [40, 41]. Among samples, RGO-Ti displays the highest Qst value due to enhanced interaction between H_2 molecules and exposed active sites in the composite. A correlation between pressure and heat of adsorption at surface coverage of 55% is shown in Figure 3.11b. It is clearly shown that high heat of adsorption leads to high hydrogen uptake at low pressures.

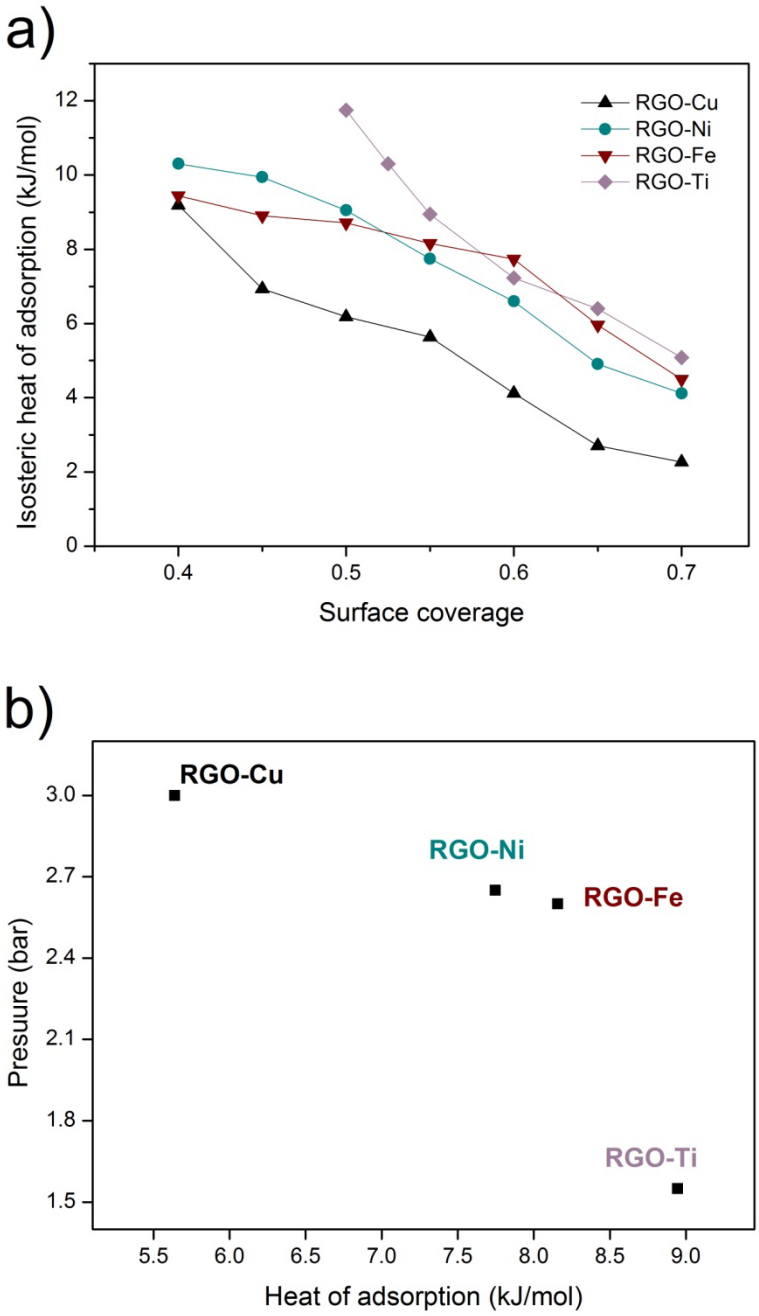

Figure 3.11 a) Isosteric heat of adsorption in dependence of the surface coverage, b) pressure as a function of heat of adsorption at surface coverage of 55%

These results emphasize that incorporation of selected nanoparticles to RGO favors the stronger interaction of hydrogen molecules with the substrate (TiO_2 >Fe_3O_4≅ NiO> CuO). These results are also in agreement with the pore structure of nanocomposites (Table

3.2) showing favorable chemical and structural changes of the substrate when Ti species are utilized.

Table 3.2 Specific surface area, pore radius, and hydrogen uptake of RGO and RGO–X nanocomposites

	S_{BET} (m^2/g)	Pore diameter (Å)	H_2 uptake (wt. %)
RGO	461	25.5	0.16
RGO-Ti	171	8.3	0.33
RGO-Fe	298	20.7	0.40
RGO-Ni	226	8.0	0.34
RGO-Cu	326	24.2	0.38

3.3 Conclusions

A series of reduced graphene oxide-metal oxide nanocomposites (RGO-MO_x, M: Ti, Fe, Ni, and Cu) were prepared via a facile chemical impregnation method. Having interaction with the substrate, incorporation of nanoparticles was shown to improve the hydrogen uptake of the system. The highest storage capacity of 0.4 wt % was obtained by RGO-Fe nanocmposites. When normalized by uptake value of each sample at 9 bar, RGO-Ti demonstrated the highest heat of adsorption due to the increased interaction between hydrogen molecules and exposed sites in the nanocomposite.

3.4 References

[1] H.-J. Choi, S.-M. Jung, J.-M. Seo, D.W. Chang, L. Dai, J.-B. Baek, Graphene for energy conversion and storage in fuel cells and supercapacitors, Nano Energy, 1 (2012) 534-551.
[2] S. Gadipelli, Z.X. Guo, Graphene-based materials: Synthesis and gas sorption, storage and separation, Progress in Materials Science, 69 (2015) 1-60.
[3] W.G. Hong, B.H. Kim, S.M. Lee, H.Y. Yu, Y.J. Yun, Y. Jun, J.B. Lee, H.J. Kim, Agent-free synthesis of graphene oxide/transition metal oxide composites and its application for hydrogen storage, International Journal of Hydrogen Energy, 37 (2012) 7594-7599.
[4] L. Ma, J.-M. Zhang, K.-W. Xu, Hydrogen storage on nitrogen induced defects in palladium-decorated graphene: A first-principles study, Applied Surface Science, 292 (2014) 921-927.

[5] V. Tozzini, V. Pellegrini, Prospects for hydrogen storage in graphene, Physical Chemistry Chemical Physics, 15 (2013) 80-89.
[6] J. Lu, Y. Guo, Y. Zhang, Y. Tang, J. Cao, A comparative study for Hydrogen storage in metal decorated graphyne nanotubes and graphyne monolayers, Journal of Solid State Chemistry, 231 (2015) 53-57.
[7] P. Reunchan, S.-H. Jhi, Metal-dispersed porous graphene for hydrogen storage, Applied Physics Letters, 98 (2011) 093103.
[8] A. Lebon, J. Carrete, L.J. Gallego, A. Vega, Ti-decorated zigzag graphene nanoribbons for hydrogen storage. A van der Waals-corrected density-functional study, International Journal of Hydrogen Energy, 40 (2015) 4960-4968.
[9] C.-H. Chen, T.-Y. Chung, C.-C. Shen, M.-S. Yu, C.-S. Tsao, G.-N. Shi, C.-C. Huang, M.-D. Ger, W.-L. Lee, Hydrogen storage performance in palladium-doped graphene/carbon composites, International Journal of Hydrogen Energy, 38 (2013) 3681-3688.
[10] Z. Wang, C.-J. Liu, Preparation and application of iron oxide/graphene based composites for electrochemical energy storage and energy conversion devices: Current status and perspective, Nano Energy, 11 (2015) 277-293.
[11] Z.-S. Wu, G. Zhou, L.-C. Yin, W. Ren, F. Li, H.-M. Cheng, Graphene/metal oxide composite electrode materials for energy storage, Nano Energy, 1 (2012) 107-131.
[12] S. Yang, Y. Sun, L. Chen, Y. Hernandez, X. Feng, K. Müllen, Porous Iron Oxide Ribbons Grown on Graphene for High-Performance Lithium Storage, Scientific Reports, 2 (2012) 427.
[13] H.G. Shiraz, O. Tavakoli, Investigation of graphene-based systems for hydrogen storage, Renewable and Sustainable Energy Reviews, 74 (2017) 104-109.
[14] C.-S. Tsao, Y.-R. Tzeng, M.-S. Yu, C.-Y. Wang, H.-H. Tseng, T.-Y. Chung, H.-C. Wu, T. Yamamoto, K. Kaneko, S.-H. Chen, Effect of Catalyst Size on Hydrogen Storage Capacity of Pt-Impregnated Active Carbon via Spillover, The Journal of Physical Chemistry Letters, 1 (2010) 1060-1063.
[15] R.C. Lochan, M. Head-Gordon, Computational studies of molecular hydrogen binding affinities: The role of dispersion forces, electrostatics, and orbital interactions, Physical Chemistry Chemical Physics, 8 (2006) 1357-1370.
[16] G. Kim, S.-H. Jhi, N. Park, Effective metal dispersion in pyridinelike nitrogen doped graphenes for hydrogen storage, Applied Physics Letters, 92 (2008) 013106.
[17] H. Wang, J.T. Robinson, G. Diankov, H. Dai, Nanocrystal Growth on Graphene with Various Degrees of Oxidation, Journal of the American Chemical Society, 132 (2010) 3270-3271.
[18] Z.G. Bajestani, A. Yurum, Y. Yurum, Significant improvement in the hydrogen storage capacity of a reduced graphene oxide/TiO2 nanocomposite by chemical bonding of Ti-O-C, RSC Advances, 6 (2016) 32831-32838.
[19] Z. Gohari-Bajestani, O. Akhlaghi, Y. Yürüm, A. Yürüm, Synthesis of anatase TiO2 with exposed (001) facets grown on N-doped reduced graphene oxide for enhanced hydrogen storage, International Journal of Hydrogen Energy.
[20] V. Singh, D. Joung, L. Zhai, S. Das, S.I. Khondaker, S. Seal, Graphene based materials: Past, present and future, Progress in Materials Science, 56 (2011) 1178-1271.
[21] S. Li, Z. Chen, Y. Jin, S. Chen, H. Wang, J. Geng, Q. Song, X. Yang, L. Ma, S. Li, Z. Qin, C. Zheng, A new approach for preparation of magnetite–graphite composite: Intercalation of polyhydroxy iron cation into graphite oxide in l-arginine medium, Solid State Sciences, 13 (2011) 862-866.

[22] H.L. Poh, F. Sanek, A. Ambrosi, G. Zhao, Z. Sofer, M. Pumera, Graphenes prepared by Staudenmaier, Hofmann and Hummers methods with consequent thermal exfoliation exhibit very different electrochemical properties, Nanoscale, 4 (2012) 3515-3522.
[23] T. Szabó, A. Bakandritsos, V. Tzitzios, E. Devlin, D. Petridis, I. Dékány, Magnetically Modified Single and Turbostratic Stacked Graphenes from Tris(2,2′-bipyridyl) Iron(II) Ion-Exchanged Graphite Oxide, The Journal of Physical Chemistry B, 112 (2008) 14461-14469.
[24] Z.Q. Li, C.J. Lu, Z.P. Xia, Y. Zhou, Z. Luo, X-ray diffraction patterns of graphite and turbostratic carbon, Carbon, 45 (2007) 1686-1695.
[25] P.-Y. Chen, M. Liu, T.M. Valentin, Z. Wang, R. Spitz Steinberg, J. Sodhi, I.Y. Wong, R.H. Hurt, Hierarchical Metal Oxide Topographies Replicated from Highly Textured Graphene Oxide by Intercalation Templating, ACS Nano, 10 (2016) 10869-10879.
[26] H. Zhou, J. Zhang, J. Zhang, X. Yan, X. Shen, A. Yuan, High-capacity room-temperature hydrogen storage of zeolitic imidazolate framework/graphene oxide promoted by platinum metal catalyst, International Journal of Hydrogen Energy, 40 (2015) 12275-12285.
[27] M. Giovanni, H.L. Poh, A. Ambrosi, G. Zhao, Z. Sofer, F. Sanek, B. Khezri, R.D. Webster, M. Pumera, Noble metal (Pd, Ru, Rh, Pt, Au, Ag) doped graphene hybrids for electrocatalysis, Nanoscale, 4 (2012) 5002-5008.
[28] X. Wang, X. Zhang, Electrochemical co-reduction synthesis of graphene/nano-gold composites and its application to electrochemical glucose biosensor, Electrochimica Acta, 112 (2013) 774-782.
[29] A. Ambrosi, A. Bonanni, Z. Sofer, J.S. Cross, M. Pumera, Electrochemistry at Chemically Modified Graphenes, Chemistry – A European Journal, 17 (2011) 10763-10770.
[30] Y. Haldorai, W. Voit, J.-J. Shim, Nano ZnO@reduced graphene oxide composite for high performance supercapacitor: Green synthesis in supercritical fluid, Electrochimica Acta, 120 (2014) 65-72.
[31] H. Yoshitake, D. Abe, Raman spectroscopic study of the framework structure of amorphous mesoporous titania, Microporous and Mesoporous Materials, 119 (2009) 267-275.
[32] K. Li, T. Chen, L. Yan, Y. Dai, Z. Huang, J. Xiong, D. Song, Y. Lv, Z. Zeng, Design of graphene and silica co-doped titania composites with ordered mesostructure and their simulated sunlight photocatalytic performance towards atrazine degradation, Colloids and Surfaces A: Physicochemical and Engineering Aspects, 422 (2013) 90-99.
[33] L. Zhang, F. Zhang, W.-F. Dong, J.-F. Song, Q.-S. Huo, H.-B. Sun, Magnetic-mesoporous Janus nanoparticles, Chemical Communications, 47 (2011) 1225-1227.
[34] Y. Jiang, Z.-J. Jiang, L. Yang, S. Cheng, M. Liu, A high-performance anode for lithium ion batteries: Fe3O4 microspheres encapsulated in hollow graphene shells, Journal of Materials Chemistry A, 3 (2015) 11847-11856.
[35] B. Zhao, J. Song, P. Liu, W. Xu, T. Fang, Z. Jiao, H. Zhang, Y. Jiang, Monolayer graphene/NiO nanosheets with two-dimension structure for supercapacitors, Journal of Materials Chemistry, 21 (2011) 18792-18798.
[36] L. Debbichi, M.C. Marco de Lucas, J.F. Pierson, P. Krüger, Vibrational Properties of CuO and Cu4O3 from First-Principles Calculations, and Raman and Infrared Spectroscopy, The Journal of Physical Chemistry C, 116 (2012) 10232-10237.

[37] Z. Gohari Bajestani, A. Yürüm, Y. Yürüm, Decoration of graphene sheets with Pd/Al2O3 hybrid particles for hydrogen storage applications, International Journal of Hydrogen Energy, 41 (2016) 9810-9818.
[38] L. Wei, Y. Mao, Enhanced hydrogen storage performance of reduced graphene oxide hybrids with nickel or its metallic mixtures based on spillover mechanism, International Journal of Hydrogen Energy, 41 (2016) 11692-11699.
[39] A.G. Klechikov, G. Mercier, P. Merino, S. Blanco, C. Merino, A.V. Talyzin, Hydrogen storage in bulk graphene-related materials, Microporous and Mesoporous Materials, 210 (2015) 46-51.
[40] K.C. Kemp, C. Vimlesh, S. Muhammad, S.K. Kwang, Reversible CO 2 adsorption by an activated nitrogen doped graphene/polyaniline material, Nanotechnology, 24 (2013) 235703.
[41] B. Schmitz, U. Müller, N. Trukhan, M. Schubert, G. Férey, M. Hirscher, Heat of Adsorption for Hydrogen in Microporous High-Surface-Area Materials, ChemPhysChem, 9 (2008) 2181-2184.

Chapter 4 : Significant improvement of the hydrogen storage capacity of reduced graphene oxide/TiO_2 nanocomposite by chemical bonding of Ti–O–C

In this chapter we report the preparation and characterization of TiO_2-integrated graphene nanocomposites with different amount of TiO_2 nanoparticles that is synthesized via facile chemical impregnation method [1]. Higher hydrogen uptake of nanocomposites compared to that of graphene sample was linked to strong attachment of highly distributed nanoparticles to the underlying graphene sheets.

4.1 Introduction

Finding materials for efficient hydrogen storage is one the most important components for adoption of hydrogen in future of renewable energies. Thus, introduction of metal/metal oxide components to graphene layers have been proposed to enhance gas adsorption property of graphene based materials [2, 3].

TiO_2 has been widely studied due to its photochemical, catalytic and dielectric characteristics. Theoretical studies showed the potential of Ti/TiO_2-anchored carbonaceous materials [4-6] as the hydrogen storage media for room-temperature applications. Recent experimental results on TiO_2-decorated expanded graphite [7] and TiO_2-carbon nanotubes (CNT) composites [8, 9] revealed the enhanced electrochemical hydrogen uptake of graphene and higher H_2 gas adsorption of CNT after impregnation with TiO_2 nanoparticles. In this chapter effects of content, dispersion state and size of TiO_2 nanoparticles on hydrogen storage capacity of graphene nanocomposites (referred to GO-TX in case of graphite oxide nanocomposites and RGO-TX in case of reduced graphene oxide nanocomposites, X: 3, 5, and 7) were studied.

4.2 Results and discussion

4.2.1 Characterization of nanocomposites

X-ray diffraction (XRD) was first carried out to determine the crystallographic structure of samples. As shown in Figure 4.1a, natural graphite flakes show a sharp peak at $2\theta = 26°$ that corresponds to (002) plane and an interlayer spacing (d-spacing) of 3.3 Å. Upon oxidation, the (002) peak disappeared and a low intensity peak, indexed as (001),

emerged at $2\theta \approx 10.5°$ with d-spacing of 8.4 Å. This increase of the d-spacing after oxidation has been correlated with intercalation of oxygen-containing groups between graphene layers that leads to change of the crystallographic structure of graphite [10]. After inclusion of Ti, intensity and full width at half maximum (FWHM) of the characteristic peak of graphite oxide ($2\theta \approx 10.5°$) were changed. In addition, a new peak centered at $2\theta \approx 25°$ was observed in GO-T5 and GO-T7 whereas no peak was detected at this region in GO-T3. Given the characteristic peak of TiO_2 (101) at $2\theta \approx 25°$ [11], former observation can be attributed to formation of TiO_2 in the samples. On the other hand, absence of this peak in GO-T3 can be related to the low metal content and/or small size of particles [10]. Besides, progressive increase of FWHM and decrease of the intensity of GO main peak by Ti content suggests that GO was partially deoxygenated in the presence of Ti and reduced to turbostratic graphite.[12] Consequently, appearance of the peak at $2\theta \approx 25°$ can also represent the formation of turbostratic graphite structures in the sample. Indeed, formation of turbostratic graphite coincides with the formation of TiO_2 particle in specimens. According to Li et al. [13], increase of FWHM of graphene layers correlates with non-uniformity in d-spacing, curvature and more importantly distortion of the layers. As a result, Ti component which intercalates between graphene oxide layers possibly forms structural defects in the system. Figure 4.1b shows XRD patterns of thermally reduced GO samples before and after addition of Ti. Observation of a broad and low-intensity (002) peak in the absence of (001) peak in RGO indicates the complete reduction of graphite oxide sheets and formation of poorly ordered graphene-like structure along the stacking direction. On the same basis, absence of GO peak at $\approx 10.5°$ was used as a clear indication of reduction of graphite oxide sheets in RGO-T nanocomposites [11, 14].

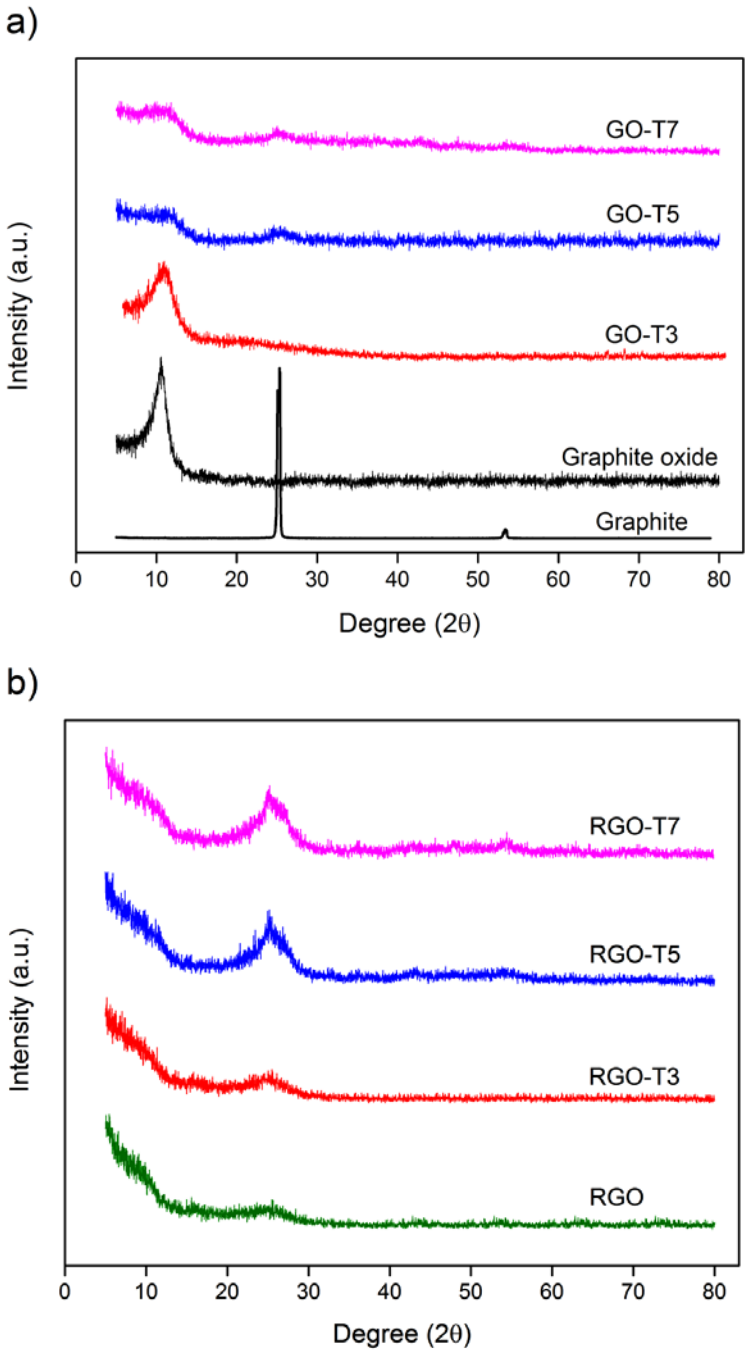

Figure 4.1 XRD patterns of a) GO and b) RGO samples with increasing amount of Ti addition

Raman spectroscopy was used to study the structural properties of particles and quality of graphene sheets, particularly defects and ordering in the system [15]. Figure 4.2 displays the Raman spectra of graphite oxide, RGO and RGO-T nanocomposites with typical characteristic bands at ~1600 cm^{-1} and ~1350 cm^{-1}, known as G-band and D-band,

respectively. G-band corresponds to vibration of the sp^2-bonded carbon atoms in a 2D hexagonal lattice while D-band represents in-plane stretching motion of symmetric sp^2 C−C bonds [16, 17]. To analyze the degree of disorder in graphitic layers, intensity ratio of the D and G bands (I_D/I_G) has been widely used in literature [16-18]. The I_D/I_G of 0.88 was calculated from Raman spectrum of GO sample while higher I_D/I_G was observed in Raman spectra of RGO and RGO-T nanocomposites. This increased I_D/I_G points out the formation of higher density of defects during the deposition of particles that is a result of the interaction between particles and graphene sheets [18, 19].

Besides the G and D bands, a low intensity peak emerged at 151 ± 1 cm^{-1} in RGO-T nanocomposites. This peak was assigned to E_g mode of TiO_2 and arises from the external vibration of anatase phase [20-23]. Inset of Figure 3.2 magnifies the wavenumber of 100–900 cm^{-1} in RGO-T7 that shows two vibration peaks at 400 cm^{-1} ($B_{1g(1)}$) and 635 cm^{-1} ($Eg_{(2)}$) in addition to E_g mode of TiO_2. This observation confirms the formation of anatase TiO_2 in RGO-T nanocomposites after thermal reduction process [20-23]. However, a large frequency blue-shift of E_g was detected in RGO-T nanocomposites compared to E_g of anatase single crystal (144 cm^{-1}). A similar large frequency shift was also reported by Zheng et al. [24] for TiO_2 nanocrystals fabricated by solution chemical process. They showed when dimensions of TiO_2 crystallites decrease to nanometer scale, frequency shift occurs in E_g mode as a result of phonon confinement.

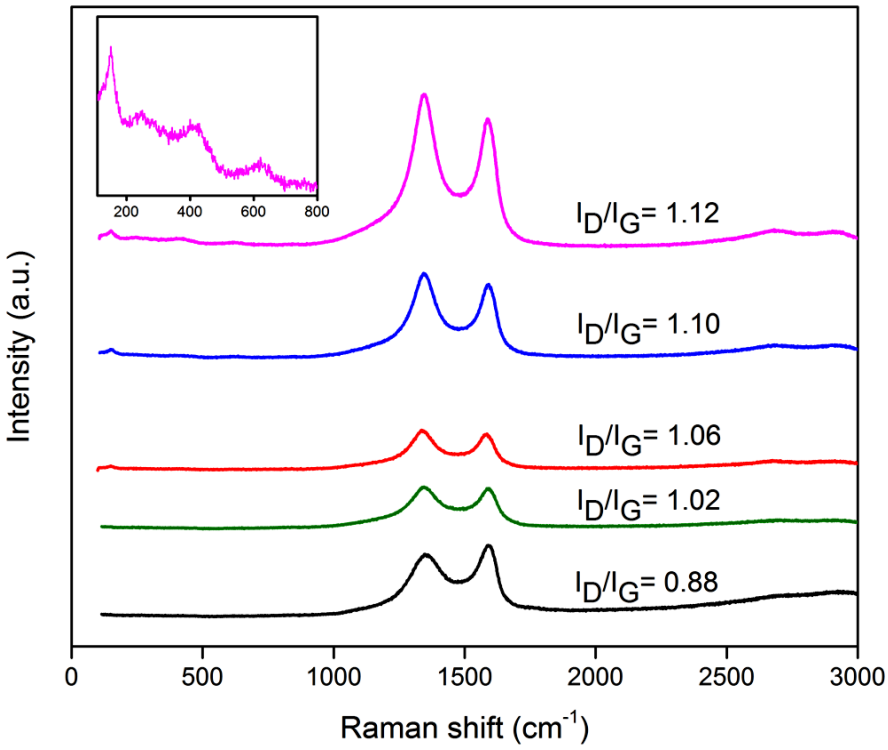

Figure 4.2 Raman spectra of graphite oxide, RGO and RGO-T nanocomposites, from bottom to top: graphite oxide, RGO, RGO-T3, RGO-T5 and RGO-T7. Inset magnifies the wavenumber of 100–900 cm-1 in RGO-T7

Distribution and size of the particles in RGO-T nanocomposites were studied using scanning electron microscopy (SEM), energy dispersive spectroscopy (EDS), and transmission electron microscopy (TEM). Figure 4.3a–c show high magnification SEM images of samples demonstrating the parent graphene sheets are coated with TiO_2 nanoparticles. RGO-T3 and T5 display homogenous dispersion of nanoparticles while excess amount of Ti led to inhomogeneous deposition, growth and formation of submicron aggregation of nanoparticles in RGO-T7. The elemental analysis of RGO-T3 was provided in Figure 4.3d–f as representative EDS results of RGO-T nanocomposites. Detection of distributed patterns of Ti and O in the elemental mapping confirms the homogeneous deposition of TiO_2 nanoparticles throughout the sample.

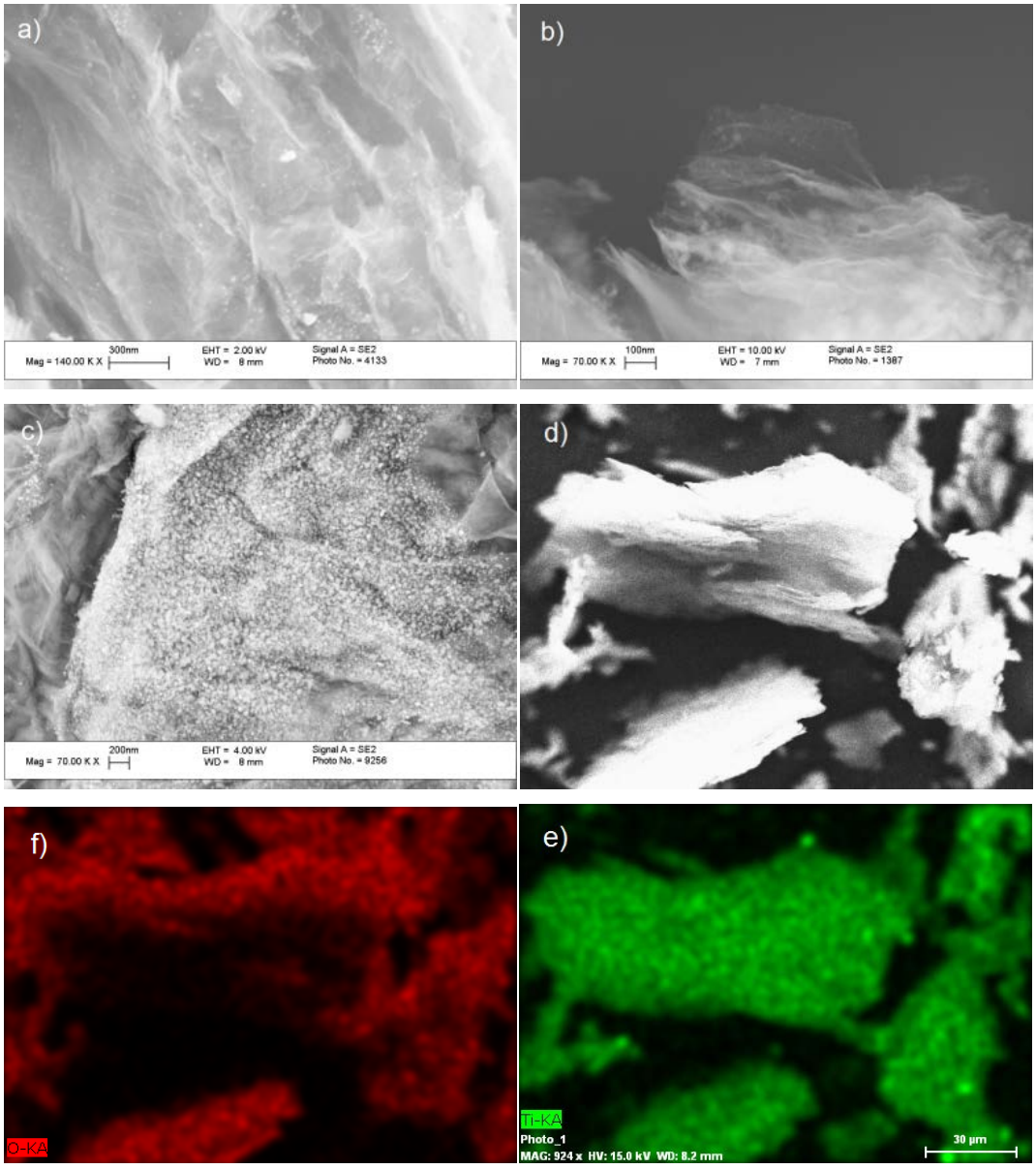

Figure 4.3 a) SEM images of RGO-T3, b) RGO-T5, and c) RGO-T7, d) SEM image of RGO-T3 with low magnification, e) Ti and f) O elemental mapping of same area shown in Figure 3.3d

TEM micrographs of RGO and RGO-T nancomposites were presented in Figure 4.4 a–d. Wrinkled structured graphene sheets were clearly observed that indicates the formation of few layer graphene layers in all samples after thermal exfoliation. Homogeneous dispersion of TiO_2 nanoparticles was detected as dark spots in TEM micrographs shown in Figure 4.4 b–d. Size of TiO_2 nanoparticles in RGO-T3 was found to be 10 ± 5 nm whereas higher amounts of Ti addition introduced higher average of particle sizes in RGO-T7.

According to Wu et al.[4] and Wang et al. [25] size, morphology and anchoring of nanocrystals are dependent on the degree of oxidation of the underlying substrate. It is thought that Ti component could use the oxygen functional groups as nucleation centers. As a result, highly oxidized GO surface with high concentration of defects interacts strongly with particles and this strong pinning force hinders the diffusion and growth of formed particles [19, 26]. Tsao et al. [27] showed that size of the catalyst particles plays an important role in H_2 uptake in which Pt nanoparticles of 1–2 nm remarkably increased the H_2 storage capacity of Pt/activated carbon nanocomposite. Therefore, formation of fine and distributed nanoparticles is highly preferred in order to increase the hydrogen adsorption capacity of RGO-T nanocomposites.

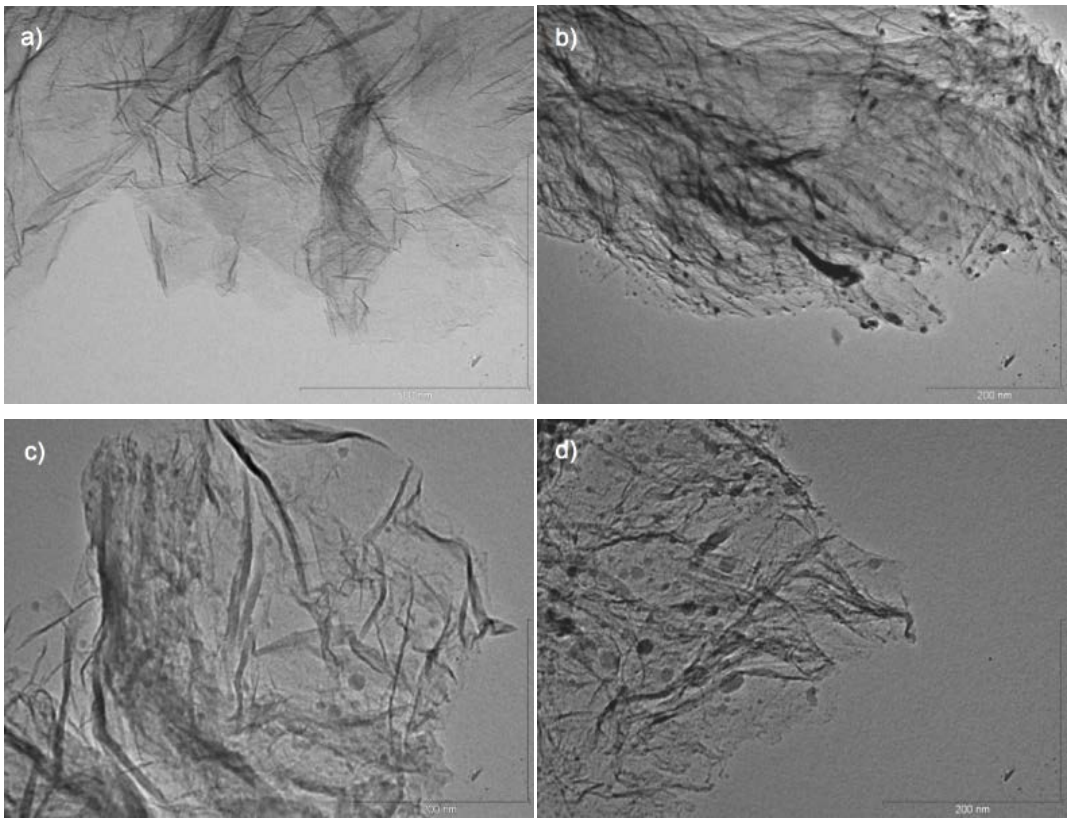

Figure 4.4 TEM micrograph of a) RGO, b) RGO-T3, c) RGO-T5, and d) RGO-T7

X-ray photoelectron spectroscopy (XPS) was performed to elucidate the chemical state of elements present in GO, RGO and RGO-T nanocomposites. Figure 4.5a depicts a representative XPS survey spectrum (RGO-T5) that shows specimens mainly consist of C and O with no trace of contamination. The presence of Ti was detected in RGO-T

nanocomposites with a weak signal at ~ 459 eV that corresponds to Ti 2p electrons [28]. Figure 4.5b depicts C 1s XPS spectrum of GO with four peaks centered at 284.56, 285.02, 286.8 and 288.8 eV. These peaks were assigned to the C–C (aromatic) [29], C–OH [19], C (epoxy/ alkoxy)/C=O[30] and O=C–O (carboxylic) [23] groups respectively that imply the highly oxidized state of graphene sheets. After thermal reduction, the intensity of components associated with oxygenated functional groups significantly decreased (Figure 4.5c). This decrease illustrates that most of the oxygen-containing functional groups are removed and GO is transformed to graphene [23]. In Figure 4.5d, Ti2p XPS spectra of RGO-T nanocomposites exhibited two peaks centered at 464.7 ± 0.1 and 459 ± 0.2 eV assigned respectively to the Ti 2p1 and Ti 2p3 spin−orbital splitting photoelectrons in the Ti^{4+} state. The splitting energy between two Ti-bands was 5.69 ± 0.02 eV that is in agreement with the normal state of Ti^{4+} [11, 31, 32]. As TiO_2 content was increased, Ti 2p3 peak narrowed (decrease of FWHM) and binding energies of Ti 2p feature shifted toward higher binding energies. According to Oh et al. [33] increasing thickness of deposited TiO_2 leads to the blue shift of Ti core level and decrease of FWHM of the Ti 2p3 peak. Therefore, observation of shifting and narrowing Ti 2p3 peak with Ti content can be related to change of the dimensions of nanoparticles that is in agreement with TEM micrographs of RGO-T nanocomposites.

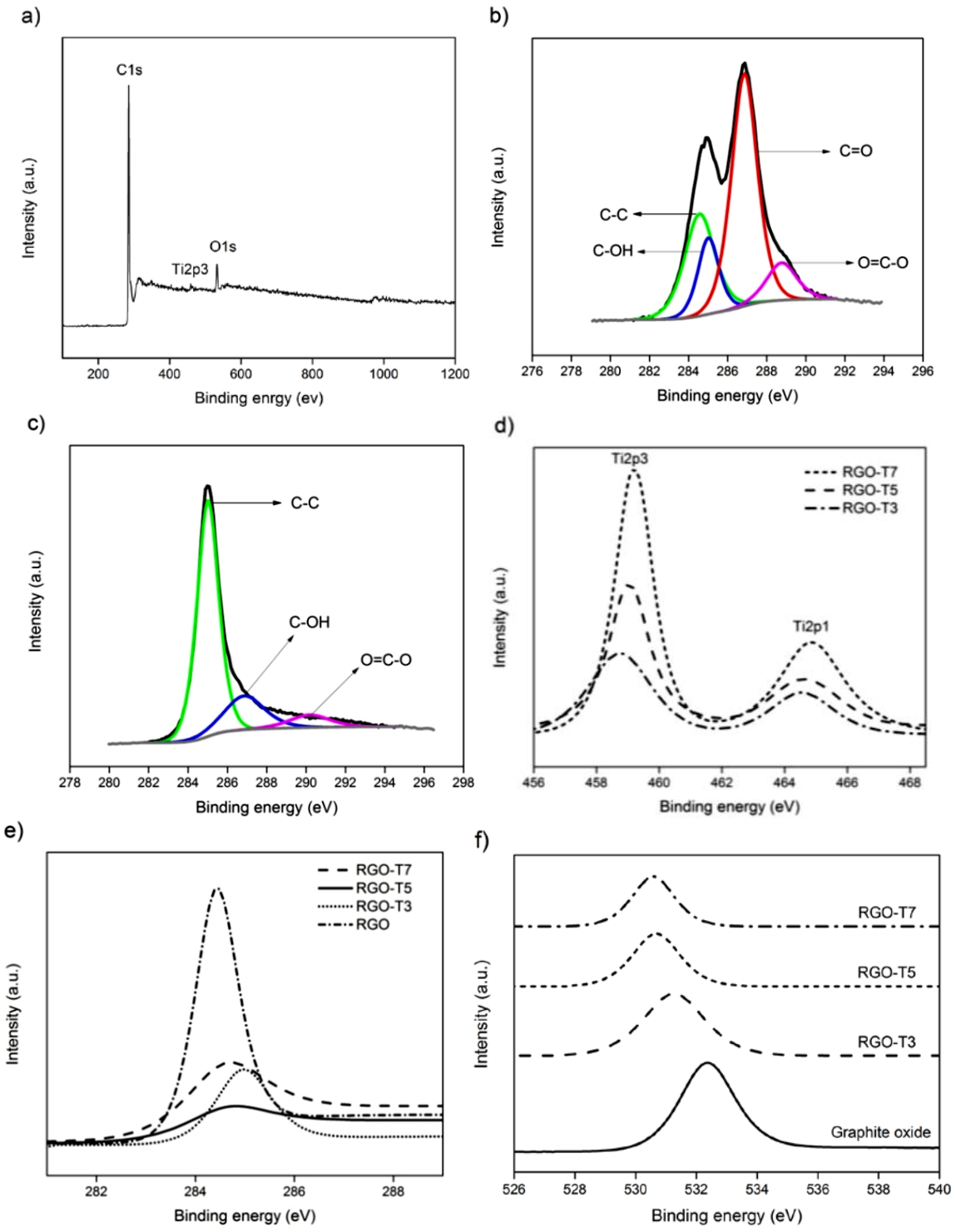

Figure 4.5 a) XPS survey spectra, b) C 1s XPS spectrum of GO, c) C 1s XPS spectrum of RGO, d) Ti2p XPS spectra of RGO-T, e) C 1s XPS spectra of RGO-T nanocomposite, and O 1s XPS spectra of GO and RGO-T nanocomposites

The C 1s XPS spectra of RGO-T nanocomposite was presented in Figure 4.5e with superimposition of C 1s XPS of RGO for comparison. All RGO-T nanocomposites showed the main peak at 284.7 ± 0.2 eV (C–C aromatic band) in which the FWHM of the peak increased from 1.02 eV in RGO to 1.3, 2.01 and 1.9 eV in RGO-T3, T5 and T7, respectively. The FWHM of the C1s core level band has been used to evaluate the degree of chemical and structural heterogeneity in environment of carbon atoms [34, 35]. Therefore, it can be concluded that environment of carbon atoms becomes more heterogeneous through the addition of Ti suggesting the bonding of TiO_2 nanoparticles with C atoms in graphene sheets. To further support the presence of this bonding, O 1s XPS spectra of graphite oxide and RGO-T nanocomposites were depicted in Figure 4.5f. The O 1s spectrum of graphite oxide shows a peak centered at 532.5 eV that is closely related to the hydroxyl groups on the surface of graphite oxide sheets. However, this peak was shifted to 530.6 ± 0.1 eV in RGO-T nanocomposites. In agreement with previous reports in bonding of Ti atoms with any available oxygen to form TiO_2 [36, 37] this peak was assigned as bonding energy of O in Ti−O−C bond [38, 39]. As a result, bonding between Ti, O, and C confirms the integration of nanoparticles into graphene sheets.

4.2.2 Gas adsorption behavior

Nitrogen adsorption-desorption isotherm was employed to characterize the specific surface area and pore structure of nanocomposites (Figure 4.6a). According to the IUPAC classification, all samples showed a nature of type IV curve, that is, a low N_2 adsorption capacity at low relative pressure (P/P_0) followed by a hysteresis loop at high P/P_0. The former indicates the presence of small number of micropores while the latter reflects the formation of mesoporous structures in the system [40]. Higher N_2 adsorption of pristine graphene than that of RGO-T illustrates the lower adsorption capability of RGO after deposition of nanoparticles when physical adsorption is the dominant process [41].

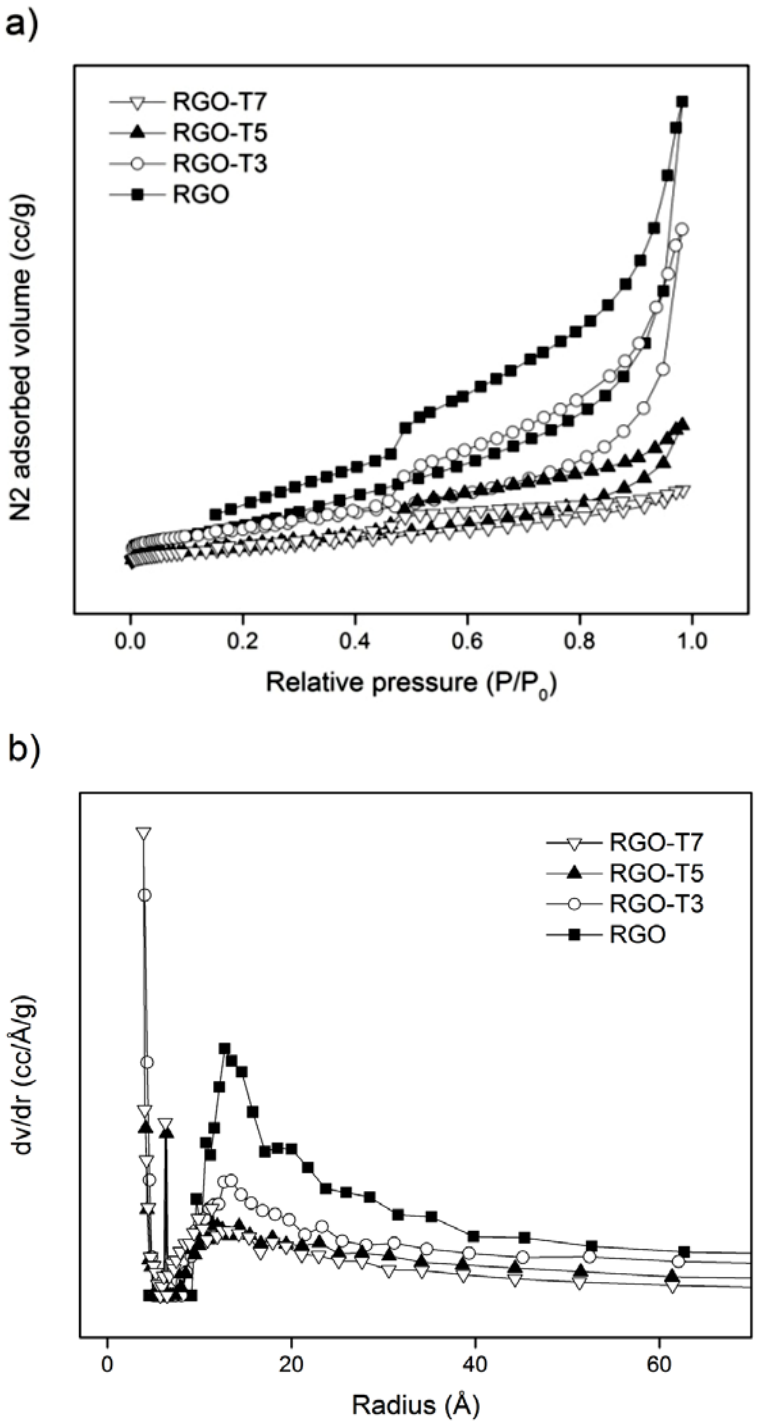

Figure 4.6 a) N_2 adsorption isotherms and b) pore size distribution of RGO and RGO-T nanocomposites

The Brunauer-Emmett-Teller (BET) and Barret-Joyner-Halenda (BJH) methods were applied to determine the specific surface area and pore structure, respectively. The pore-size distribution isotherm of RGO (Figure 4.6b) displayed one peak concentrated in 2–5nm.

After incorporation of nanoparticles, the main peak was weakened and an extra peak emerged at lower radius (~ 1 nm). Moreover, significant decrease in average pore size was detected after addition of Ti to the samples (Table 4.1). As a result, the reduction in specific surface area and average pore size can be attributed to the partial blockage of mesopores by TiO_2 nanoparticles [42].

Table 4.1 Specific surface area and pore diameter of RGO and RGO-T nanocomposites

	Specific surface area (m^2/g)	**Pore diameter (Å)**
RGO	461.76	25.5
RGO-T3	371.31	8.1
RGO-T5	219.35	8.3
RGO-T7	207.50	7.8

Figure 4.7 presents the hydrogen adsorption isotherms of RGO and RGO-T nanocomposites at 298 K. As expected, the hydrogen uptake of all samples increased by hydrogen pressure. The parent graphene sample shows hydrogen uptake of 0.17 wt. % at 10 bar. After TiO_2-integration, the hydrogen storage capacity of 0.39 wt. % was obtained by RGO-T5 that is 125% higher than that of pristine graphene. Further addition of Ti (RGO-T7) caused decrease of hydrogen adsorption, possibly owing to aggregation of nanoparticles and losing porosity/surface area.

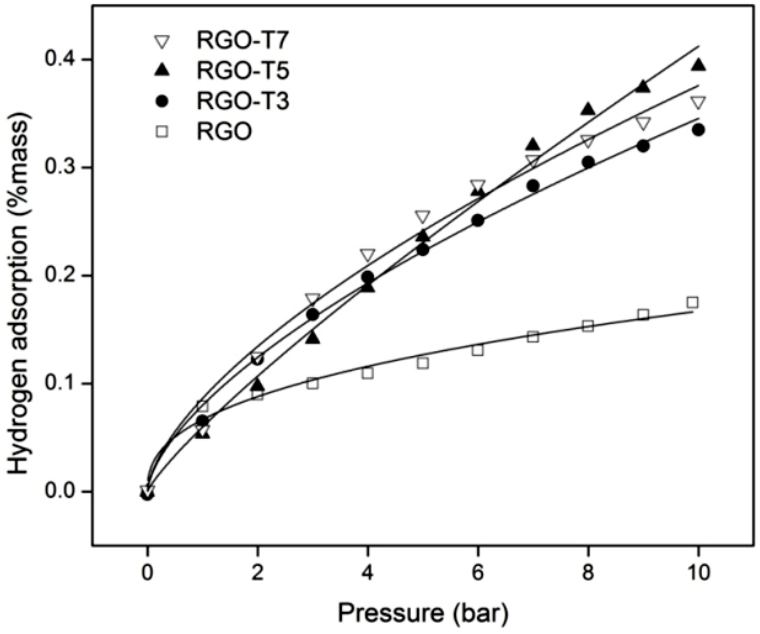

Figure 4.7 Hydrogen adsorption isotherms RGO and RGO nanocomposites

The enhanced hydrogen storage capacity of nanocomposites is not attributed to differences between the surface areas of samples since all nanocomposites displayed lower BET specific surface area than RGO (Figure 4.6a). In addition, comparison of hydrogen adsorption isotherms at 298 K reveals the change of the shape of the adsorption curves from concave in pristine graphene to relatively linear in RGO-T samples. Li et al. [43] found that linear adsorption isotherm is the characteristic behavior of hydrogen spillover on nearly all adsorbents and is very different from that of physical adsorptions characterized by an isotherm concave to the pressure axis. Thus, the higher hydrogen adsorption capacity of RGO-T nanocomposites originates from a process other than physical adsorption. Wang et al. [5, 44] have shown by the first-principle computations that strongly anchored Ti atoms on surface of GO template are superior sites for hydrogen adsorption whereby each Ti atom can bind multiple H_2 with the binding energies of 14–41 kJ/mol-H_2. Results of Hydrogen storage measurement obtained by Mishra et al. [45] Zhang et al. [8] and Lueking and Yang [46] suggest the contribution of chemical adsorptions in hydrogen uptake of different carbonaceous materials after incorporation of TiO_2. They showed that this contribution can be attributed to non-classical s–p–d hybridization [8]. As a result, higher hydrogen storage capacity of RGO-T nanocomposites compared to pristine graphene can be

linked to the activation of processes usually grouped as chemisorption. Lueking and Yang [46] have also underscored the role of catalyst-support interaction for improvement of hydrogen uptake of composites in which simple mixing of metal particles with support does not improve the hydrogen uptake of the system. Besides, Choucair and Mauron [47] reported decrease in hydrogen uptake of graphene at 77 K and 1 atm H_2 pressure after mechanical mixing with 1/1 weight ratio TiO_2 nanoparticles. Given the importance of particle size[27] and dispersion of nanoparticles [48] strong attachment of highly distributed nanoparticles to the underlying grapehene sheets was found to be essential to improve the hydrogen uptake of graphene/metal oxide nanocmposites.

4.3 Conclusions

A series of TiO_2-integrated reduced graphene oxide composites with different amounts of TiO_2 were prepared via a facile chemical impregnation method. Observed by TEM, TiO_2 nanoparticles with diameter of < 20 nm were homogeneously dispersed on the graphene sheets. It was shown that strong interaction of metal oxide nanoparticles with the support, smaller particle size, and high dispersion of nanoparticles are necessary to promote the hydrogen storage capacity of nanocomposites. The highest storage capacity of 0.39 wt. % was obtained among all nanocomposites that is 125 % higher than hydrogen uptake of parent graphene material. This significant improvement of hydrogen adsorption compared to decrease of hydrogen capacity of RGO-TiO_2 after mechanical mixing of components (reported by ref [47]) was correlated with the formation of Ti–O–C bonding between nanoparticles and graphene substrate.

4.4. References

[1] Z.G. Bajestani, A. Yurum, Y. Yurum, Significant improvement in the hydrogen storage capacity of a reduced graphene oxide/TiO2 nanocomposite by chemical bonding of Ti-O-C, RSC Advances, 6 (2016) 32831-32838.
[2] V. Tozzini, V. Pellegrini, Prospects for hydrogen storage in graphene, Physical Chemistry Chemical Physics, 15 (2013) 80-89.
[3] S. Gadipelli, Z.X. Guo, Graphene-based materials: Synthesis and gas sorption, storage and separation, Progress in Materials Science, 69 (2015) 1-60.
[4] Z.-S. Wu, G. Zhou, L.-C. Yin, W. Ren, F. Li, H.-M. Cheng, Graphene/metal oxide composite electrode materials for energy storage, Nano Energy, 1 (2012) 107-131.
[5] L. Wang, K. Lee, Y.-Y. Sun, M. Lucking, Z. Chen, J.J. Zhao, S.B. Zhang, Graphene Oxide as an Ideal Substrate for Hydrogen Storage, ACS Nano, 3 (2009) 2995-3000.

[6] E. Liu, Y. Gao, N. Zhao, J. Li, C. He, C. Shi, Adsorption of hydrogen atoms on graphene with TiO2 decoration, Journal of Applied Physics, 113 (2013) 153708.
[7] Y. Yu, N. Zhao, C. Shi, C. He, E. Liu, J. Li, Electrochemical hydrogen storage of expanded graphite decorated with TiO2 nanoparticles, International Journal of Hydrogen Energy, 37 (2012) 5762-5768.
[8] Z. Zhang, J.-Y. Hwang, M. Ning, X. Li, Field ionization effect on hydrogen adsorption over TiO2-coated activated carbon, International Journal of Hydrogen Energy, 37 (2012) 16018-16024.
[9] S.-u. Rather, N. Mehraj-ud-din, R. Zacharia, S.W. Hwang, A.R. Kim, K.S. Nahm, Hydrogen storage of nanostructured TiO2-impregnated carbon nanotubes, International Journal of Hydrogen Energy, 34 (2009) 961-966.
[10] C.-C. Huang, N.-W. Pu, C.-A. Wang, J.-C. Huang, Y. Sung, M.-D. Ger, Hydrogen storage in graphene decorated with Pd and Pt nano-particles using an electroless deposition technique, Separation and Purification Technology, 82 (2011) 210-215.
[11] M.S.A. Sher Shah, A.R. Park, K. Zhang, J.H. Park, P.J. Yoo, Green Synthesis of Biphasic TiO2–Reduced Graphene Oxide Nanocomposites with Highly Enhanced Photocatalytic Activity, ACS Applied Materials & Interfaces, 4 (2012) 3893-3901.
[12] S. Li, Z. Chen, Y. Jin, S. Chen, H. Wang, J. Geng, Q. Song, X. Yang, L. Ma, S. Li, Z. Qin, C. Zheng, A new approach for preparation of magnetite–graphite composite: Intercalation of polyhydroxy iron cation into graphite oxide in l-arginine medium, Solid State Sciences, 13 (2011) 862-866.
[13] Z.Q. Li, C.J. Lu, Z.P. Xia, Y. Zhou, Z. Luo, X-ray diffraction patterns of graphite and turbostratic carbon, Carbon, 45 (2007) 1686-1695.
[14] A. Dhanabalan, X. Li, R. Agrawal, C. Chen, C. Wang, Fabrication and Characterization of SnO2/Graphene Composites as High Capacity Anodes for Li-Ion Batteries, Nanomaterials, 3 (2013) 606.
[15] H.L. Poh, F. Sanek, A. Ambrosi, G. Zhao, Z. Sofer, M. Pumera, Graphenes prepared by Staudenmaier, Hofmann and Hummers methods with consequent thermal exfoliation exhibit very different electrochemical properties, Nanoscale, 4 (2012) 3515-3522.
[16] M. Giovanni, H.L. Poh, A. Ambrosi, G. Zhao, Z. Sofer, F. Sanek, B. Khezri, R.D. Webster, M. Pumera, Noble metal (Pd, Ru, Rh, Pt, Au, Ag) doped graphene hybrids for electrocatalysis, Nanoscale, 4 (2012) 5002-5008.
[17] X. Wang, X. Zhang, Electrochemical co-reduction synthesis of graphene/nano-gold composites and its application to electrochemical glucose biosensor, Electrochimica Acta, 112 (2013) 774-782.
[18] A. Ambrosi, A. Bonanni, Z. Sofer, J.S. Cross, M. Pumera, Electrochemistry at Chemically Modified Graphenes, Chemistry – A European Journal, 17 (2011) 10763-10770.
[19] G. Compagnini, P. Russo, F. Tomarchio, O. Puglisi, L. D'Urso, S. Scalese, Laser assisted green synthesis of free standing reduced graphene oxides at the water–air interface, Nanotechnology, 23 (2012) 505601.
[20] C. Chang-Jun, X. Mao-Wen, B. Shu-Juan, J. Chen-Chen, L. Zhen-Jiang, J. Dian-Zeng, A green and facile route for constructing flower-shaped TiO 2 nanocrystals assembled on graphene oxide sheets for enhanced photocatalytic activity, Nanotechnology, 24 (2013) 275602.
[21] H.C. Choi, Y.M. Jung, S.B. Kim, Size effects in the Raman spectra of TiO2 nanoparticles, Vibrational Spectroscopy, 37 (2005) 33-38.

[22] H. Yoshitake, D. Abe, Raman spectroscopic study of the framework structure of amorphous mesoporous titania, Microporous and Mesoporous Materials, 119 (2009) 267-275.
[23] K. Li, T. Chen, L. Yan, Y. Dai, Z. Huang, J. Xiong, D. Song, Y. Lv, Z. Zeng, Design of graphene and silica co-doped titania composites with ordered mesostructure and their simulated sunlight photocatalytic performance towards atrazine degradation, Colloids and Surfaces A: Physicochemical and Engineering Aspects, 422 (2013) 90-99.
[24] W.F. Zhang, Y.L. He, M.S. Zhang, Z. Yin, Q. Chen, Raman scattering study on anatase TiO 2 nanocrystals, Journal of Physics D: Applied Physics, 33 (2000) 912.
[25] H. Wang, J.T. Robinson, G. Diankov, H. Dai, Nanocrystal Growth on Graphene with Various Degrees of Oxidation, Journal of the American Chemical Society, 132 (2010) 3270-3271.
[26] C. Xu, X. Wang, Fabrication of Flexible Metal-Nanoparticle Films Using Graphene Oxide Sheets as Substrates, Small, 5 (2009) 2212-2217.
[27] C.-S. Tsao, Y.-R. Tzeng, M.-S. Yu, C.-Y. Wang, H.-H. Tseng, T.-Y. Chung, H.-C. Wu, T. Yamamoto, K. Kaneko, S.-H. Chen, Effect of Catalyst Size on Hydrogen Storage Capacity of Pt-Impregnated Active Carbon via Spillover, The Journal of Physical Chemistry Letters, 1 (2010) 1060-1063.
[28] I. Iatsunskyi, M. Kempiński, G. Nowaczyk, M. Jancelewicz, M. Pavlenko, K. Załęski, S. Jurga, Structural and XPS studies of PSi/TiO2 nanocomposites prepared by ALD and Ag-assisted chemical etching, Applied Surface Science, 347 (2015) 777-783.
[29] L. Yue-Wen, G. Meng-Xue, F. Lan, D. Shun-Liu, B. Jian-Feng, X. Su-Yuan, C. Zhong, H. Rong-Bin, Z. Lan-Sun, Facile and straightforward synthesis of superparamagnetic reduced graphene oxide–Fe 3 O 4 hybrid composite by a solvothermal reaction, Nanotechnology, 24 (2013) 025604.
[30] P. Wang, Y. Zhai, D. Wang, S. Dong, Synthesis of reduced graphene oxide-anatase TiO2 nanocomposite and its improved photo-induced charge transfer properties, Nanoscale, 3 (2011) 1640-1645.
[31] X. Bai, X. Zhang, Z. Hua, W. Ma, Z. Dai, X. Huang, H. Gu, Uniformly distributed anatase TiO2 nanoparticles on graphene: Synthesis, characterization, and photocatalytic application, Journal of Alloys and Compounds, 599 (2014) 10-18.
[32] S. Bourgeois, P. le Seigneur, M. Perdereau, Study by XPS of ultra-thin nickel deposits on TiO2(100) supports with different stoichiometries, Surface Science, 328 (1995) 105-110.
[33] W.S. Oh, C. Xu, D.Y. Kim, D.W. Goodman, Preparation and characterization of epitaxial titanium oxide films on Mo(100), Journal of Vacuum Science & Technology A, 15 (1997) 1710-1716.
[34] R. Rozada, J. Paredes, S. Villar-Rodil, A. Martínez-Alonso, J.D. Tascón, Towards full repair of defects in reduced graphene oxide films by two-step graphitization, Nano Res., 6 (2013) 216-233.
[35] S. Villar-Rodil, J.I. Paredes, A. Martinez-Alonso, J.M.D. Tascon, Preparation of graphene dispersions and graphene-polymer composites in organic media, Journal of Materials Chemistry, 19 (2009) 3591-3593.
[36] A. Felten, I. Suarez-Martinez, X. Ke, G. Van Tendeloo, J. Ghijsen, J.-J. Pireaux, W. Drube, C. Bittencourt, C.P. Ewels, The Role of Oxygen at the Interface between Titanium and Carbon Nanotubes, ChemPhysChem, 10 (2009) 1799-1804.

[37] M.C. Biesinger, L.W.M. Lau, A.R. Gerson, R.S.C. Smart, Resolving surface chemical states in XPS analysis of first row transition metals, oxides and hydroxides: Sc, Ti, V, Cu and Zn, Applied Surface Science, 257 (2010) 887-898.
[38] W.-S. Wang, D.-H. Wang, W.-G. Qu, L.-Q. Lu, A.-W. Xu, Large Ultrathin Anatase TiO2 Nanosheets with Exposed {001} Facets on Graphene for Enhanced Visible Light Photocatalytic Activity, The Journal of Physical Chemistry C, 116 (2012) 19893-19901.
[39] T.S. Sreeprasad, S.M. Maliyekkal, K.P. Lisha, T. Pradeep, Reduced graphene oxide–metal/metal oxide composites: Facile synthesis and application in water purification, Journal of Hazardous Materials, 186 (2011) 921-931.
[40] R.I. Masel, Principles of Adsorption and Reaction on Solid Surfaces, JOHN WILEY & SONS1996.
[41] C.-H. Chen, T.-Y. Chung, C.-C. Shen, M.-S. Yu, C.-S. Tsao, G.-N. Shi, C.-C. Huang, M.-D. Ger, W.-L. Lee, Hydrogen storage performance in palladium-doped graphene/carbon composites, International Journal of Hydrogen Energy, 38 (2013) 3681-3688.
[42] M.-S. Park, J.-S. Yu, K.J. Kim, G. Jeong, J.-H. Kim, Y.-N. Jo, U. Hwang, S. Kang, T. Woo, Y.-J. Kim, One-step synthesis of a sulfur-impregnated graphene cathode for lithium-sulfur batteries, Physical Chemistry Chemical Physics, 14 (2012) 6796-6804.
[43] Y. Li, F.H. Yang, R.T. Yang, Kinetics and Mechanistic Model for Hydrogen Spillover on Bridged Metal−Organic Frameworks, The Journal of Physical Chemistry C, 111 (2007) 3405-3411.
[44] L. Wang, J. Zhao, L. Wang, T. Yan, Y.-Y. Sun, S.B. Zhang, Titanium-decorated graphene oxide for carbon monoxide capture and separation, Physical Chemistry Chemical Physics, 13 (2011) 21126-21131.
[45] M. Amrita, B. Subarna, K.M. Susanta, A.G. Olivia, M. Mano, Synthesis of carbon nanotube–TiO 2 nanotubular material for reversible hydrogen storage, Nanotechnology, 19 (2008) 445607.
[46] A. Lueking, R.T. Yang, Hydrogen Spillover from a Metal Oxide Catalyst onto Carbon Nanotubes—Implications for Hydrogen Storage, Journal of Catalysis, 206 (2002) 165-168.
[47] M. Choucair, P. Mauron, Versatile preparation of graphene-based nanocomposites and their hydrogen adsorption, International Journal of Hydrogen Energy, 40 (2015) 6158-6164.
[48] L. Zubizarreta, J.A. Menéndez, J.J. Pis, A. Arenillas, Improving hydrogen storage in Ni-doped carbon nanospheres, International Journal of Hydrogen Energy, 34 (2009) 3070-3076.

Chapter 5 : Synthesis of anatase TiO_2 with exposed (001) facets grown on N-doped reduced graphene oxide for enhanced hydrogen storage

In this chapter we report the preparation and characterization of TiO_2-decorated N-doped graphene nanocomposite (hereafter referred to as TiO_2-N-RGO) via a solvothermal method [1]. Enhanced hydrogen capacity of this nanocomposite compared to graphene sample was linked to i) formation and stability of (001) reactive facets on nanoparticles and ii) strong attachment of fully dispersed and fine nanoparticles to the underlying substrate.

5.1 Introduction

The realization of innovative hydrogen storage materials has worldwide strategic importance. In the viewpoints of onboard storage applications, practical materials require efficient hydrogen adsorption at room temperature and pressures relevant for mobile systems. Among the various options for hydrogen storage technologies, much effort has been devoted to graphene-based systems due to their outstanding properties such as large specific surface area, chemical stability, and low mass density [2-9]. However, the weak binding between carbonaceous structures in any form and H_2 is an important parameter that leads to low H_2 adsorption of these materials [7]. Therefore, surface modifications such as functionalization by metal or metal oxide nanoparticles have been proposed to enhance gas adsorption property of graphene substrates [10]. In order to exploit all potentials of graphene decorated by nanoparticles, one has to cope with (i) the tendency of clustering and (ii) low catalytic activity of nanoparticles at ambient temperature.

To eliminate clustering of nanoparticles, one strategy is to introduce chemically active sites to graphene substrate [10-14]. Theoretical and experimental studies have shown that incorporation of substitutional atoms such as nitrogen and boron to carbonaceous structures gives rise to the formation of polarized bonding between carbon and substitutional atom and thus, improvement of the bonding between nanoparticles and the substrate occurs [10, 14, 15]. In the case of nitrogen, its higher electronegativity compared to carbon develops positive charge on carbon atoms. These positively charged centers pin nanoparticles to the surface of the support and derive the dispersion of nanoparticles [16, 17].

Apart from dispersion state, nature and particularly reactivity of nanoparticles are critical factors in hydrogen storage capacity of graphene-based nanocomposites. Titanium dioxide (TiO_2) has been widely studied due to its photochemical and catalytic characteristics. Theoretical studies have shown the potential of TiO_2-anchored carbonaceous materials as a promising hydrogen storage media for room-temperature applications [18, 19]. Recent experimental findings revealed a higher H_2 gas adsorption of carbon nanotube (CNT) and improved electrochemical hydrogen uptake of graphene after impregnation with TiO_2 nanoparticles [20, 21]. Since the reactivity of nanoparticles is directly related to their surface chemistry [22, 23], the stability of highly reactive crystalline planes rather than the stable ones in equilibrium state would further improve the hydrogen adsorption capacity of graphene-nanoparticle systems. In the case of TiO_2 (anatase), the (001) facets are the most reactive surfaces which are rapidly eliminated during the crystal growth to minimize the total surface free energy of the crystal [22, 24]. Therefore, utilization of chemical agents such as hydrofluoric acid (HF) that can bind to (001) facets would favor the occurrence of (001) rather than (101) planes in the synthesis of TiO_2 nanocrystals [24].

Here we report the preparation and characterization of TiO_2-decorated nitrogen-doped graphene nanocomposite via a solvothermal method (as explained in experimental chapter). The role of dispersion state of nanoparticles on hydrogen adsorption properties of the nanocomposite was examined through the cyclic stability and kinetic studies.

5.2 Results and discussion

5.2.1 Characterization of nanocomposites

Figure 5.1 shows thermogravimetric analysis of all samples indicating the presence of 11.3 wt. % and 11.26 wt. % TiO_2 particles in TiO_2-RGO and TiO_2-N-RGO nanocomposites, respectively.

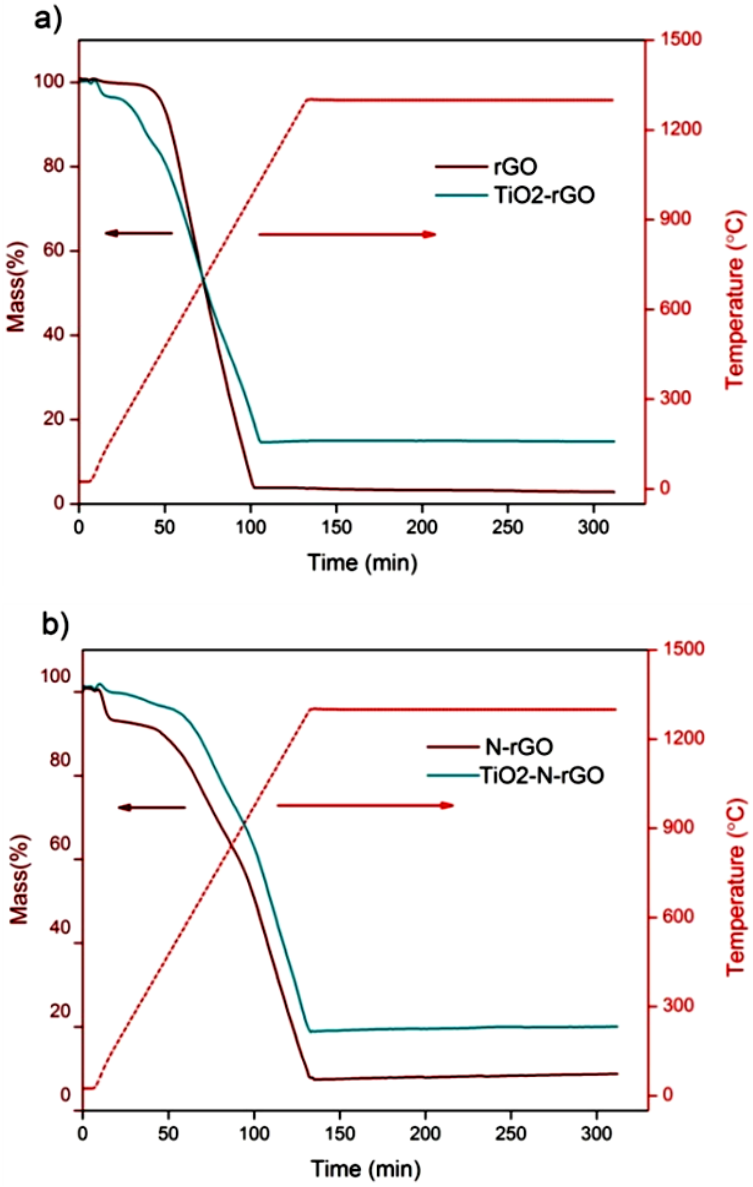

Figure 5.1 TGA of a) RGO and TiO_2-RGO and b) N-RGO and TiO_2-N-RGO nanocomposites as a function of time and temperature

Figure 5.2 displays nitrogen adsorption-desorption isotherms of synthesized specimens giving the specific surface area of 461, 95, 170, and 132 m^2/g respectively for reduced graphene oxide (RGO), nitrogen doped-RGO (N-RGO), TiO_2 doped RGO (TiO_2-RGO), and TiO_2-N-RGO.

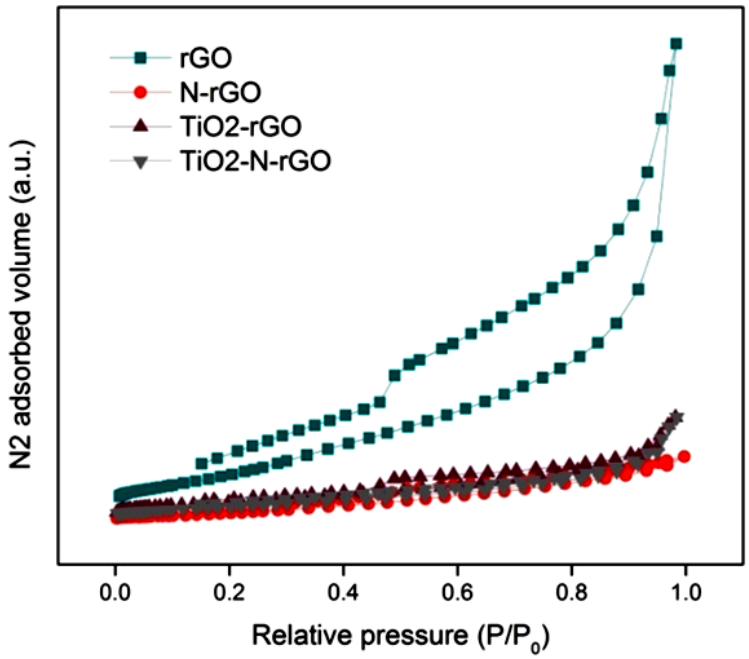

Figure 5.2 N_2 adsorption isotherms of RGO, N-RGO, TiO2-RGO and TiO_2-N-RGO nanocomposites

The XRD patterns of as-prepared samples are shown in Fig 5.3. In GO, the characteristic peak of (001) emerged at $2\theta \approx 10.5°$ that corresponds to d-spacing of 8.4 Å. This peak demonstrates the presence of oxygen-containing functional groups on graphene sheets [25]. After thermal reduction, a broad peak was observed in the range of 2θ = 18°–30° that is indexed as (002). The appearance of (002) peak in the absence of (001) peak in RGO and N-RGO implies the complete removal of oxygen functional groups from GO sheets and formation of poorly ordered graphene-like structure along the stacking direction [26]. Upon decoration of TiO_2 nanoparticles, a low intensity peak indexed as (004) appeared at 2θ = 37.9° and full width at half maximum (FWHM) of the (002) peak were changed. The latter observation suggests that the restacking of graphene nanosheets was prevented during the solvothermal process and TiO_2 nanoparticles act as a barrier to prevent agglomeration of graphene layers [27, 28]. It is noticeable that the main peak of TiO_2 at 25.3° and RGO at 24° are at the same region and thus, the characteristic peak of anatase TiO_2 may be screened by the main peak of RGO. The same observation has also been reported by Shah et al. [29] and Dhanabalan et al. [30] for TiO_2-RGO and SnO_2-Graphene composite, respectively.

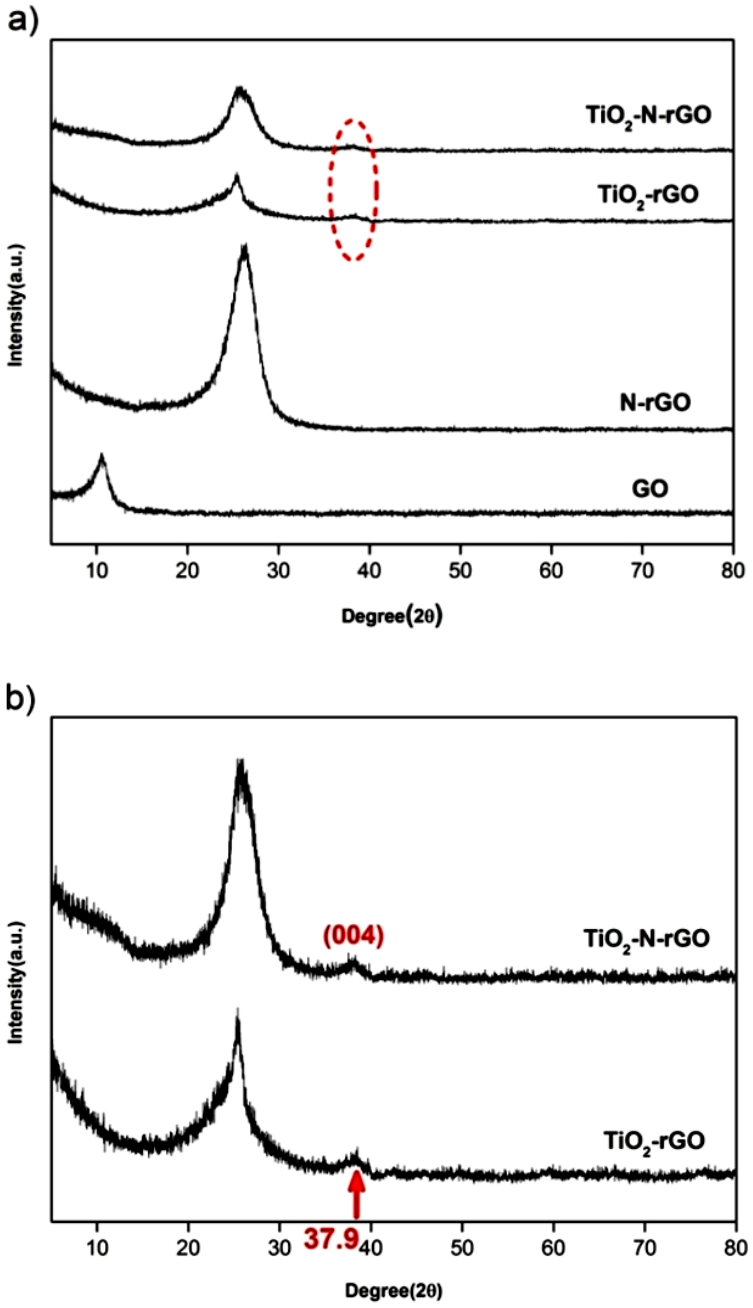

Figure 5.3 XRD patterns of a) GO, N-RGO, TiO_2-GO and TiO2-N-RGO and b) magnified XRD patterns of TiO_2-GO and TiO_2-N-RGO in higher magnification, the red dotted circle is the location of (004) planes of the anatase TiO_2

Formation of fine and distributed nanoparticles is highly preferred to improve the hydrogen uptake capacity of graphene-based materials [31]. To track the dispersion state of nanoparticles firstly, FE-SEM and EDS were performed on nanocomposites. As seen in Figure 5.4a, TiO_2-N-RGO displays almost complete coverage of uniformly distributed

nanoparticles on graphene layers with no sign of agglomeration. The corresponding elemental mapping analysis (Figure 5.4c–f) shows the well-defined spatial distribution of O, Ti, and N, validating the good dispersion of nanoparticles throughout the nanocomposite. On the other hand, agglomerated colonies are clearly observed (Figure 5.4b) when pristine graphene (without nitrogen doping, named as TiO_2-RGO nanocomposite) is utilized for the decoration of nanoparticles.

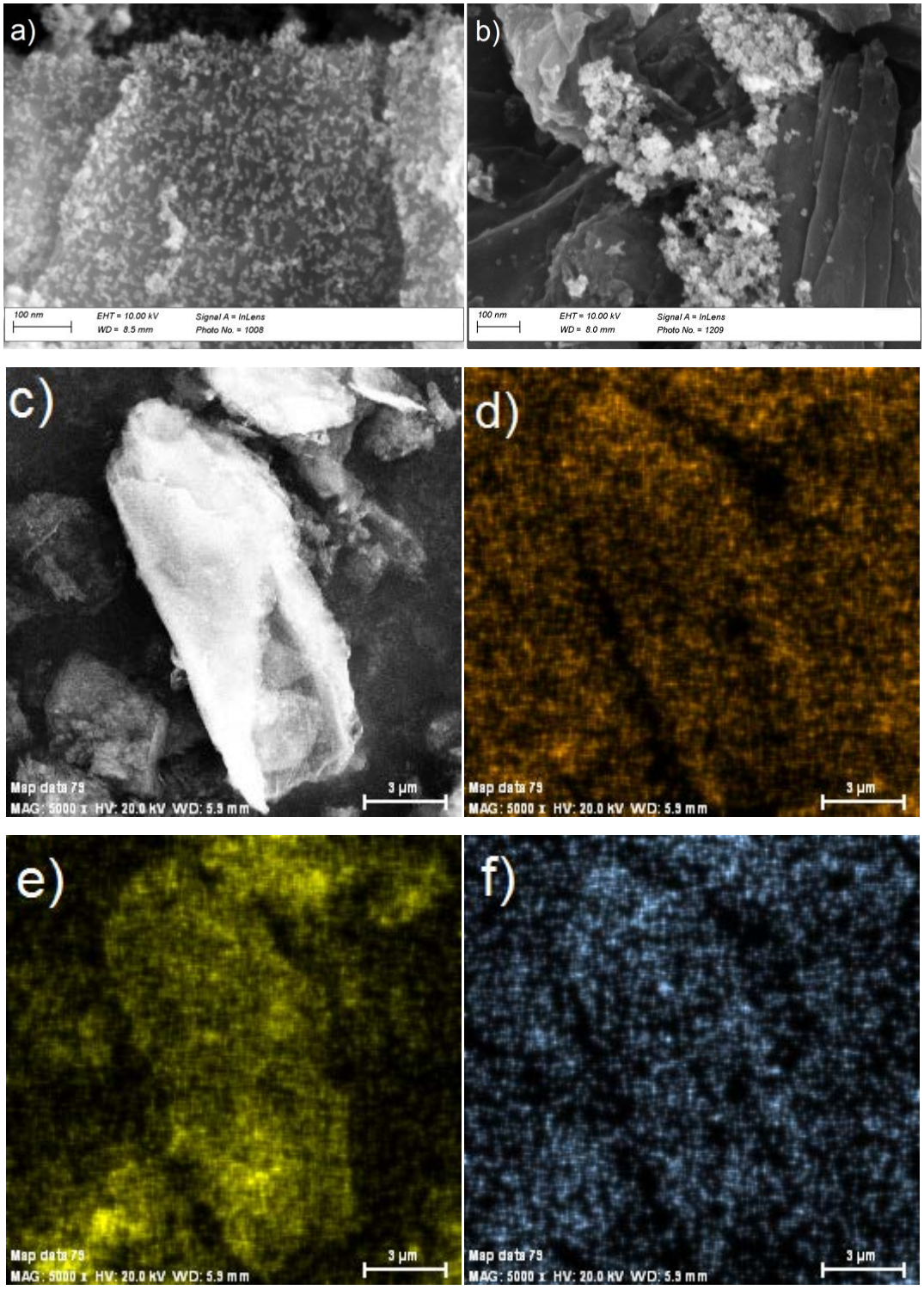

Figure 5.4 FE-SEM images of a) TiO_2-N-RGO, b) TiO_2-RGO, and c) selected area of TiO_2-N-RGO nanocomposite for elemental mapping analysis and corresponding elemental mapping for d) oxygen, e) titanium, and f) nitrogen

To elucidate the effect of nitrogen doping on distribution of nanoparticles, Raman spectroscopy was performed on reduced graphene oxide (RGO) and its nanocomposites (Figure 5.5a). The corresponding results of graphite and GO were also shown for comparison. Raman spectra of samples show two bands at Raman shifts of ~1350 cm^{-1} (D-band) and ~1580 cm^{-1} (G-band). G-band corresponds to vibration of the sp^2- bonded carbon atoms in a 2D hexagonal lattice and D-band represents the in-plane stretching motion of symmetric sp^2 C−C bonds. Higher intensity of the D-band (I_D) compared to G-band (I_G) generally indicates the formation of defective structure in graphene layers [32, 33]. The growth of I_D/I_G from 1.02 in RGO to 1.04 in N-RGO and 1.05 in TiO_2-N-RGO points out the increase of density of defects upon nitrogen doping and presence of graphene-nanoparticles interaction, respectively [28, 32]. It is worth mentioning that all nanocomposites exhibit characteristic Raman peaks at 151 cm^{-1}, 390 cm^{-1}, 515 cm^{-1} and 629 cm^{-1} (Figure 5.5b) that are attributed to E_g, $B_{1g}(1)$, A_{1g} + $B_{1g}(2)$, and $E_g(2)$ modes of TiO_2, respectively [34-36]. In agreement with results of XRD (Figure 4.3), this observation confirms the formation of TiO_2 anatase phase throughout nanocomposites.

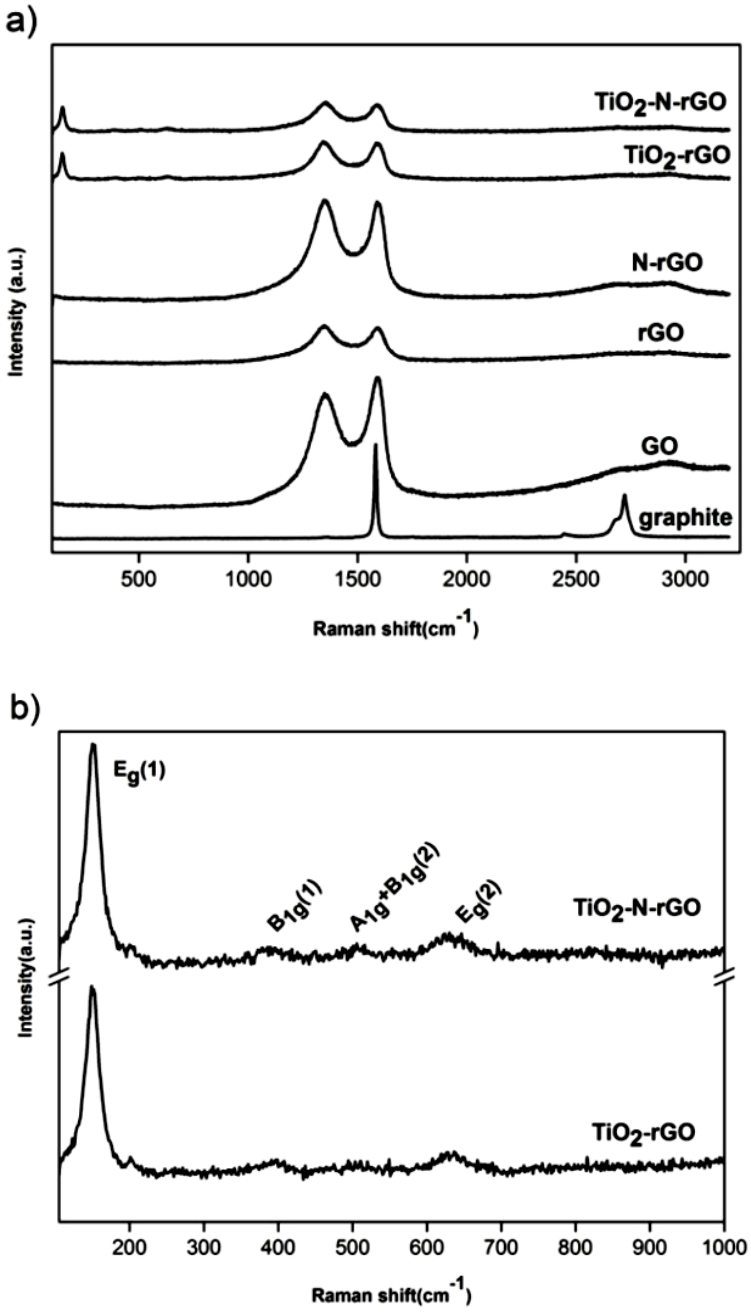

Figure 5.5 Raman characterization of a) graphite, GO, RGO, N-RGO, TiO_2-RGO, and TiO_2-N-RGO and b) TiO_2-RGO and TiO_2-N-RGO in the range 100−9000 cm^{-1}

X-ray photoelectron spectroscopy (XPS) was performed to determine the elemental quantification in TiO_2-N-RGO nanocomposite. Figure 5.6a shows the core level XPS spectrum of C 1s orbital. The peaks centered at 284.43 eV and 291.94 eV are assigned to graphite-like sp^2 C and satellite peak of π-π^* interaction, respectively. This indicates that most of the C atoms are arranged in a conjugated honeycomb lattice. Carbon atoms bonded

to nitrogen-substituted sites depict two peaks at the bonding energies of 285.98, 287.38 eV that show the formation of N–sp^2 C, N–sp^3 C in graphene structure, respectively [37-39]. Various types of nitrogen functional groups like graphitic N, pyridinic-N, and pyrrolic-N can be present in nitrogen-doped carbon system [10, 32]. The pyridinic groups refer to the N atoms at the side of graphene layers that make two chemical bonds with C atoms and donate one π-electron to the carbon network. The pyrrolic-N atoms make bonds with two C atoms and contribute to the π system with two π-electrons [17, 32, 37]. XPS spectrum of N 1s orbital shown in Figure 5.6b confirms the formation of these three functional groups; pyridinic-N (397.9eV, 0.9 atom%), pyrrolic-N (399.04 eV, 2.12 atom%), and graphitic N (401.14eV, 1.44 atom%) [10, 32]. These groups are schematically demonstrated in Figure 5.6c. Since the development of a high number of polarized sites on graphene sheets (Figure 5.4f) coincides with the high distribution of nanoparticles (Figure 5.4a), it can be concluded that nitrogen-containing functional groups act as nucleation centers for the growth of nanoparticles. This observation is in agreement with previous reports illustrating that doping heteroatoms promote dispersion of nanoparticles in carbonaceous materials [10, 40].

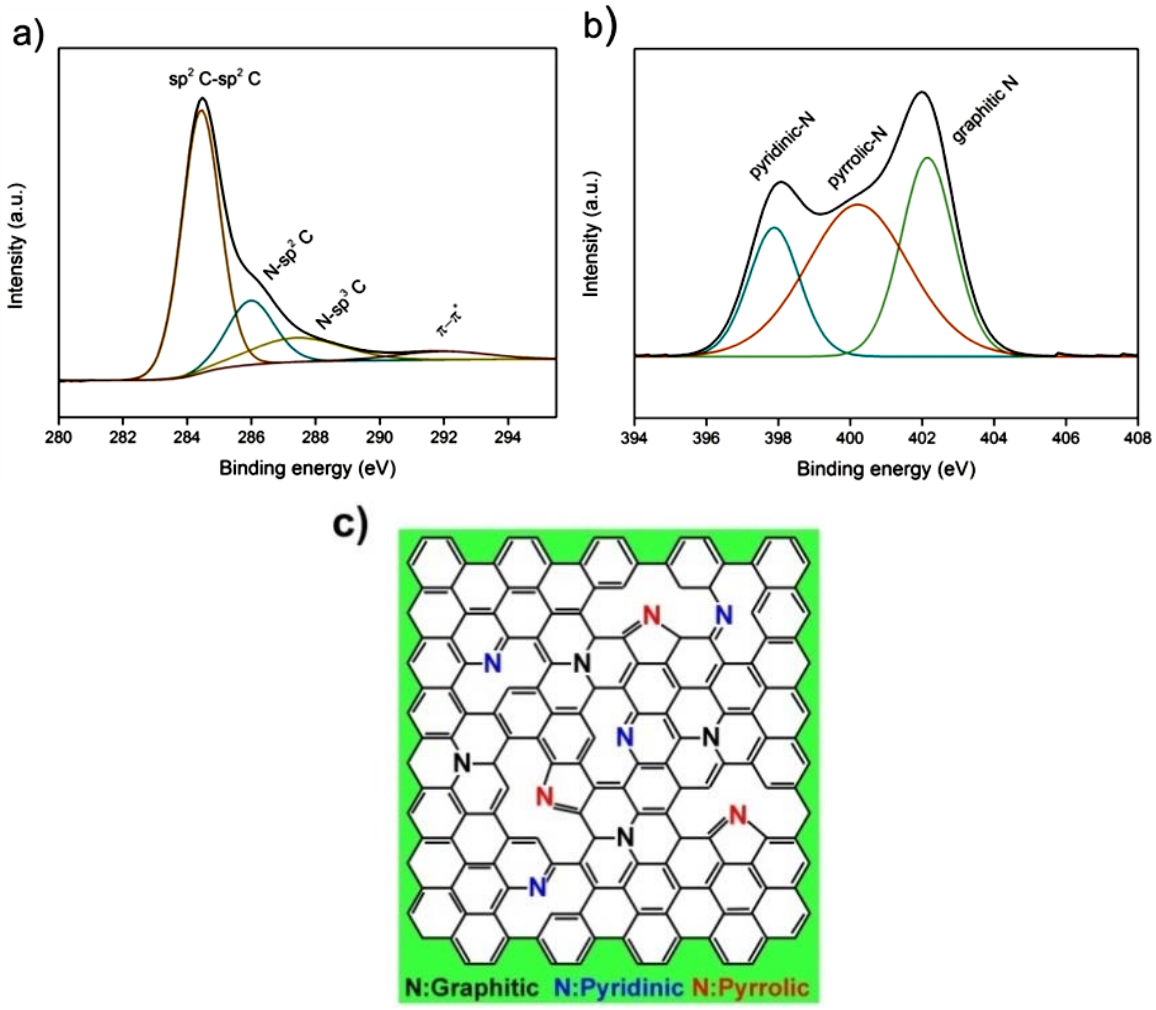

Figure 5.6 High-resolution XPS results of a) carbon and b) nitrogen, and c) schematic showing the bond structure of nitrogen-doped graphene

When core level XPS spectrum of Ti is considered (Figure 5.7a), two peaks are observed at 464.8 eV (Ti $2p_{1/2}$) and 459.1 eV (Ti $2p_{3/2}$). The splitting energy of 5.7 eV shows the normal state of Ti^{4+} in TiO_2 nanoparticles [27, 29]. The presence of oxygen is also detected at 532 and 530 eV (Figure 5.7b) that are attributed to the adsorbed oxygen on the surface of TiO_2 [41] and oxygen bonding energy in Ti−O−C structure, respectively [42]. The latter observation confirms the attachment of TiO_2 particles to the graphene substrate. In order to understand the interaction between Ti and F, XPS spectrum of F 1s is presented in Figure 5.7c. The measured bonding energy of 684.7 eV originates from ligand exchange between F^- and surface hydroxyl groups. Since, no peak was observed at 688.5 eV—F in a solid solution of $TiO_{2-x}F_x$ [41], it can be concluded that diffusion of F species

into the lattice of TiO_2 and subsequently lattice substitution of F^- for O^{-2} is ruled out [22, 41, 43].

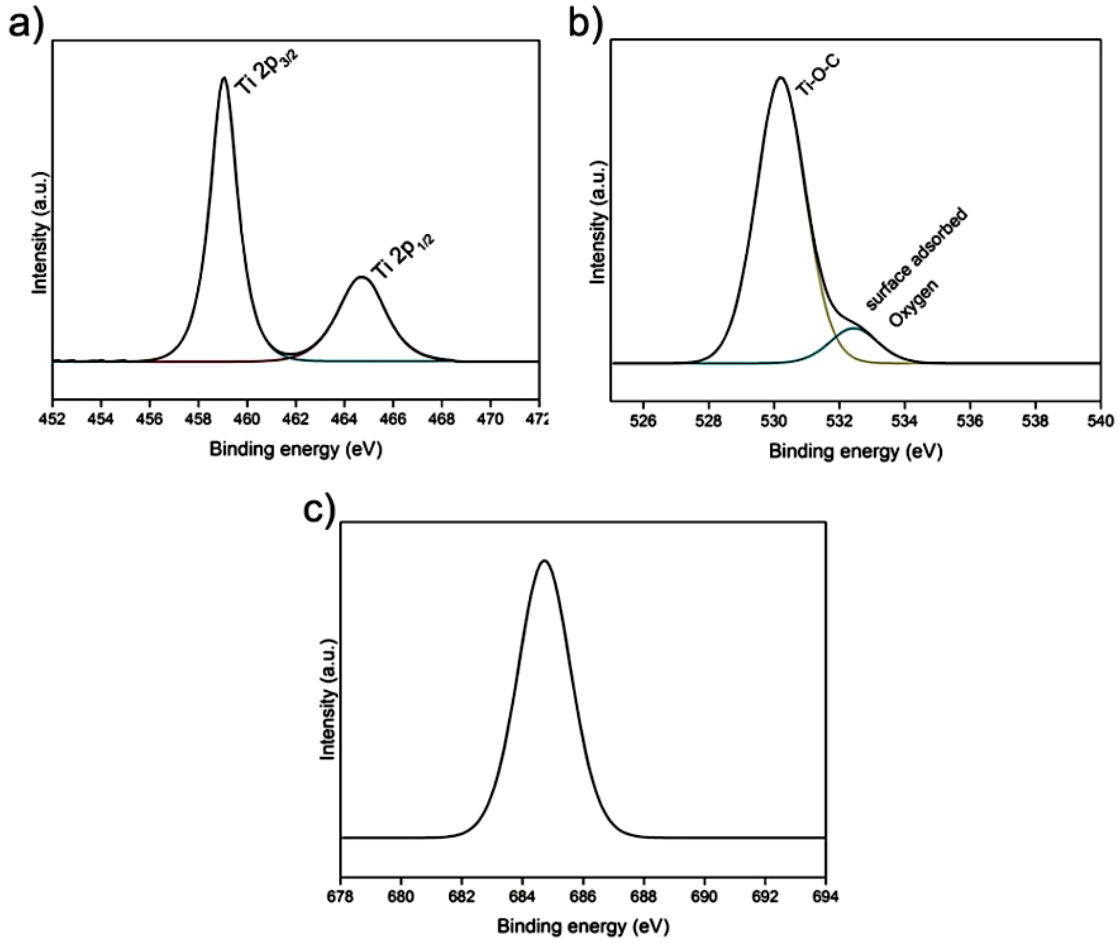

Figure 5.7 High-resolution X-ray photoelectron spectra of a) titanium, b) oxygen, and c) fluorine in TiO_2-N-RGO nanocomposite

HR-TEM was used to characterize the morphology and crystal structure of TiO_2 nanoparticles. As shown in Figure 5.8a, square-shaped nanoparticles are clearly detectable with their well-defined edges and corners. Figure 5.8b and 5.8c display the lattice fringes with a spacing of 0.355 and 0.231–0.235 nm that correspond to the d-spacing of the (101) and (004) planes of TiO_2 anatase phase, respectively. The observed (004) planes are parallel to the surface of the particles and present a direct evidence for the existence of (001) exposed facets. The d-spacing of (004) planes is also in well agreement with the results of XRD ($2\theta = 37.9°$ with d-spacing of 0.235 nm, Figure 5.3b) and previous reports [44, 45]. Inset of Figure 4.8c schematically illustrates the truncated octahedral structure of

TiO_2 nanoparticles. The top and bottom surfaces represent (001) facets which are shown in Figure 5.8b and 5.8c.

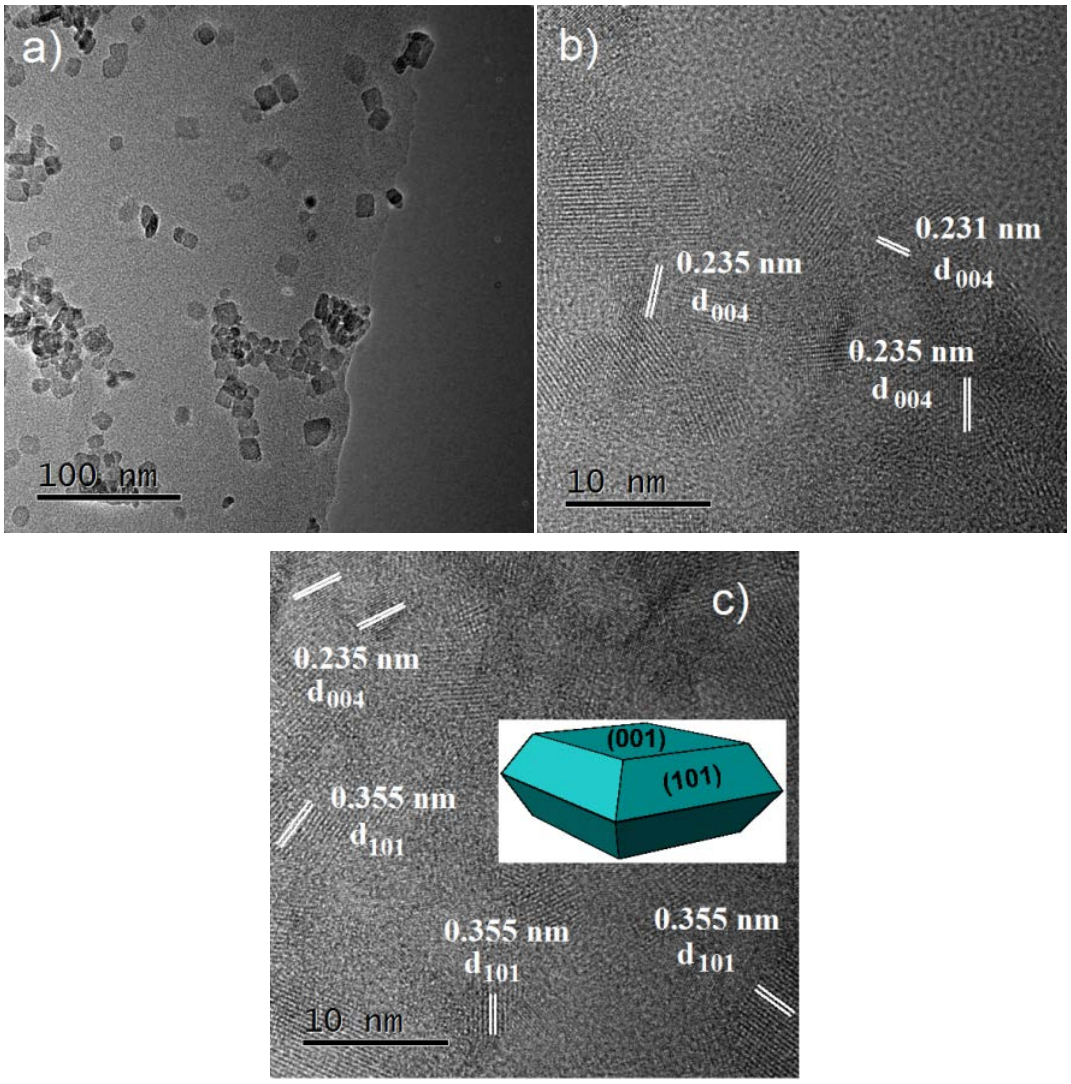

Figure 5.8 a) Low-magnification TEM, and b) and c) HR-TEM images of TiO_2-RGO (Inset shows a 3D model of the truncated TiO_2 nanoparticles.)

5.2.2 Hydrogen adsorption

Figure 5.9a shows the hydrogen adsorption isotherm of nanocomposites measured in the pressure range of 0–8 bar at room temperature. The hydrogen uptake of the specimens increased with hydrogen pressure. While RGO has the lowest hydrogen uptake among all specimens (~ 0.15 wt. %), incorporation of TiO_2 nanoparticles to N-doped RGO significantly increased hydrogen capacity of the system to 0.91 wt. % that is ~ 500%, ~

400%, and ~ 130% higher than the hydrogen uptake values of RGO, N-RGO, and TiO_2-RGO, respectively.

The interaction between gas molecules (here H_2) and carbonaceous materials is based on the Van der Waals interactions. Therefore, tailoring the charge distribution of the substrate can improve the strength of C–H bond [10]. When carbon atoms are substituted by heteroatoms (e.g., N, S), the p orbital of the substitute atom and the 1s orbital from the hydrogen atom contribute to form a bond that results in the elongation of H–H bond in hydrogen molecules. This elongation indicates the activation of H_2 and leads to migration of hydrogen molecules to a carbon site [46]. In our system, presence of nitrogen atoms (Figure 5.4f and 5.6b), especially pyrrolic N that donates two electrons to honeycomb lattice of carbon changes the asymmetry of electron charge cloud of the substrate lattice and thus, enhances the polarity of the system. This enhanced polarity increases the strength of C–H bond and gives rise to higher hydrogen capacity of N-RGO than that of RGO. However, high hydrogen uptake of TiO_2-N-RGO nanocomposite cannot be solely explained by hydrogen uptake of N-doped graphene and TiO_2 nanoparticles. Theoretical studies on TiO_2-decorated graphene have shown that strongly anchored Ti atoms on the surface of the template are superior sites for hydrogen adsorption whereby each Ti atom can bind multiple H_2 with the binding energies of 14–41 kJ/mol-H_2 [18]. We demonstrated that strong attachment of TiO_2 nanoparticles (without exposed facets) to the underlying graphene substrate through Ti–O–C bond is crucial to enhance the hydrogen storage of the nanocomposite. In our previous study, we reported an uptake of 0.32 ± 0.03 wt. % for RGO-TiO_2 nanocomposites [47] whereas a mechanical mixture of graphene and TiO_2 nanoparticles (1/1 wt/wt) showed lower hydrogen uptake compared to that of parent graphene [48]. Therefore, the significant enhancement of hydrogen uptake of TiO_2-N-RGO nanocomposite compared to that of RGO was attributed to the formation of; i) highly reactive (001) exposed facets on TiO_2, ii) evenly distributed TiO_2 nanoparticles on the graphene sheets, and iii) the strong interaction of substrate and nanoparticles through Ti–O–C bonding.

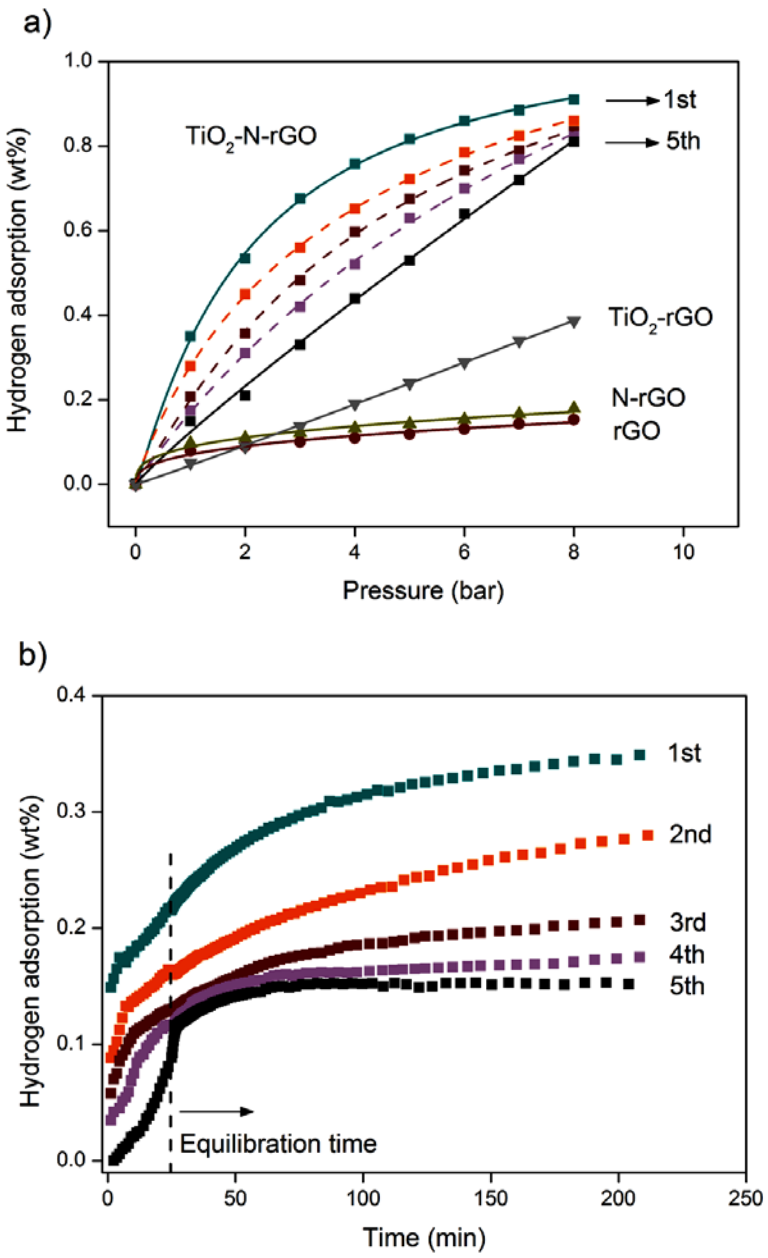

Figure 5.9 a) Hydrogen adsorption isotherms of RGO, N-RGO, TiO_2-RGO, and cyclic performance of TiO_2-N-RGO and b) kinetic curves of hydrogenation at 1 bar (first isotherm point) for TiO_2-N-RGO

The cyclic performance of TiO_2-N-RGO nanocomposite was studied through 5 cycles and the adsorption isotherms are shown in Figure 5.9a. Hydrogenation was performed at room temperature with 12 h degassing stage under vacuum of 10^{-7} mbar before the pressurizing step. Later equilibration time was set to 180 min for isothermal points of each cycle.

Hydrogen re-loading with constant equilibration time led to a notable reduction in H_2 uptakes of the nanocomposite at the first isothermal point (1 bar). However, at the last isotherm point (8 bar) the hydrogen capacities display a minimal reduction; changing from 0.91 wt. % in the first cycle to 0.81 at 5^{th} cycle. After degassing stage, 88% of the stored hydrogen was released at ambient conditions and a residual mass of ~ 0.1 wt. % retained at very low pressures. This retaining hydrogen can be attributed to the interaction of hydrogen with defects such as holes and edges that leads to reduction of available sites for hydrogen adsorption [49]. The relevant kinetic curves of adsorption isotherm at 1 bar are shown in Figure 4.9b. It is interesting to note that no induction period is required to initiate the process of adsorption as high hydrogen uptake is detected even before reaching the equilibration period (dashed line in Figure 5.9b). Altogether, these observations imply that almost all the binding sites do not degenerate upon cyclic hydrogenation [50].

To provide further insight about the effect of reactive (001) facets on the cyclic stability of nanocomposite, the morphology, size, and distribution of TiO_2 nanoparticles were investigated after 3^{rd} cyclic H_2-loading. As shown in Figure 5.10a, homogeneous dispersion of nanoparticles is clearly detectable on the graphene sheets. Visual observation in Figure 5.10b reveals the rectangular shaped crystallites within a size range of 5.5–6.5 nm which is highly beneficial for the H_2 gas adsorption [51]. This rectangular morphology was originally observed in nanocomposite before hydrogen storage measurement and found to be stable after cyclic hydrogen uptakes. Lattice fringes (magnified in Figure 5.10c) confirmed the stability of (001) exposed nanofacets after cyclic gas adsorption.

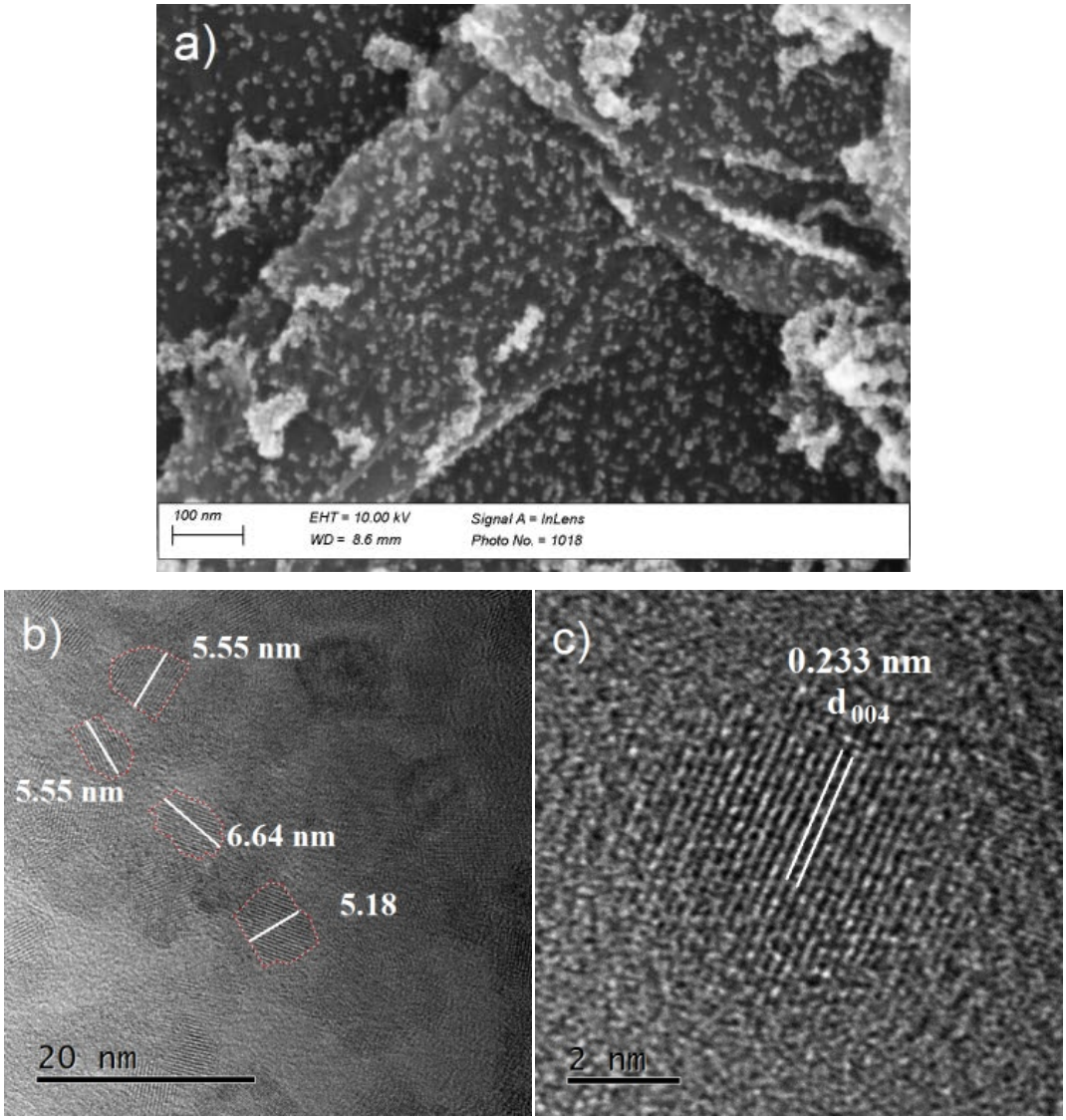

Figure 5.10 FE-SEM a) and HR-TEM b) and c) images of TiO2-N-RGO sample after 3rd cycle of hydrogen adsorption

The corresponding elemental mapping shown in Figure 5.11a–d further validates the uniform distribution of TiO_2 nanoparticles throughout the nanocomposite. These observations demonstrate that cyclic stability of TiO_2-N-RGO nanocomposite can be mainly ascribed to the high stability of reactive (001) exposed facets and dispersed TiO_2 nanoparticles in the hydrogen storage system.

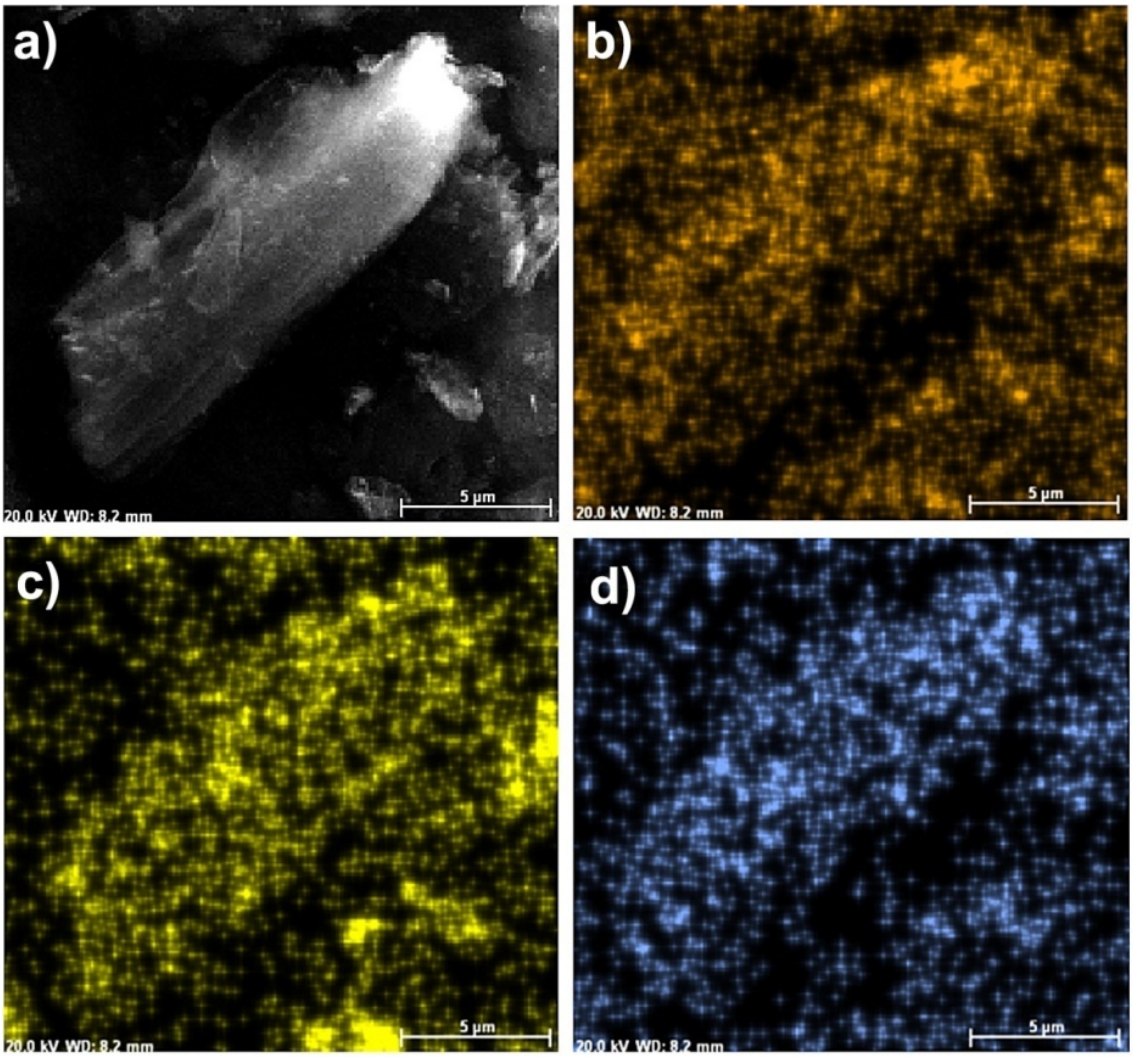

Figure 5.11 Elemental mapping analysis of TiO_2-N-RGO nanocomposite sample after 3rd cycle of hydrogen adsorption: a) selected area, b) oxygen, c) titanium, and d) nitrogen

5.3 Conclusions

TiO_2 (anatase) with exposed (001) facets were decorated on nitrogen-doped graphene by a solvothermal method. Nitrogen doping was found to be an effective method to obtain an excellent dispersion of nanoparticles. Highly dispersed nanoparticles with strong interaction with the support are crucial to promote the hydrogen storage capacity of the system. Incorporation of TiO_2 nanoparticles with exposed (001) facets to graphene sheets significantly enhanced the hydrogen uptake of the systems at room temperature and low hydrogen pressures (0.8 MPa). Simultaneous utilization of nitrogen doped graphene and reactive TiO_2 nanoparticles were also found to be an effective method to enhance the cyclic

stability of nanocomposite. These results provide an efficient and convenient way to design high-performance graphene-based nanocomposites for hydrogen storage systems that can also be used for applications that necessitate high reactivity and stability.

5.4 References

[1] Z. Gohari-Bajestani, O. Akhlaghi, Y. Yürüm, A. Yürüm, Synthesis of anatase TiO2 with exposed (001) facets grown on N-doped reduced graphene oxide for enhanced hydrogen storage, International Journal of Hydrogen Energy, 42 (2017) 6096-6103.
[2] C.-H. Chen, T.-Y. Chung, C.-C. Shen, M.-S. Yu, C.-S. Tsao, G.-N. Shi, C.-C. Huang, M.-D. Ger, W.-L. Lee, Hydrogen storage performance in palladium-doped graphene/carbon composites, Int. J. Hydrogen Energy, 38 (2013) 3681-3688.
[3] L. Ma, J.-M. Zhang, K.-W. Xu, Hydrogen storage on nitrogen induced defects in palladium-decorated graphene: A first-principles study, Appl. Surf. Sci., 292 (2014) 921-927.
[4] G. Srinivas, Y. Zhu, R. Piner, N. Skipper, M. Ellerby, R. Ruoff, Synthesis of graphene-like nanosheets and their hydrogen adsorption capacity, Carbon, 48 (2010) 630-635.
[5] K. Spyrou, D. Gournis, P. Rudolf, Hydrogen Storage in Graphene-Based Materials: Efforts Towards Enhanced Hydrogen Absorption, ECS J. Solid State Sci. Technol., 2 (2013) M3160-M3169.
[6] C. Ataca, E. Aktürk, S. Ciraci, H. Ustunel, High-capacity hydrogen storage by metallized graphene, Appl. Phys. Lett., 93 (2008) 043123.
[7] S. Gadipelli, Z.X. Guo, Graphene-based materials: Synthesis and gas sorption, storage and separation, Prog. Mater. Sci., 69 (2015) 1-60.
[8] N. Kostoglou, A. Tarat, I. Walters, V. Ryzhkov, C. Tampaxis, G. Charalambopoulou, T. Steriotis, C. Mitterer, C. Rebholz, Few-layer graphene-like flakes derived by plasma treatment: A potential material for hydrogen adsorption and storage, Micropor. Mesopor. Mat., 225 (2016) 482-487.
[9] D.P. Broom, M. Hirscher, Irreproducibility in hydrogen storage material research, Energy & Environmental Science, (2016).
[10] V.B. Parambhath, R. Nagar, S. Ramaprabhu, Effect of Nitrogen Doping on Hydrogen Storage Capacity of Palladium Decorated Graphene, Langmuir, 28 (2012) 7826-7833.
[11] L. Ma, J.-M. Zhang, K.-W. Xu, V. Ji, Hydrogen adsorption and storage on palladium-decorated graphene with boron dopants and vacancy defects: A first-principles study, Physica E Low Dimens. Syst. Nanostruct., 66 (2015) 40-47.
[12] S. Seenithurai, R.K. Pandyan, S.V. Kumar, C. Saranya, M. Mahendran, Li-decorated double vacancy graphene for hydrogen storage application: A first principles study, Int. J. Hydrogen Energy, 39 (2014) 11016-11026.
[13] D. Kim, S. Lee, Y. Hwang, K.-H. Yun, Y.-C. Chung, Hydrogen storage in Li dispersed graphene with Stone–Wales defects: A first-principles study, Int. J. Hydrogen Energy, 39 (2014) 13189-13194.
[14] E. Beheshti, A. Nojeh, P. Servati, A first-principles study of calcium-decorated, boron-doped graphene for high capacity hydrogen storage, Carbon, 49 (2011) 1561-1567.
[15] S. Nachimuthu, P.-J. Lai, J.-C. Jiang, Efficient hydrogen storage in boron doped graphene decorated by transition metals – A first-principles study, Carbon, 73 (2014) 132-140.

[16] M. Chen, J. Liu, W. Zhou, J. Lin, Z. Shen, Nitrogen-doped Graphene-Supported Transition-metals Carbide Electrocatalysts for Oxygen Reduction Reaction, Sci. Rep., 5 (2015) 10389.
[17] G. Wu, A. Santandreu, W. Kellogg, S. Gupta, O. Ogoke, H. Zhang, H.-L. Wang, L. Dai, Carbon nanocomposite catalysts for oxygen reduction and evolution reactions: From nitrogen doping to transition-metal addition, Nano Energy.
[18] L. Wang, K. Lee, Y.-Y. Sun, M. Lucking, Z. Chen, J.J. Zhao, S.B. Zhang, Graphene Oxide as an Ideal Substrate for Hydrogen Storage, ACS Nano, 3 (2009) 2995-3000.
[19] E. Liu, Y. Gao, N. Zhao, J. Li, C. He, C. Shi, Adsorption of hydrogen atoms on graphene with TiO2 decoration, Journal of Applied Physics, 113 (2013) 153708.
[20] Y. Yu, N. Zhao, C. Shi, C. He, E. Liu, J. Li, Electrochemical hydrogen storage of expanded graphite decorated with TiO2 nanoparticles, International Journal of Hydrogen Energy, 37 (2012) 5762-5768.
[21] S.-u. Rather, N. Mehraj-ud-din, R. Zacharia, S.W. Hwang, A.R. Kim, K.S. Nahm, Hydrogen storage of nanostructured TiO2-impregnated carbon nanotubes, International Journal of Hydrogen Energy, 34 (2009) 961-966.
[22] H.G. Yang, C.H. Sun, S.Z. Qiao, J. Zou, G. Liu, S.C. Smith, H.M. Cheng, G.Q. Lu, Anatase TiO2 single crystals with a large percentage of reactive facets, Nature, 453 (2008) 638-641.
[23] A. Selloni, Crystal growth: Anatase shows its reactive side, Nat. Mater., 7 (2008) 613-615.
[24] L. Wu, B.X. Yang, X.H. Yang, Z.G. Chen, Z. Li, H.J. Zhao, X.Q. Gong, H.G. Yang, On the synergistic effect of hydrohalic acids in the shape-controlled synthesis of anatase TiO2 single crystals, Cryst. Eng. Comm., 15 (2013) 3252-3255.
[25] H.L. Poh, F. Sanek, A. Ambrosi, G. Zhao, Z. Sofer, M. Pumera, Graphenes prepared by Staudenmaier, Hofmann and Hummers methods with consequent thermal exfoliation exhibit very different electrochemical properties, Nanoscale, 4 (2012) 3515-3522.
[26] C. Xiang, M. Li, M. Zhi, A. Manivannan, N. Wu, Reduced graphene oxide/titanium dioxide composites for supercapacitor electrodes: shape and coupling effects, J. Mater. Chem., 22 (2012) 19161-19167.
[27] X. Bai, X. Zhang, Z. Hua, W. Ma, Z. Dai, X. Huang, H. Gu, Uniformly distributed anatase TiO2 nanoparticles on graphene: Synthesis, characterization, and photocatalytic application, J. Alloy Compd., 599 (2014) 10-18.
[28] P. Shao, J. Tian, W. Shi, S. Gao, F. Cui, Eco-friendly one-pot synthesis of ultradispersed TiO2 nanocrystals/graphene nanocomposites with high photocatalytic activity for dye degradation, J. Mater. Chem. A, 3 (2015) 19913-19919.
[29] M.S.A. Sher Shah, A.R. Park, K. Zhang, J.H. Park, P.J. Yoo, Green Synthesis of Biphasic TiO2–Reduced Graphene Oxide Nanocomposites with Highly Enhanced Photocatalytic Activity, ACS Appl. Mater. Interfaces, 4 (2012) 3893-3901.
[30] A. Dhanabalan, X. Li, R. Agrawal, C. Chen, C. Wang, Fabrication and Characterization of SnO2/Graphene Composites as High Capacity Anodes for Li-Ion Batteries, Nanomaterials, 3 (2013) 606.
[31] C.-S. Tsao, Y.-R. Tzeng, M.-S. Yu, C.-Y. Wang, H.-H. Tseng, T.-Y. Chung, H.-C. Wu, T. Yamamoto, K. Kaneko, S.-H. Chen, Effect of Catalyst Size on Hydrogen Storage Capacity of Pt-Impregnated Active Carbon via Spillover, J. Phys. Chem. Lett., 1 (2010) 1060-1063.

[32] Y. Shao, S. Zhang, M.H. Engelhard, G. Li, G. Shao, Y. Wang, J. Liu, I.A. Aksay, Y. Lin, Nitrogen-doped graphene and its electrochemical applications, J. Mater. Chem., 20 (2010) 7491-7496.
[33] P. Cheng, Z. Yang, H. Wang, W. Cheng, M. Chen, W. Shangguan, G. Ding, TiO2–graphene nanocomposites for photocatalytic hydrogen production from splitting water, Int. J. Hydrogen Energy, 37 (2012) 2224-2230.
[34] C. Chang-Jun, X. Mao-Wen, B. Shu-Juan, J. Chen-Chen, L. Zhen-Jiang, J. Dian-Zeng, A green and facile route for constructing flower-shaped TiO 2 nanocrystals assembled on graphene oxide sheets for enhanced photocatalytic activity, Nanotechnology, 24 (2013) 275602.
[35] H.C. Choi, Y.M. Jung, S.B. Kim, Size effects in the Raman spectra of TiO2 nanoparticles, Vib. Spectrosc., 37 (2005) 33-38.
[36] X. Zhang, Y. Sun, X. Cui, Z. Jiang, A green and facile synthesis of TiO2/graphene nanocomposites and their photocatalytic activity for hydrogen evolution, Int. J. Hydrogen Energy, 37 (2012) 811-815.
[37] D. Wei, Y. Liu, Y. Wang, H. Zhang, L. Huang, G. Yu, Synthesis of N-Doped Graphene by Chemical Vapor Deposition and Its Electrical Properties, Nano Lett., 9 (2009) 1752-1758.
[38] H. Wang, C. Zhang, Z. Liu, L. Wang, P. Han, H. Xu, K. Zhang, S. Dong, J. Yao, G. Cui, Nitrogen-doped graphene nanosheets with excellent lithium storage properties, J. Mater. Chem., 21 (2011) 5430-5434.
[39] K. Dave, K.H. Park, M. Dhayal, Characteristics of ultrasonication assisted assembly of gold nanoparticles in hydrazine reduced graphene oxide, RSC Adv., 5 (2015) 107348-107354.
[40] H. Jung, K.T. Park, M.N. Gueye, S.H. So, C.R. Park, Bio-inspired graphene foam decorated with Pt nanoparticles for hydrogen storage at room temperature, Int. J. Hydrogen Energ., 41 (2016) 5019-5027.
[41] Y. Wang, L. Li, X. Huang, Q. Li, G. Li, New insights into fluorinated TiO2 (brookite, anatase and rutile) nanoparticles as efficient photocatalytic redox catalysts, RSC Advances, 5 (2015) 34302-34313.
[42] W.-S. Wang, D.-H. Wang, W.-G. Qu, L.-Q. Lu, A.-W. Xu, Large Ultrathin Anatase TiO2 Nanosheets with Exposed {001} Facets on Graphene for Enhanced Visible Light Photocatalytic Activity, The Journal of Physical Chemistry C, 116 (2012) 19893-19901.
[43] J. Yu, Q. Xiang, J. Ran, S. Mann, One-step hydrothermal fabrication and photocatalytic activity of surface-fluorinated TiO2 hollow microspheres and tabular anatase single micro-crystals with high-energy facets, Cryst. Eng. Comm., 12 (2010) 872-879.
[44] L. Gu, J. Wang, H. Cheng, Y. Du, X. Han, Synthesis of nano-sized anatase TiO2 with reactive {001} facets using lamellar protonated titanate as precursor, Chem. Commun., 48 (2012) 6978-6980.
[45] J. Ding, Z. Huang, J. Zhu, S. Kou, X. Zhang, H. Yang, Low-temperature synthesis of high-ordered anatase TiO2 nanotube array films coated with exposed {001} nanofacets, Sci. Rep., 5 (2015) 17773.
[46] M. Sankaran, B. Viswanathan, The role of heteroatoms in carbon nanotubes for hydrogen storage, Carbon, 44 (2006) 2816-2821.
[47] Z.G. Bajestani, A. Yurum, Y. Yurum, Significant improvement in the hydrogen storage capacity of a reduced graphene oxide/TiO2 nanocomposite by chemical bonding of Ti-O-C, RSC Advances, 6 (2016) 32831-32838.

[48] M. Choucair, P. Mauron, Versatile preparation of graphene-based nanocomposites and their hydrogen adsorption, Int. J. Hydrogen Energy, 40 (2015) 6158-6164.
[49] P. Kula, W. Szymanski, L. Kolodziejczyk, R. Atraszkiewicz, J. Grabarczyk, M. Clapa, L. Kaczmarek, A. Jedrzejczak, P. Niedzielski, High strength metallurgical graphene for hydrogen storage nanocomposites, Vacuum, 129 (2016) 79-85.
[50] G.M. Psofogiannakis, T.A. Steriotis, A.B. Bourlinos, E.P. Kouvelos, G.C. Charalambopoulou, A.K. Stubos, G.E. Froudakis, Enhanced hydrogen storage by spillover on metal-doped carbon foam: an experimental and computational study, Nanoscale, 3 (2011) 933-936.
[51] L. Wang, N.R. Stuckert, H. Chen, R.T. Yang, Effects of Pt Particle Size on Hydrogen Storage on Pt-Doped Metal−Organic Framework IRMOF-8, J. Phys. Chem. C, 115 (2011) 4793-4799.

Chapter 6 : Decoration of graphene sheets with Pd/Al_2O_3 hybrid particles for hydrogen storage applications

In this chapter we report the preparation and utilization of Pd/Al_2O_3 hybrid particles as a heterogeneous catalyst for enhancement of hydrogen storage capacity of reduced graphene oxide [1]. This study, to the best of our knowledge, is the first of its kind to utilize a hybrid particle with low Pd loading for hydrogen storage applications. All measurements were made at room temperature and pressures relevant for practical on-board storage systems.

6.1 Introduction

Weak binding energy between graphene sheets and H_2 at ambient conditions is the key factor that leads to low H_2 adsorption capacity of pristine graphene. To achieve higher H_2 uptake, chemical and structural modifications have been performed to exploit all the potentials of graphene [2]. One of the promising methods is decoration of graphene sheets with transition metals such as Pd [3], Pt [4], V [5] and Ti [6]. Given the high catalytic activity of Pd, it is the material of choice for decoration of graphene to improve the hydrogen uptake at ambient temperatures [3, 7]. Although Pd has strong potential to serve as a catalyst for hydrogen conversion, control of particle size, excessive hydrogen adsorption strength, scarcity and expensiveness restrict the utilization of Pd as a homogenous catalyst in hydrogen storage applications [8, 9]. In addition, high amount of catalyst that is needed to increase the hydrogen storage capacity is another confining parameter for usage of Pd. Huang et al [4], Chen et al [10] and Vinayan et al [5] reported that more than 50% increase in hydrogen uptake of different carbonaceous materials can be achievable when 2.2 wt. %, 7.78 wt. % and 30 wt. % Pd is added to the support, respectively. Different methods have been suggested to overcome these restrictions such as synthesizing Pd-based nanoalloys and using supporting materials. In the latter, the supporting material functions as nucleation seeds and enables growth and size control of noble metals. Additionally, this gives rise to enhanced activity and stability of the hybrid system [11-14].

Alumina (Al_2O_3), due to showing a wide range of catalytic reactions, is one of the most commonly used support materials for metal and metal oxide catalysts [15]. As a metallic catalyst support, various active sites such as surface defects and A1–OH groups provide high metal dispersion compared to most other metal oxide support materials [16]. Besides, formation of different coordination of Al^{3+} and migration of protons or OH groups upon dehydroxylation (450-700 °C) provide opportunity for different Lewis acid sites and OH groups to interact with adsorbed species [15].

Here, we report the preparation and utilization of Pd/Al_2O_3 hybrid particles as a heterogeneous catalyst for enhancement of hydrogen storage capacity of RGO. All hydrogen storage measurements were made at room temperature and pressures relevant for practical on-board storage systems.

6.2 Results and discussion

6.2.1 Characterization of nanocomposites

Characteristic properties of samples were summarized in Table 6.1.

Table 6.1 lists the primary particle size and molar ratio of Pd/Al_2O_3 for different RGO nanocomposites.

Name	Primary particle size of Al_2O_3 (nm)	Al_2O_3/Pd (mol/mol)	Al_2O_3/GO (wt/wt)
Al-220-10	220	10	1/300
Al-13-10	13	10	1/300
Al-13-3	13	3	1/300

X-ray diffraction (XRD) was first performed to determine the crystallographic structure of graphite oxide (GO), RGO and RGO nanocomposites. As shown in Figure 6.1, natural graphite flakes showed a sharp peak at $2\theta = 26°$ that corresponds to (002) plane and an interlayer spacing (d-spacing) of 3.3 Å. Upon oxidation, the (002) peak disappeared and a low intensity peak, indexed as (001), emerged at $2\theta = 10.5°$ with d-spacing of 8.37 Å. This increase of the d-spacing after oxidation has been correlated with intercalation of

oxygen-containing groups between graphene layers which leads to a change of the crystallographic structure of graphite. Upon thermal reduction, a broad and low-intensity (002) peak was observed with no sign of (001) peak showing that GO sheets are completely reduced and free graphene-like sheets with poorly ordered structure are formed. The XRD patterns of RGO nanocomposites showed no characteristic peaks for Pd and Al_2O_3 (data not shown) which can be attributed to the low material content and/or small size of hybrid particles [17]. The XRD pattern of Al-13-3 was shown in Figure 6.1 as a representative XRD graph of RGO nanocomposites.

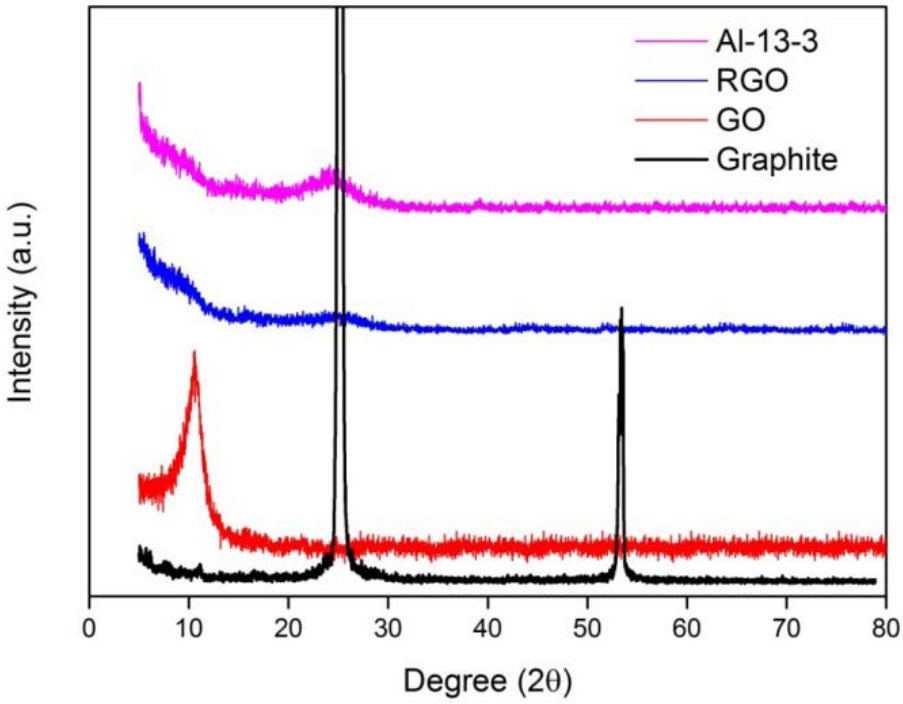

Figure 6.1 XRD pattern of graphite, GO, RGO and Al-13-3

Next, we tracked the distribution and size of the particles by using scanning electron microscopy (SEM) and energy dispersive spectroscopy (EDS). Figure 6.2a and b exhibit distributed nanoparticles with a size of 20 ± 15 nm and well-defined peaks of Al and Pd in EDS spectrum of RGO nanocomposite, respectively. The elemental mapping of this sample was provided by Figure 6.2c–f. Detection of similar distribution patterns for Al and Pd in elemental mapping shows strong evidence of the presence of hybrid particles in RGO nanocomposite. Although the exact form of hybrid particles cannot be determined in these

figures, it is more likely that very fine Pd/Al_2O_3 nanoparticles have been impregnated into graphene sheets [18].

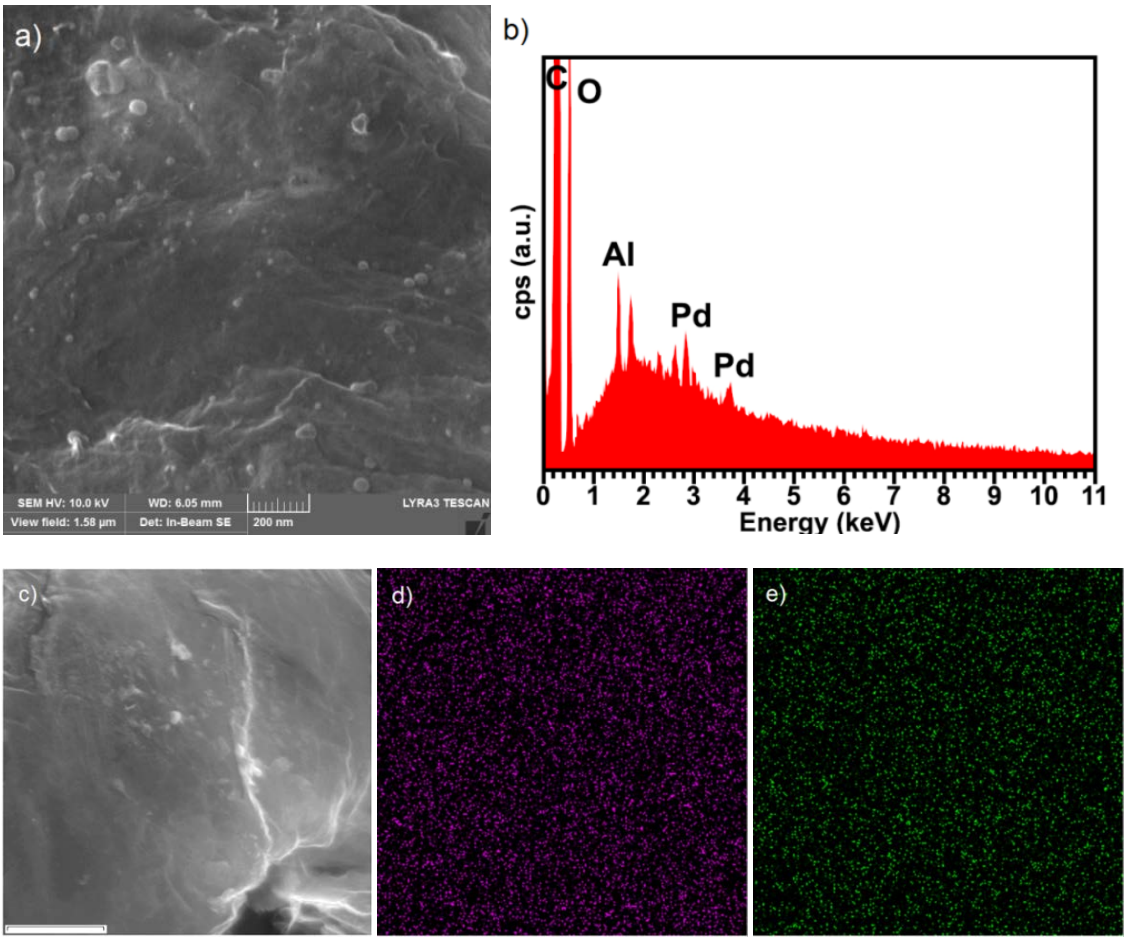

Figure 6.2 a) SEM image in high magnification and b) EDS spectrum of Al-13-3, c) SEM image in low magnification (scale bar shows 2.5 µm), d) Al elemental mapping and e) Pd elemental mapping of area shown in Figure 5.2c

In order to analyze the morphology of hybrid particles, a representative transmission electron microcopy (TEM) micrograph was shown in Figure 6.3. Homogeneous dispersion of hybrid particles was found on the transparent few layer graphene sheets. Closer observation, presented in the inset of Figure 6.3, shows two partially overlapped nanoparticles in which Pd (bright cluster) is deposited on the surface of Al_2O_3 nanoparticle (dark region). Cabria et al. [19] demonstrated that transition metals such as Ti, Pd, and Pt doped on carbonaceous materials suffer from agglomeration and particle growth. Since H_2 molecule dissociates easily on the surface of catalyst, agglomeration reduces the number of

active sites for the hydrogen adsorption [20]. According to Wang et al. [21], size and anchoring of nanocrystals to graphene substrate are dependent on the degree of oxidation of underlying sheets. Highly oxidized GO interacts strongly with particles and gives rise to strong pinning force which hinders the diffusion and growth of formed particles [22, 23]. Thus, incorporation of fine and distributed nanoparticles is highly preferred in order to obtain higher H_2 uptake of RGO nanocomposite.

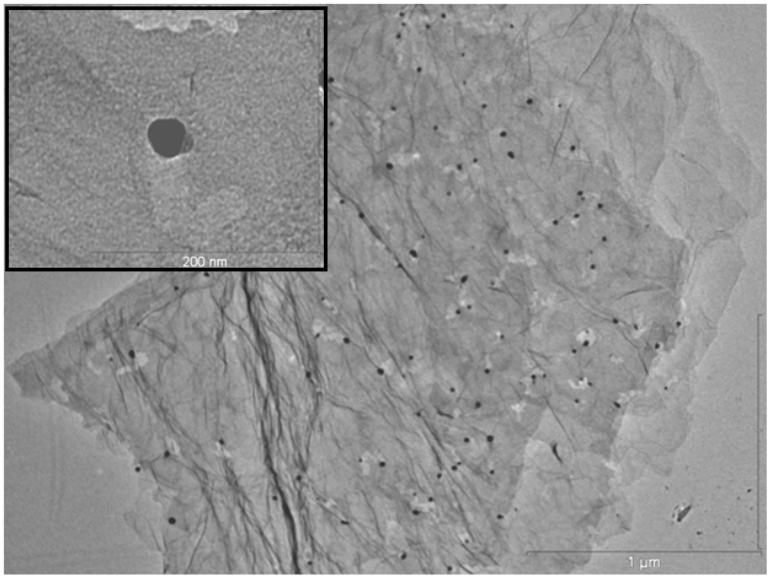

Figure 6.3 TEM micrograph of RGO nanocomposite, inset shows deposition of Pd (bright particle) on Al_2O_3 nanoparticle (darker particle)

X-ray photoelectron spectroscopy (XPS) was carried out to elucidate the chemical state of RGO nanocomposites. A wide energy scan was carried out on Al-13-3 that gives an XPS survey spectrum with Al (2p), Pd (3d), O 1s and C 1s with no trace of contaminations (data not shown). The spectrum was dominated by the O 1s and C 1s signals which are typical for this kind of graphene nanocomposites. Figure 6.4a depicts C 1s XPS spectrum of GO with four peaks centered at 284.56, 285.02, 286.8 and 288.8 eV. These peaks were assigned respectively to the C–C (aromatic), C–OH, C (epoxy/ alkoxy)/C=O and O=C–O (carboxylic) [24-27] groups that imply the highly oxidized state of GO sheets. After thermal reduction, the intensity of components associated with oxygenated functional groups decreased, (Figure 6.4b) demonstrating that most of the oxygen-containing functional groups were removed and GO mostly was transformed to graphene [24]. In order

to determine the oxidation state of Pd and Al species, Pd (3d) and Al (2p) spectra were analyzed and shown in Figure 6.4c and 6.4d, respectively.

Two spin–orbit split peaks of Pd(3d) spectrum were resolved in RGO nanocomposite, where Pd($3d_5$) is clear at the binding energy of 337.08 eV. Previous studies showed that oxidized Pd (PdO_x) presents binding energies of 336.4 eV (PdO) and 337.6 eV (PdO_2) [28, 29]. Therefore, it can be concluded that PdO_x species with x>1 are formed on the surface of the hybrid particles. In case of Al, the Al ($2p_3$) peak located at 74.3 eV was assigned to Al–O in Al_2O_3 compound. This value was shifted to lower binding energies compared to the data reported in the literature [30, 31] that suggests the electron transfer to Al^{3+} species. Figure 6.4e depicts the O 1s spectrum of GO with the peak centered at 532.3 eV. After addition of catalyst, this peak was shifted to the high binding energy side of the spectrum (532.9 eV) indicating formation of electron-deficient species on graphene sheets. Subsequently, simultaneous presence of Pd^{x+} x>2, lower bonding energy of Al^{3+} and higher bonding energy of oxygen in RGO nanocomposite illustrate that electrons could be donated from GO and Pd to Al_2O_3 component [28]. Indeed, development of these interactions in RGO nanocomposite is desired as forming pinning force between PdO_x/Al_2O_3 and graphene sheets [32].

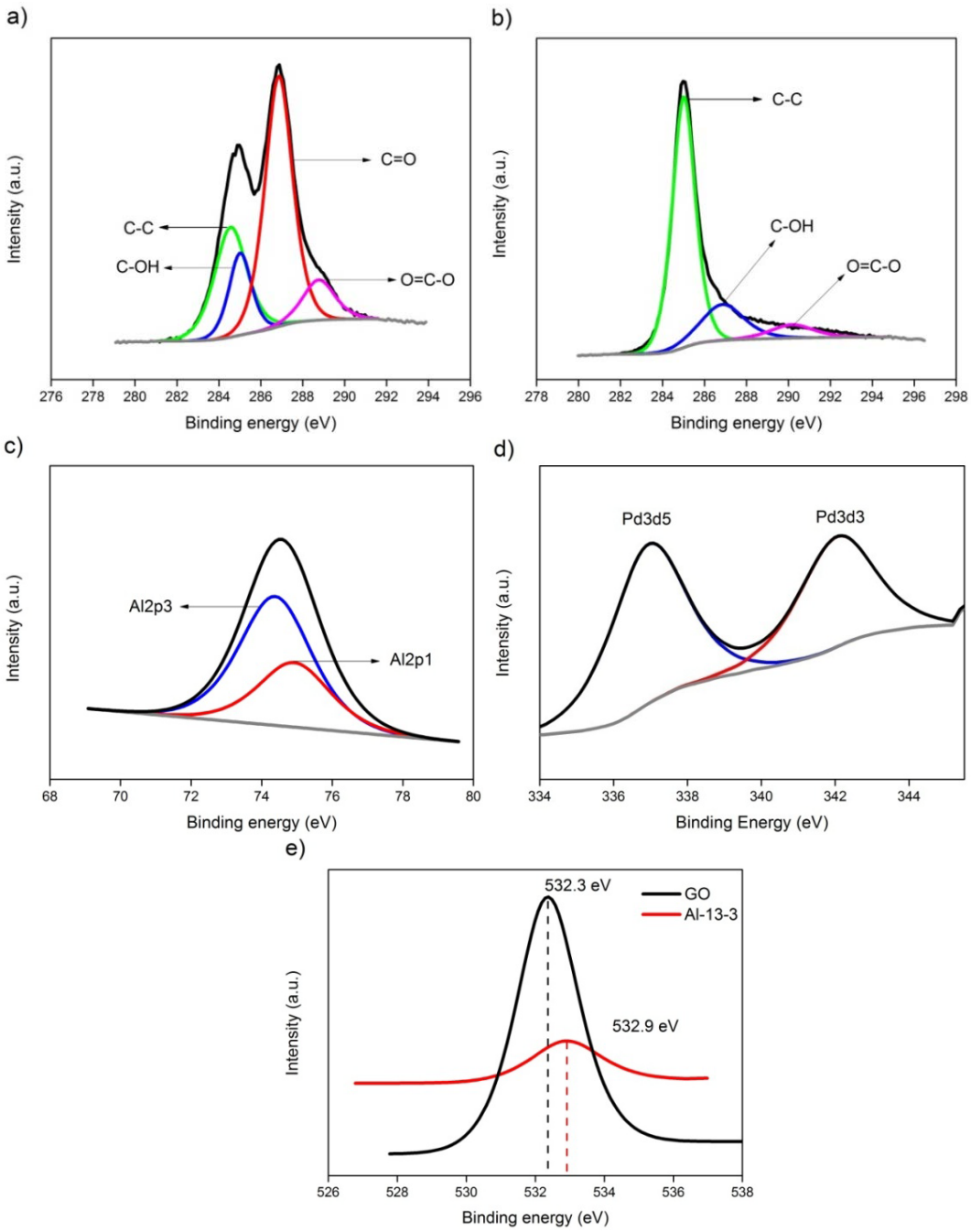

Figure 6.4 a) C1s scan of GO, b) C1s scan of RGO, c) Al2p scan of Al-13-3, d) Pd3d scan of Al-13-3, and e) O1s scan of GO and Al-13-3

To further support the interaction between catalyst and graphene sheets, Raman spectroscopy was performed on RGO and RGO nanocomposite. As shown in Figure 6.5, two characteristic bands were observed at ~1600 cm^{-1} (known as G band) and ~1350 cm^{-1} (known as D band). The D band is attributed to disorder in the symmetrical hexagonal

graphitic lattice, while the G band originates from the in-plane stretching motion of symmetric sp^2 C−C bonds [33-35]. Compared to Raman spectrum of RGO, the G band of RGO nanocomposite was shifted to lower wave number by ~3 cm^{-1}. In addition, the intensity ratio of the D and G (I_D/I_G) of RGO nanocomposite became lower than that of RGO that can be ascribed by the interactions between the hybrid particles and graphene sheets [36].

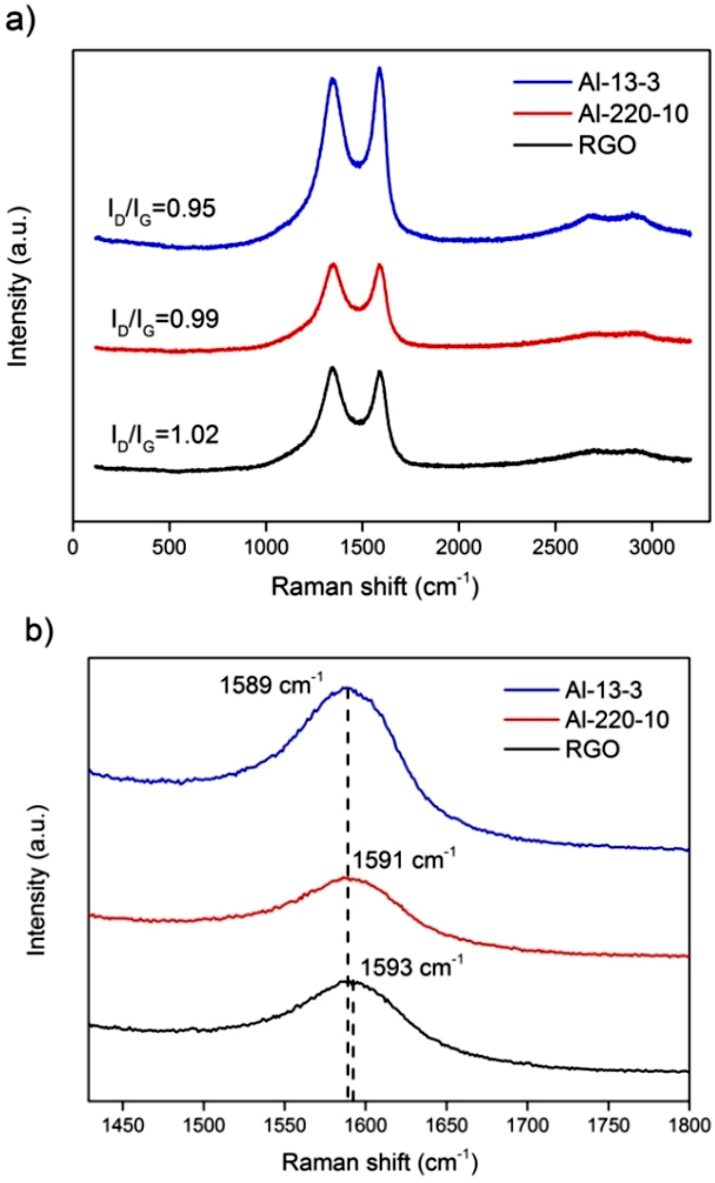

Figure 6.5 Raman spectra of RGO and RGO nanocomposites a) entire spectrum and b) between1400–1800 cm^{-1} (G band)

6.2.2 Gas adsorption behavior of nanocomposites

To characterize the specific surface area and pore structure of samples, N_2 adsorption−desorption isotherm was measured (Figure 6.6a). According to the IUPAC classification, specimens showed a nature of type IV curve, that is, a low N_2 adsorption capacity at low relative pressure (P/P_0) followed by a hysteresis loop at high P/P_0. The former indicates the presence of small number of micropores while the latter reflects formation of mesoporous structures in the system [37-39]. Lower nitrogen adsorption of RGO nanocomposites than that of RGO illustrated the lower adsorption capability of the nanocomposite when physical adsorption is the dominated process [40]. Moreover, Barret-Joyner-Halenda (BJH) method was applied to determine the pore structure of samples. The pore-size distribution isotherm of RGO (Figure 6.6b) displayed a sharp peak concentrated at ~2.5 nm followed by a shoulder at ~3.7 nm. After incorporation of hybrid particles, the main peak was depressed significantly and another shoulder emerged at higher radius (~ 50 nm). The BET surface area and total pore volume of samples were listed in Table 5.2. These indicate the decrease of BET surface area and total pore volume after addition of the catalysts. In the view of aforementioned results, the loss of the BET surface area and total pore volume of RGO nanocomposites are connected with changes in the pore structure and occupation of the most of the free spaces between graphene sheets by hybrid particles [18, 41].

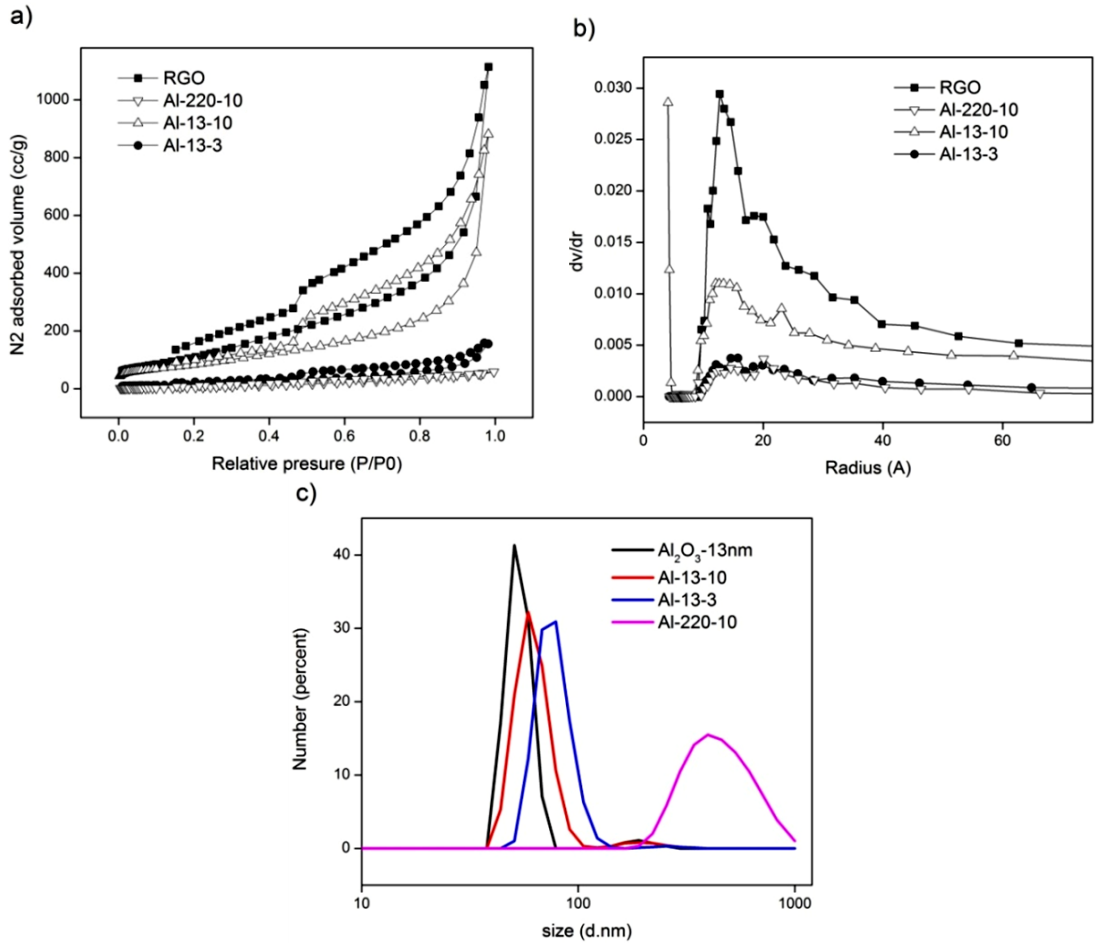

Figure 6.6 nitrogen adsorption-desorption isotherms, b) pore size distribution of RGO and RGO nanocomposites, and c) particle size distribution of hybrid particles

In addition, changes in the BET surface area of RGO nanocomposites were found to be inversely proportional to the size of hybrid particles during mixing process. Figure 6.6c depicts the particle size distribution of particles before adding to GO mixture. As a reference, particle size distribution of Al_2O_3 nanoparticles (with primary particle size of 13 nm) after sonication was shown in Figure 5.6c and referred to as Al_2O_3-13nm. Increase of r_h and width of size distribution curves can be correlated with the size of Al_2O_3 nanoparticles as well as surface coverage of Pd components. As a result, decreasing BET surface area with increment of r_h of hybrid particles can be related to increasing blockage of micropores [18, 41].

Table 6.2 BET surface area, total pore volumes and hydrogen uptakes at 298 K of RGO and RGO nanocomposites

Sample	S_{BET} (m^2/g)	V_{total} (cm^3/g)	H_2 uptake (wt. %)
RGO	461.8	1.72	0.17
Al-220-10	47.2	0.09	0.18
Al-13-10	319	1.363	0.24
Al-13-3	62.8	0.24	0.31

Hydrogen adsorption isotherms of RGO and RGO nanocomposites at 298 K were shown in Figure 6.7. RGO presents a H_2 uptake of 0.17 wt. % at 10 bar, slightly higher than reported values under the similar conditions [42]. Addition of hybrid particles with larger Al_2O_3 particle size introduced negligible effect on the enhancement and behavior of hydrogen uptake. On the other hand, Al-13-3 exhibited a significantly higher hydrogen storage capacity of 0.31 wt. % and increasing the slope of the isotherm in the intermediate and high pressure regimes.

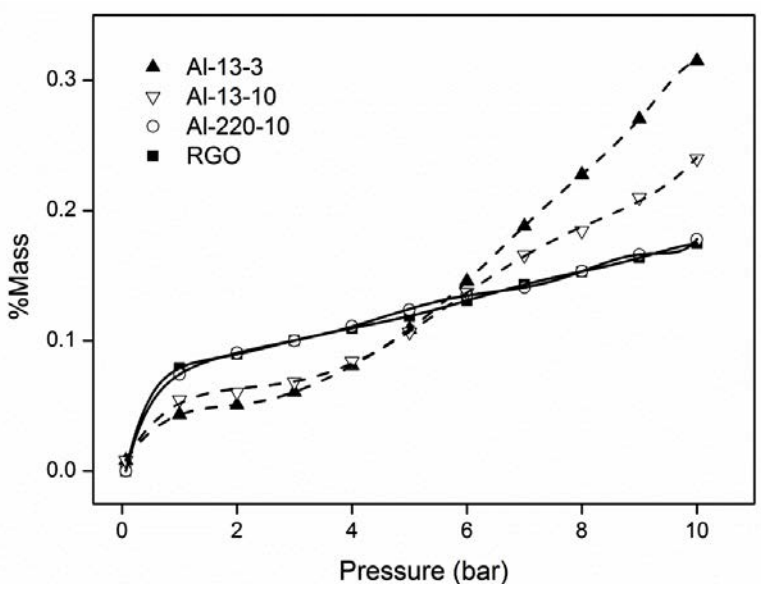

Figure 6.7 Hydrogen adsorption isotherms RGO and RGO nanocomposites

Four different mechanisms have been proposed to explain the hydrogen uptake of Pd-doped carbonaceous materials: i) physisorption on carbon support, ii) hydride formation in

large Pd particles, iii) H spillover to carbon substrate, and iv) Kubas-type bonding to isolated Pd atoms [43]. Higher hydrogen capacity of the RGO nanocomposite cannot be attributed to the differences in the surface area and pore volume since both of them were lower in RGO nanocomposites compared to that of RGO (Table 6.2). Furthermore, since Pd content of samples is < 0.3 wt. % formation of Pd hydrides has negligible contribution to enhancement of hydrogen uptake. Given the assumption that the entire Pd atoms were converted to β-$PdH_{0.67}$, which saturates quickly at room temperature and low H_2 pressures, hydrogen uptake of samples via formation of metal hydrides cannot exceed 0.005 wt. %. Kubas-type bonding necessitates the presence of single atom metal centers and clustering changes the mechanism to chemisorption on larger crystals (Figure 6.3) [43]. Therefore, the improving hydrogen storage capacity of RGO nanocomposites by decrease of particle size of Al_2O_3 nanoparticles and increase of Pd content can be attributed to the activation of other processes, usually grouped as spillover. In addition, increasing slope of the isotherms may be an evidence of activation of spillover process. According to Li and Yang [44], observation of non-linear shape of isotherms can be explained by pressure dependent diffusivity of spillover hydrogen. Khoobiar [45] demonstrated the dissociation of hydrogen molecules on Pt at room temperature followed by migration of active H atoms from parent $Pt/A1_2O_3$ particles to substrate indicator particles.

Li et al [46] demonstrated that hydrogen atoms from the dissociation of H_2 at noble metal donate electrons to Lewis acid sites of the supporting material. Since surface diffusion of hydrogen atoms is the rate-determining step in hydrogen spillover [47], strong interaction between H atom and Lewis acid sites reduce the diffusion of hydrogen atom on the surface of supporting material. Therefore, presence of weak Lewis acid sites, like five-coordinate Al^{3+} in γ-Al_2O_3, facilitates diffusion of hydrogen atoms on the surface of the supporting materials [46]. As a result, we can conclude that higher hydrogen uptake of RGO nanocomposites can be a result of concomitant activity of physical absorption and chemical adsorption of dissociated H_2 on the graphene sheets [48]. The low loadings of Pd (< 0.3 wt%) in RGO nanocomposites compared to that of reported in literature for Pd-RGO [4, 5, 49] suggests a strong potential for these hybrid particles to be used in hydrogen storage application.

6.3 Conclusions

The Pd/Al_2O_3-reduced graphene oxide nanocomposite (Pd<0.3 wt. %) was successfully prepared by incorporation of Pd/Al_2O_3 hybrid particles with graphite oxide followed by thermal reduction in controlled atmosphere. The results from this work demonstrated that size of the support material in heterogeneous catalyst plays an important role to enhance the hydrogen storage capacity of RGO. The hydrogen uptake of 0.31 wt. % at room temperature and pressure of 10 bar was obtained for the sample containing Al_2O_3 primary particle size of 13 nm and Pd/Al_2O_3 of 1/3 wt/wt (Al-13-3 nanocomposite). The significant improvement of hydrogen storage capacity of RGO after addition of 1 wt. % Pd/Al_2O_3 hybrid particles (Pd<0.3 wt. %) was connected with activation of processes usually grouped as spillover. The present findings may give rise to a pathway for development of new type of catalysts with low loadings of noble metals for preparation of high-performance hybrid particles–RGO nanocomposites.

6.4 References

[1] Z. Gohari Bajestani, A. Yürüm, Y. Yürüm, Decoration of graphene sheets with Pd/Al2O3 hybrid particles for hydrogen storage applications, International Journal of Hydrogen Energy, 41 (2016) 9810-9818.
[2] D.J. Durbin, C. Malardier-Jugroot, Review of hydrogen storage techniques for on board vehicle applications, International Journal of Hydrogen Energy, 38 (2013) 14595-14617.
[3] J. Fang, I. Levchenko, X. Lu, D. Mariotti, K. Ostrikov, Hierarchical bi-dimensional alumina/palladium nanowire nano-architectures for hydrogen detection, storage and controlled release, International Journal of Hydrogen Energy, 40 (2015) 6165-6172.
[4] C.-C. Huang, N.-W. Pu, C.-A. Wang, J.-C. Huang, Y. Sung, M.-D. Ger, Hydrogen storage in graphene decorated with Pd and Pt nano-particles using an electroless deposition technique, Separation and Purification Technology, 82 (2011) 210-215.
[5] B.P. Vinayan, K. Sethupathi, S. Ramaprabhu, Facile synthesis of triangular shaped palladium nanoparticles decorated nitrogen doped graphene and their catalytic study for renewable energy applications, International Journal of Hydrogen Energy, 38 (2013) 2240-2250.
[6] T. Mashoff, M. Takamura, S. Tanabe, H. Hibino, F. Beltram, S. Heun, Hydrogen storage with titanium-functionalized graphene, Applied Physics Letters, 103 (2013) 013903.
[7] S. Dutta, A review on production, storage of hydrogen and its utilization as an energy resource, Journal of Industrial and Engineering Chemistry, 20 (2014) 1148-1156.
[8] L. Ma, J.-M. Zhang, K.-W. Xu, Hydrogen storage on nitrogen induced defects in palladium-decorated graphene: A first-principles study, Applied Surface Science, 292 (2014) 921-927.

[9] B. Sakintuna, F. Lamari-Darkrim, M. Hirscher, Metal hydride materials for solid hydrogen storage: A review, International Journal of Hydrogen Energy, 32 (2007) 1121-1140.
[10] C.-H. Chen, T.-Y. Chung, C.-C. Shen, M.-S. Yu, C.-S. Tsao, G.-N. Shi, C.-C. Huang, M.-D. Ger, W.-L. Lee, Hydrogen storage performance in palladium-doped graphene/carbon composites, International Journal of Hydrogen Energy, 38 (2013) 3681-3688.
[11] A. Mezni, I. Balti, A. Mlayah, N. Jouini, L.S. Smiri, Hybrid Au–Fe_3O_4 nanoparticles: Plasmonic, surface snhanced Raman scattering, and phase transition properties, The Journal of Physical Chemistry C, 117 (2013) 16166-16174.
[12] N. Hussain, A. Borah, G. Darabdhara, P. Gogoi, V.K. Azhagan, M.V. Shelke, M.R. Das, A green approach for the decoration of Pd nanoparticles on graphene nanosheets: An in situ process for the reduction of C-C double bonds and a reusable catalyst for the Suzuki cross-coupling reaction, New Journal of Chemistry, 39 (2015) 6631-6641.
[13] S. Gil, J. Garcia-Vargas, L. Liotta, G. Pantaleo, M. Ousmane, L. Retailleau, A. Giroir-Fendler, Catalytic oxidation of propene over Pd catalysts supported on CeO_2, TiO_2, Al_2O_3 and M/Al_2O_3 oxides (M = Ce, Ti, Fe, Mn), Catalysts, 5 (2015) 671.
[14] J. Im, H. Shin, H. Jang, H. Kim, M. Choi, Maximizing the catalytic function of hydrogen spillover in platinum-encapsulated aluminosilicates with controlled nanostructures, Nat Commun, 5 (2014).
[15] X. Liu, R.E. Truitt, DRFT-IR studies of the surface of γ-alumina, Journal of the American Chemical Society, 119 (1997) 9856-9860.
[16] T.H. Ballinger, J.T. Yates, IR spectroscopic detection of Lewis acid sites on alumina using adsorbed carbon monoxide. Correlation with aluminum-hydroxyl group removal, Langmuir, 7 (1991) 3041-3045.
[17] H. Zhou, J. Zhang, J. Zhang, X. Yan, X. Shen, A. Yuan, High-capacity room-temperature hydrogen storage of zeolitic imidazolate framework/graphene oxide promoted by platinum metal catalyst, International Journal of Hydrogen Energy, 40 (2015) 12275-12285.
[18] M.-S. Park, J.-S. Yu, K.J. Kim, G. Jeong, J.-H. Kim, Y.-N. Jo, U. Hwang, S. Kang, T. Woo, Y.-J. Kim, One-step synthesis of a sulfur-impregnated graphene cathode for lithium-sulfur batteries, Physical Chemistry Chemical Physics, 14 (2012) 6796-6804.
[19] I. Cabria, M.J. López, S. Fraile, J.A. Alonso, Adsorption and dissociation of molecular hydrogen on palladium clusters supported on graphene, The Journal of Physical Chemistry C, 116 (2012) 21179-21189.
[20] M. Lischka, A. Groß, Hydrogen adsorption on an open metal surface: H_2/Pd(210), Physical Review B, 65 (2002) 075420.
[21] H. Wang, J.T. Robinson, G. Diankov, H. Dai, Nanocrystal Growth on Graphene with Various Degrees of Oxidation, Journal of the American Chemical Society, 132 (2010) 3270-3271.
[22] C.-S. Tsao, Y.-R. Tzeng, M.-S. Yu, C.-Y. Wang, H.-H. Tseng, T.-Y. Chung, H.-C. Wu, T. Yamamoto, K. Kaneko, S.-H. Chen, Effect of Catalyst Size on Hydrogen Storage Capacity of Pt-Impregnated Active Carbon via Spillover, The Journal of Physical Chemistry Letters, 1 (2010) 1060-1063.
[23] C. Zlotea, F. Cuevas, V. Paul-Boncour, E. Leroy, P. Dibandjo, R. Gadiou, C. Vix-Guterl, M. Latroche, Size-dependent hydrogen sorption in ultrasmall Pd clusters embedded in a mesoporous carbon template, Journal of the American Chemical Society, 132 (2010) 7720-7729.

[24] L. Yue-Wen, G. Meng-Xue, F. Lan, D. Shun-Liu, B. Jian-Feng, X. Su-Yuan, C. Zhong, H. Rong-Bin, Z. Lan-Sun, Facile and straightforward synthesis of superparamagnetic reduced graphene oxide–Fe_3O_4 hybrid composite by a solvothermal reaction, Nanotechnology, 24 (2013) 025604.
[25] G. Compagnini, P. Russo, F. Tomarchio, O. Puglisi, L. D'Urso, S. Scalese, Laser assisted green synthesis of free standing reduced graphene oxides at the water–air interface, Nanotechnology, 23 (2012) 505601.
[26] P. Wang, Y. Zhai, D. Wang, S. Dong, Synthesis of reduced graphene oxide-anatase TiO_2 nanocomposite and its improved photo-induced charge transfer properties, Nanoscale, 3 (2011) 1640-1645.
[27] K. Li, T. Chen, L. Yan, Y. Dai, Z. Huang, J. Xiong, D. Song, Y. Lv, Z. Zeng, Design of graphene and silica co-doped titania composites with ordered mesostructure and their simulated sunlight photocatalytic performance towards atrazine degradation, Colloids and Surfaces A: Physicochemical and Engineering Aspects, 422 (2013) 90-99.
[28] J.C. Colmenares, A. Magdziarz, M.A. Aramendia, A. Marinas, J.M. Marinas, F.J. Urbano, J.A. Navio, Influence of the strong metal support interaction effect (SMSI) of Pt/TiO_2 and Pd/TiO_2 systems in the photocatalytic biohydrogen production from glucose solution, Catalysis Communications, 16 (2011) 1-6.
[29] J.J. Dodson, H.E. Hagelin-Weaver, Effect of titania structure on palladium oxide catalysts in the oxidative coupling of 4-methylpyridine, Journal of Molecular Catalysis A: Chemical, 410 (2015) 271-279.
[30] C. Xu, T. Sritharan, S.G. Mhaisalkar, M. Srinivasan, S. Zhang, An XPS study of Al_2Au and $AlAu_4$ intermetallic oxidation, Applied Surface Science, 253 (2007) 6217-6221.
[31] N.M. Figueiredo, N.J.M. Carvalho, A. Cavaleiro, An XPS study of Au alloyed Al–O sputtered coatings, Applied Surface Science, 257 (2011) 5793-5798.
[32] Z.-S. Wu, G. Zhou, L.-C. Yin, W. Ren, F. Li, H.-M. Cheng, Graphene/metal oxide composite electrode materials for energy storage, Nano Energy, 1 (2012) 107-131.
[33] M. Giovanni, H.L. Poh, A. Ambrosi, G. Zhao, Z. Sofer, F. Sanek, B. Khezri, R.D. Webster, M. Pumera, Noble metal (Pd, Ru, Rh, Pt, Au, Ag) doped graphene hybrids for electrocatalysis, Nanoscale, 4 (2012) 5002-5008.
[34] X. Wang, X. Zhang, Electrochemical co-reduction synthesis of graphene/nano-gold composites and its application to electrochemical glucose biosensor, Electrochimica Acta, 112 (2013) 774-782.
[35] A. Ambrosi, A. Bonanni, Z. Sofer, J.S. Cross, M. Pumera, Electrochemistry at Chemically Modified Graphenes, Chemistry – A European Journal, 17 (2011) 10763-10770.
[36] Y. Haldorai, W. Voit, J.-J. Shim, Nano ZnO@reduced graphene oxide composite for high performance supercapacitor: Green synthesis in supercritical fluid, Electrochimica Acta, 120 (2014) 65-72.
[37] S. Yang, Y. Sun, L. Chen, Y. Hernandez, X. Feng, K. Müllen, Porous Iron Oxide Ribbons Grown on Graphene for High-Performance Lithium Storage, Scientific Reports, 2 (2012) 427.
[38] Y. Linhui, R. Hong, Z. Yi, L. Danzhen, A facile solvothermal method to produce ZnS quantum dots-decorated graphene nanosheets with superior photoactivity, Nanotechnology, 24 (2013) 375601.
[39] W. Guanghui, L. Ruiyi, L. Zaijun, L. Junkang, G. Zhiguo, W. Guangli, N-doped graphene/graphite composite as a conductive agent-free anode material for lithium ion

batteries with greatly enhanced electrochemical performance, Electrochimica Acta, 171 (2015) 156-164.
[40] Y. Wang, J. Liu, K. Wang, T. Chen, X. Tan, C.M. Li, Hydrogen storage in Ni–B nanoalloy-doped 2D graphene, International Journal of Hydrogen Energy, 36 (2011) 12950-12954.
[41] L. Zu, X. Cui, Y. Jiang, Z. Hu, H. Lian, Y. Liu, Y. Jin, Y. Li, X. Wang, Preparation and electrochemical characterization of mesoporous polyaniline-silica nanocomposites as an electrode material for pseudocapacitors, Materials, 8 (2015) 1369.
[42] G. Srinivas, Y. Zhu, R. Piner, N. Skipper, M. Ellerby, R. Ruoff, Synthesis of graphene-like nanosheets and their hydrogen adsorption capacity, Carbon, 48 (2010) 630-635.
[43] C.I. Contescu, K. van Benthem, S. Li, C.S. Bonifacio, S.J. Pennycook, P. Jena, N.C. Gallego, Single Pd atoms in activated carbon fibers and their contribution to hydrogen storage, Carbon, 49 (2011) 4050-4058.
[44] Y. Li, R.T. Yang, Hydrogen storage on platinum nanoparticles doped on superactivated carbon, The Journal of Physical Chemistry C, 111 (2007) 11086-11094.
[45] S. Khoobiar, Particle to particle migration of hydrogen atoms on platinum—alumina catalysts from particle to neighboring particles, The Journal of Physical Chemistry, 68 (1964) 411-412.
[46] Y. Li, F.H. Yang, R.T. Yang, Kinetics and mechanistic model for hydrogen spillover on bridged metal−organic frameworks, The Journal of Physical Chemistry C, 111 (2007) 3405-3411.
[47] L. Wang, R.T. Yang, New sorbents for hydrogen storage by hydrogen spillover - a review, Energy & Environmental Science, 1 (2008) 268-279.
[48] A. Sigal, M.I. Rojas, E.P.M. Leiva, Is hydrogen storage possible in metal-doped graphite 2D systems in conditions found on earth?, Physical Review Letters, 107 (2011) 158701.
[49] N. Ismail, M. Madian, M.S. El-Shall, Reduced graphene oxide doped with Ni/Pd nanoparticles for hydrogen storage application, Journal of Industrial and Engineering Chemistry, 30 (2015) 328-335.

Chapter 7: General Conclusions

This thesis examined the feasibility of using reduced graphene oxide based nanocomposite as hydrogen storage media in ambient conditions.

In chapter 3, graphene sheets were decorated by transition metal oxide (TiO_2, NiO, Fe_3O_4, CuO) by a chemical method for hydrogen storage capacity. All hydrogen isotherms were measured at ambient pressures and temperatures of 25 and 55 °C. As expected, hydrogen uptake increased by pressure and decreased by temperature in all composites. Moreover, hydrogen capacity improved after addition of metal oxide nanoparticles in the case of nanocomposite compare to RGO. The highest storage capacity of 0.4 wt. % was obtained by RGO-Fe nanocomposites while RGO-Ti demonstrated the highest improvement in the isosteric heat of adsorption when normalized by maximum uptake at 298k.

As reported in chapter 4, a series of graphene-based nanocomposites with different TiO_2 contents have been prepared via a facile chemical method. All nanocomposites were employed as hydrogen gas adsorption materials at room temperature and pressure up to 10 bar. The effect of dispersion state and size of the particles on the hydrogen storage capacity of nanocomposites was studied. The highest hydrogen uptake of 0.39 wt% was obtained among prepared nanocomposites and it is 125% higher than the hydrogen adsorption of the parent graphene material. This improvement can account for the presence of a high number of active sites needed for hydrogen molecules and the strong interaction between nanoparticles and graphene sheets.

In chapter 5 of the thesis, homogeneously distributed TiO_2 nanoparticles with (001) reactive facets were grown over nitrogen-doped reduced graphene oxide sheets (N-RGO) under solvothermal conditions. Hydrogen storage capacity of the system was significantly improved to 0.91 wt% at room temperature and pressure of 0.8 MPa that is the highest hydrogen storage ever reported for graphene-based nanocomposites at room temperature and low pressures. Importantly, this nanocomposite exhibits ~91% capacity retention through 5 cycles with more than 88% release of the stored hydrogen at ambient conditions. Enhanced hydrogen uptake and capacity retention were attributed to the synergistic effect of i) reactive facets of TiO2, ii) high dispersion of nanoparticles with the average size of 6 nm, and iii) strong interaction between the substrate and TiO_2 nanoparticles through polarized C–N bonding of N-rGO sheets.

In chapter 6, we reported the development of a heterogeneous catalyst consisting of Al_2O_3 nanoparticle and low amounts of Pd that markedly enhances the hydrogen uptake of RGO. The Pd/Al2O3 hybrid particles were prepared by ultrasound-assisted impregnation of $PdCl_2$ in an aqueous suspension of Al_2O_3 nanoparticles. Hybrid particles were immobilized onto the RGO support, giving Pd/Al_2O_3–RGO nanocomposites. It was shown that incorporation of 1 wt% heterogeneous catalyst (<0.3 wt% Pd) significantly increased the hydrogen storage capacity of RGO from 0.17 wt% to 0.31 wt%. This indicated a rise of hydrogen uptake by a factor of 1.8 in RGO nanocomposite. The improving hydrogen storage capacity of RGO nanocomposites by the change of Al_2O_3 particle size and Pd content was linked to activation of processes usually grouped as spillover.

Through this thesis, we have demonstrated that size of nanoparticles, dispersion state, and interaction between nanoparticles and substrate plays an important role to increase the hydrogen storage capacity of the nanocomposite. Additionally, we illustrated that particles with active facets can improve the activity of the composites toward adsorption of hydrogen gas molecules. We achieved hydrogen uptake of 0.91wt% which is the highest amount of hydrogen storage capacity reported for graphene based nanocomposites in the literature in moderate conditions.

Through these Chapters, reduced graphene oxide can be expected to function as a substrate for new composite material for energy storage applications. In this study, the effect of the substrate with different surface area and porosity on hydrogen storage behavior of composites was not examined. I believe the next step to further enhance the performance of graphene will be synthesizing the three-dimensional architecture of graphene materials. Graphene–single walled carbon nanotube (SWCNT) integrated 3D materials with a pillared structure can be produced by chemical and/or CVD method. These scaffolds provide high surface area, low density, and chemical–mechanical stability, as they have micro, meso, and macro porous structures. These 3D graphene architectures can serve as ideal scaffolds for depositing inorganic materials. 3D structural composites of transition metal oxide doped reduced graphene oxide/CNT would suggest an alternative and novel material for possible applications in energy storage devices. Together with an additional study regarding desorption properties of graphene based nanocomposites, such studies should allow the practical realization of graphene scaffold as eco-friendly energy storage systems.